Max-Planck-Institut
für Meteorologie

MAX-PLANCK-GESELLSCHAFT

International Max Planck Research School
on Earth System Modelling

Finite element methods, grid refinement, and boundary currents in geophysical modeling

Peter Dominik Düben

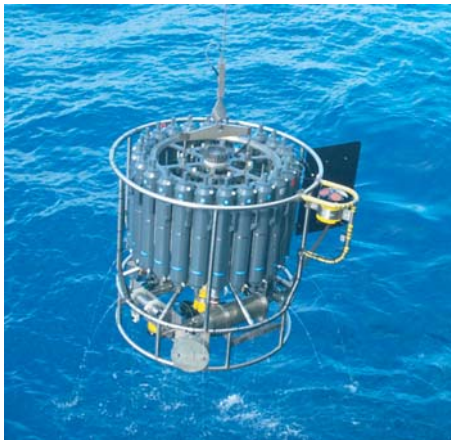

Berichte zur Erdsystemforschung 118/2012

Reports on Earth System Science

Hinweis

Die Berichte zur Erdsystemforschung werden vom Max-Planck-Institut für Meteorologie in Hamburg in unregelmäßiger Abfolge herausgegeben.

Sie enthalten wissenschaftliche und technische Beiträge, inklusive Dissertationen.

Die Beiträge geben nicht notwendigerweise die Auffassung des Instituts wieder.

Die "Berichte zur Erdsystemforschung" führen die vorherigen Reihen "Reports" und "Examensarbeiten" weiter.

Notice

The Reports on Earth System Science are published by the Max Planck Institute for Meteorology in Hamburg. They appear in irregular intervals.

They contain scientific and technical contributions, including Ph. D. theses.

The Reports do not necessarily reflect the opinion of the Institute.

The "Reports on Earth System Science" continue the former "Reports" and "Examensarbeiten" of the Max Planck Institute.

Anschrift / Address

Max-Planck-Institut für Meteorologie
Bundesstrasse 53
20146 Hamburg
Deutschland

Tel.: +49-(0)40-4 11 73-0
Fax: +49-(0)40-4 11 73-298
Web: www.mpimet.mpg.de

Layout:

Bettina Diallo, PR & Grafik

Titelfotos:
vorne:
Christian Klepp - Jochem Marotzke - Christian Klepp
hinten:
Clotilde Dubois - Christian Klepp - Katsumasa Tanaka

Berichte zur Erdsystemforschung 118/2012

Finite element methods, grid refinement, and boundary currents in geophysical modeling

Peter Dominik Düben

aus Bad Berleburg

Hamburg 2012

Reports on Earth System Science 118/2012

ISSN 1614-1199

Peter Dominik Düben
Max-Planck-Institut für Meteorologie
Bundesstrasse 53
20146 Hamburg

Als Dissertation angenommen
vom Department Geowissenschaften der Universität Hamburg

auf Grund der Gutachten von
Prof. Dr. Jochem Marotzke
und
Dr. Peter Korn

Hamburg, den 27. Juni 2012
Prof. Dr. Jürgen Oßenbrügge
Leiter des Departments für Geowissenschaften

ISSN 1614-1199

Finite element methods, grid refinement, and boundary currents in geophysical modeling

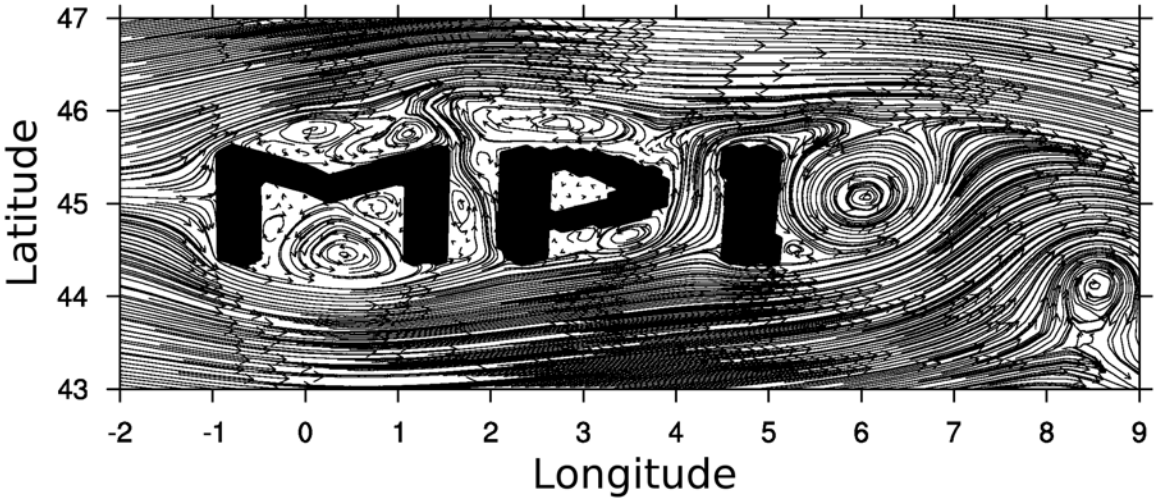

Peter Dominik Düben

Hamburg 2012

Abstract

Most of today's dynamical cores of weather and climate models are based on finite difference, hybrid finite volume/finite difference, or spectral discretization methods. In the first part of this thesis, we evaluate a new finite element approach for the discretization of the equations of motion in geophysical modeling. Finite element methods offer a local, higher order representation of the physical fields and allow the use of unstructured grids and grids with variable resolution. We use a new finite element that combines a continuous second order representation for the scalar field with a discontinuous first order representation for the velocity field, to develop a shallow-water model on a rotating sphere. This specific choice of a low-order element is attractive, since it has the remarkable property of being able to represent the geostrophic balance and fulfill the Ladyzhenskaya-Babuska-Brezzi-condition, which is a necessary condition for convergence in finite element modeling. In summary, we present a stable model setup and certify the new finite element approach to offer very promising properties for use in dynamical cores of global weather or climate models, in all tests performed. We propose the use of the stereographic projection to introduce spherical geometry to global finite element models.

In the second part of this thesis, we analyze the influence of grid refinement on fundamental features of geophysical modeling. Through the study of the transition of waves between coarse and fine parts of a grid, and the influence of grid refinement on the representation of geostrophic balance and turbulent cascades, we investigate possible sources of errors for applications of grid refinement in ocean and atmosphere modeling. Furthermore, we investigate improvements that are possible through grid refinement, by evaluating simulations of flow over topography, local wave patterns, and western boundary currents. We find that the improvements possible with local grid refinement justify the risk of a spurious reflection and scattering of waves, in the given geophysical setup.

In the final part of this thesis, we study boundary currents and boundary separation in finite element models. We evaluate the influence of local resolution, eddy viscosity, the grid structure, and the boundary conditions to the numerical representation of boundary currents, and try to identify proper criteria to detect boundary separation points in ocean modeling, for no-slip and free-slip boundary conditions, and steady and unsteady flows. To find these criteria, we study the physical fields along the coast line, and evaluate classical and recent theories for flow separation in Fluid Dynamics. Out of all of the evaluated criteria to detect separation points on no-slip boundaries, the two separation criteria by Prandtl work best. For free-slip boundaries, the two separation criteria by Lekien and Haller turned out to be the best choice.

Dies ist ein kleines Zahnrad in einem großen Getriebe.
Niemand weiß, ob eine Drehung eine kleine
oder eine große Wirkung entfalten wird.

Contents

1 Introduction **7**
- 1.1 Horizontal discretization in atmosphere and ocean models . . . 8
- 1.2 Grid refinement in atmosphere and ocean models . . . 11
- 1.3 Boundary currents and boundary separation in ocean models . . . 13
- 1.4 Thesis Outline . . . 14

2 A discontinuous/continuous low-order finite element shallow-water model on the sphere **17**
- 2.1 Introduction . . . 17
- 2.2 Model setup . . . 20
  - 2.2.1 The viscous shallow-water equations . . . 20
  - 2.2.2 The discontinuous/continuous finite element discretization . . . 20
  - 2.2.3 The spherical geometry . . . 24
- 2.3 Numerical results . . . 28
  - 2.3.1 Steady and unsteady solid body rotation . . . 30
  - 2.3.2 Rossby-Haurwitz wave . . . 34
  - 2.3.3 Zonal flow over an isolated mountain . . . 36
  - 2.3.4 Perturbed jet stream . . . 39
  - 2.3.5 Munk gyre test case . . . 42
- 2.4 Conclusions . . . 45

3 Variable resolution modeling in atmosphere and ocean is less painful than expected **47**
- 3.1 Introduction . . . 47
- 3.2 Model setup . . . 50
  - 3.2.1 The viscous shallow-water equations . . . 50
  - 3.2.2 Discretization . . . 50
  - 3.2.3 Grids and grid refinement . . . 51
- 3.3 Numerical results . . . 52
  - 3.3.1 Wave packets affected by grid refinement . . . 53
  - 3.3.2 Geostrophic balance affected by grid refinement . . . 60
  - 3.3.3 Turbulent decay of randomly initialized fields . . . 63
  - 3.3.4 Decay of a zonal flow over an isolated mountain . . . 66
  - 3.3.5 Perturbed jet stream . . . 67
  - 3.3.6 Ocean gyre test case . . . 70
- 3.4 Conclusion . . . 74
- 3.A Kinetic energy and enstrophy spectra on plane and sphere . . . 75
- 3.B Energy conservation . . . 76

4 A study of model parameters and discretized fields that influence boundary separation 77
4.1 Introduction . . . 77
4.2 Model setup . . . 80
4.2.1 The viscous shallow-water equations . . . 81
4.2.2 Discretization in space and time . . . 81
4.2.3 Grids and grid refinement . . . 82
4.2.4 Diagnostic tools for the identification of separation points . . . 82
4.2.5 Separation points and flow around a turn of the coast line . . . 83
4.3 Test cases . . . 83
4.3.1 The idealized coast line test . . . 83
4.3.2 The Atlantic test . . . 84
4.3.3 The island test . . . 86
4.4 Properties of boundary currents in a finite element shallow-water model . . . 89
4.4.1 The western boundary current in the idealized coast line test . . . 89
4.4.2 The western boundary current in the Atlantic test . . . 93
4.5 Criteria to detect boundary separation points . . . 93
4.5.1 The properties of an idealized separation point . . . 95
4.5.2 Approach $\mathbb{A}$: Evaluating the change of the tangential velocity in the normal direction following Prandtl (1904) and Haller (2004) . . . 97
4.5.3 Approach $\mathbb{B}$: Evaluating the vorticity following Ghil et al. (2004) . . . 104
4.5.4 Approach $\mathbb{C}$: Evaluating the change of the tangential velocity in the normal direction and the change of the normal velocity in the tangential direction following Lekien and Haller (2008) . . . 106
4.5.5 Approach $\mathbb{D}$: Evaluating the ratio between the tangential and normal velocity components . . . 112
4.5.6 Approach $\mathbb{E}$ . . . 115
4.6 Discussion of the results . . . 118
4.6.1 On western boundary currents in a finite element shallow-water model . . . 118
4.6.2 On criteria to detect boundary separation points . . . 119
4.7 Main conclusions . . . 120

5 Conclusions and Outlook 121
5.1 Scientific contribution . . . 121
5.2 Answers to the Research Questions . . . 122
5.3 Outlook . . . 124

Bibliography 125

Acknowledgements 131

Chapter 1

Introduction

In numerous scientific areas numerical modeling allows an improvement of understanding where experiments and analytical theory reach their limits. One of these scientific areas is the field of Fluid Dynamics. The equations of motion that describe fluids are well known. But – till today – many of these equations can not be solved analytically, due to nonlinearities. Experimental approaches are difficult and laborious for most of the scientific problems in Fluid Dynamics, as well. In Computational Fluid Dynamics (CFD) numerical methods are successfully used to simulate and understand the dynamics of fluid motion.

This thesis investigates scientific questions in the field of Geophysical Fluid Dynamics (GFD). GFD mainly focus on the dynamics of atmosphere and ocean. Since atmosphere and ocean are both chaotic systems of large magnitude, the applicability of experimental and analytical investigations is limited, while numerical models have proven to be useful tools to enhance our understanding of the dynamics of atmosphere and ocean, and to perform weather predictions.

The quality of a numerical model for the atmosphere or the ocean depends on two major components. On the one side, the differential equations which describe fluid motion are solved numerically in the dynamical core of the model. On the other side, physical processes that cannot be resolved with the effective resolution of the numerical model are imitated through artificial terms that are added to the equations of motion. Since these terms need to be adjusted by parameters, this part of the model is called sub-grid-scale parameterization.

This thesis will focus on dynamical cores of numerical models for atmosphere and ocean. In particular, we investigate the discretization and properties of the two dimensional shallow-water equations. The shallow-water equations are derived by vertical integration of the three-dimensional equations of motion, and describe the dynamics of a fluid layer. Since both atmosphere and ocean have a much larger extent in the horizontal than in the vertical direction, the shallow-water equations offer a meaningful first test ground for investigations of dynamical cores of full atmosphere and ocean models.

In the three major parts of this thesis, we investigate a new discretization technique

for weather or climate models, the use of grid refinement in global ocean and atmosphere modeling, and the representation and mechanism of boundary separation in ocean modeling. The following three subsections will give a short introduction to the background of each of these topics, and state the most important research questions that will be answered within this thesis.

1.1 Horizontal discretization in atmosphere and ocean models

A perfect dynamical core of an atmosphere or ocean model provides an accurate description of the equations of motion, numerical stability, the maintenance of important conservation constraints, positive definiteness of tracers, little numerical diffusion, high computational efficiency, and it is free of spurious modes.

To discretize the horizontal part of the equations of motion in state-of-the-art atmosphere and ocean models, three types of discretization methods are mainly used:

1. In **finite difference methods**, the continuous physical fields are approximated on distinct grid points. Spatial derivatives of the physical fields are computed through difference quotients that evaluate the differences of the field values and the distances between neighboring grid points. The degrees of freedom of the scalar fields, of the zonal, and of the meridional velocity are typically located on different grid points – this is called staggering. Different staggering schemes show different behavior for wave propagation and conservation properties.

   While finite difference methods are fairly easy to implement and computationally cheap, they show two major drawbacks. First, the point representation of the physical fields does not allow a mathematically sound description of sub-grid-scale structures. Second, since the methods require the use of structured lattices, finite difference methods typically use structured longitude/latitude grids for global simulations. These grids do not offer a uniform coverage of the sphere, since the grid cells get smaller towards the poles. This is not optimal, since the length of time spacing is typically limited by the length of the smallest grid edge. Furthermore, the lines of grid points at the latitude of the north and south pole shrink to single points. This is called 'pole problem'. For an ocean model the pole problem can be avoided by rotating the grid, and putting the poles of the grid onto land masses. This is not possible for an atmosphere model.

2. In **hybrid finite volume/finite difference methods**, the domain is divided into non-overlapping grid cells. Finite volume methods work with a so-called weak form of the equations. In a weak form, the differential equations are multiplied with test functions and integrated over the volume. In finite volume methods, the test functions are set to be one inside a specific grid cell, and zero elsewhere.

The integrated divergence or curl of a physical vector quantity inside a grid cell can be represented by fluxes of the quantity through or along the cell edges, via the Gauss or Stokes theorem.

In hybrid finite volume/finite difference methods, the scalar quantities are assumed to be constant over a grid cell, while the velocity (or momentum) field is defined by normal components on the cell edges. This description has the advantage to allow a direct representation of fluxes between neighboring grid cells, which offers direct mass conservation. The description has the disadvantage that the tangential component of the velocity field on the grid edges needs to be reconstructed from the normal components of velocity on neighboring edges, to evaluate the shear and the Coriolis force of the momentum equation. This reconstruction is typically a difficult operation with respect to energy and momentum conservation, the order of accuracy, and computational efficiency, especially on unstructured grids. In general, it is difficult to construct hybrid finite volume/finite difference methods with higher-order accuracy.

The hybrid finite volume/finite difference schemes work on unstructured grids, such as the quasi-uniform icosahedral grid on the sphere, and allow grid refinement procedures in which the existing grid points are moved towards regions of specific interest (see for example Ringler et al. 2011). Still, the geometric flexibility is limited due to the need of the so-called dual grid – the grid one obtains when connecting the cell centers of a given grid.

3. In **spectral methods** the equations of motion are solved in Fourier space. For spherical applications, spherical harmonics serve as basis functions. Spatial derivatives are calculated easily through multiplications in Fourier space, and the derivatives of the basis functions are known by analytical description. To advect tracers, or to post-process the model data, the physical fields need to be transferred back to physical space. Spectral methods are usually not used for ocean models, since it is very difficult to describe coast lines with the non-local basis functions.

   While spectral methods offer a good representation of the global atmosphere in low resolution models and allow a good measure of the numerical accuracy through the truncation level, the non-local description of the physical fields can lead to immediate non-local interactions, and the representation through basis functions can lead to spurious small-scale wave patterns (Gibbs phenomenon). The major problem for the use of spectral methods in high-resolution atmospheric modeling is the computational cost for the Legendre transformation needed for the mapping process between Fourier and physical space, which increases fast with resolution.

In this thesis, we investigate another type of discretization methods which is used extensively in numerous CFD applications, but – till today – only very rarely used for global atmosphere or ocean models: The group of finite element methods (Giraldo et al. 2002; Danilov et al. 2004; Nair et al. 2005; Giraldo 2006; Läuter et al. 2008). Here, the prognostic quantities are expanded into sets of local basis functions. The basis functions extend either over a single, or very few neighboring grid cells. The choice of the basis functions is very important and should be adapted to the requirements for a specific finite element model, since different basis functions lead to different properties of the dynamics and the performance of the model. The polynomial orders of the used basis functions offer a sound mathematical error description.

Similar to finite volume methods, finite element methods work with a weak form of the equations. Therefore, the differential equations are multiplied with test functions, and integrated over the volume of the domain. In difference to finite volume methods, the test functions are typically not constant within a grid cell. The test functions can be expanded into the same sets of basis functions as used to describe the physical fields – these methods are called Bubnov-Galerkin finite element methods – or they can be expanded into an approximation space different from the one spanned by the basis functions – these methods are called Petrov-Galerkin finite element methods.

Compared to the discretization methods described above, the major advantages of finite element methods are the local higher order representation of the physical fields, and the highest geometric flexibility for the use of unstructured grids and grid refinement. The major disadvantage is the higher computational cost per grid cell, compared to finite difference or finite volume methods. Still, finite element methods offer a higher internal resolution inside the grid cells, and it is not clear how the computational performance per effective resolution compares between the methods.

In finite element methods, a simulation on fewer grid cells with higher-order basis functions might result in the same effective resolution as a simulation on many grid cells with lower-order basis functions, but less grid cells will degrade the representation of topography and coast lines. Therefore, low-order finite element methods seem to be more suitable for global modeling than high-order methods. Unfortunately, it is difficult to find a low-order finite element approach that is able to represent the geostrophic balance between the Coriolis and the pressure gradient terms of the momentum equation, and satisfies a necessary condition for stability in finite element discretization methods – the Ladyzhenskaya-Babuska-Brezzi-condition (LBB-condition) – at the same time. The standard low-order finite element methods used in Computational Fluid Dynamics typically fail either to represent the geostrophic balance or to fulfill the LBB-condition, which leads to spurious modes (see for example Le Roux et al. 1998). Spurious modes destabilize the model or necessitate the use of numerical filtering. Additional to the two constraint above, finite element models for geophysical applications should provide two inertia-gravity wave modes for each Rossby wave mode. To this end, the perfect

choice would be to have twice as many degrees of freedom for the velocity field than for the scalar field.

A hybrid finite element approach that combines a second order continuous representation for the scalar field with a first order discontinuous representation for the velocity field – the $P_1^{DG}P_2$ finite element approach – was proposed as a potential candidate to form the dynamical cores of future weather or climate models (Cotter et al. 2009b). It was shown that the element is LBB-stable and able to represent the geostrophic balance (Cotter et al. 2009a,b). The $P_1^{DG}P_2$ finite element does not show spurious pressure or Rossby modes; it shows spurious inertial oscillations, but these do not propagate (Cotter and Ham 2011). The element offers direct mass conservation. While there exists extensive literature on how to obtain stable finite element models when only continuous or only discontinuous field representations are used, it is not obvious how to obtain an adequate model setup for the hybrid continuous/discontinuous $P_1^{DG}P_2$ element.

The $P_1^{DG}P_2$ finite element has not been used to develop a shallow-water model in spherical geometry. Therefore, we study the following research questions in the first part of this thesis (Chapter 2):

- Can we develop a stable shallow-water model setup on the sphere, using the $P_1^{DG}P_2$ finite element approach?
- What is the best way to introduce spherical geometry to a finite element model?
- How does a $P_1^{DG}P_2$ finite element model compare to other models, such as the hybrid finite volume/finite difference ICON shallow-water model (Rípodas et al. 2009)?

1.2 Grid refinement in atmosphere and ocean models

Grid refinement in the vertical direction is used successfully in most of the state-of-the-art weather and climate models. The distance between neighbored grid layers is typically decreasing towards the sea surface in ocean and atmosphere models. Still, in most of the dynamical cores of today's weather or climate models the only possibility to use grid refinement in the horizontal direction is via local nesting. This will probably change with the next generation of models based on hybrid finite volume/finite difference or finite element methods.

In global modeling, grid refinement in the horizontal direction could be used to increase the resolution in a specific region of interest – such as a single country or continent, arctic or tropical regions – or it could be used to improve the representation of important local features that have a large impact on the whole simulation – such as boundary currents, sea overflows, islands, and deep water formations in an ocean model; and mountains, tropical cyclones, and convection areas in an atmosphere model.

Still, a large part of the GFD community is skeptic towards the use of horizontal grid refinement. There are three major concerns against the use of grids with variable resolution in the horizontal direction: First, grid refinement can lead to reflection and scattering of waves at the transition between coarse and fine parts of a refined grid. Second, when a small area of the grid is refined, a smaller time step is needed for the whole simulation, due to the change of the size of the smallest grid cell. Third, it will be difficult to adjust sub-grid-scale parameterization schemes on refined grids, since physical processes might be resolved on the fine, but not on the coarse parts of a grid with variable resolution.

While the three concerns are reasonable at first sight, there are counter arguments that put them into another perspective. First, the use of grid refinement is well established in many applications of CFD, which are similar to GFD applications in many aspects. Here, grid refinement often leads to a significant improvement of the results, or a significant reduction of the numerical cost. In these applications wave scattering and reflection at the transition between coarse and fine parts of the grid are well known, but they do not cause severe problems that would negate the advantages. Second, the concern about smaller time steps can be addressed by the used time stepping scheme. The use of semi-implicit or implicit time stepping schemes can reduce the need for smaller time steps for the whole simulation. One could think about local time stepping methods, and the use of an increased number of intermediate time steps to solve for the fast terms in semi-implicit methods within the refined areas of a grid. Third, in the longitude/latitude grids used in finite difference methods, the zonal distance of grid points scales linearly with the cosine of the latitude. A grid cell at the equator is approximately five times larger than a grid cell at 80° North. For these models it is already necessary and possible to adjust the sub-grid-scale parameterization schemes to the local resolution.

In general, it is more difficult to show the advantages of grid refinement in GFD than in CFD. In contrast to typical applications in CFD, the simulation of weather and climate models do not converge with resolution, and have no reference solution. Grid refinement will change the results of a model run, but it will be difficult to analyze if the results are improved or degraded.

An analytical investigation of the error caused by grid refinement appears to be hardly possible for geophysical models in two or three dimensions, based on nonlinear, viscous equations, and discretized on unstructured grids. Still, it is crucially important to ensure that the wave propagation properties and the turbulent cascade are not disturbed by grid refinement, before using refined grids for geophysical applications. Geostrophic balance and conservation properties need to be maintained on the refined grids as well.

A quantification of the errors caused by grid refinement is difficult. Benchmark tests for spurious behavior are not existing. Therefore, we study a number of test setups

we developed to understand and quantify the errors and improvements caused by grid refinement. We study the following research questions in the second part of this thesis (Chapter 3):

- What is the influence of grid refinement on small- and large-scale flow patterns?
- Is the ability to represent the geostrophic balance and the representation of turbulent cascades influenced by grid refinement in a $P_1^{DG}P_2$ finite element model?
- In which applications can grid refinement improve the simulations of a $P_1^{DG}P_2$ shallow-water model?

1.3 Boundary currents and boundary separation in ocean models

The properties of the coast line in numerical ocean models are fairly different from the properties of the real-world coast line. This is mainly caused by the coarse resolution of today's ocean models, in which the coast line is represented by straight edges of the length of the grid spacing. It is therefore not surprising that numerical models have difficulties to represent the separation of boundary currents – such as the separation of the Gulf stream – correctly. In standard ocean models, the separation point of the Gulf stream tends to overshoot the separation point in the real world. State-of-the-art high-resolution model simulations, with a grid resolution of $1/10^\circ$ or higher, achieve a significant improvement for the representation of Gulf stream separation (Bryan et al. 2007; Chassignet and Garrao 2001). However, high-resolution does not guarantee a proper representation of the Gulf stream. The separation point remains sensitive to changes in the model setup, such as changes in viscosity parameterization (Bryan et al. 2007). In numerical models, the mechanism of boundary separation remains poorly understood. There is no recipe to obtain a realistic representation of boundary currents and boundary separation in ocean models (see Chassignet and Marshall 2008, for an overview).

The numerical representation of boundary currents is strongly dependent on the used boundary conditions, the used sub-grid-scale parameterization scheme, and the representation of the coast line. In turn, the boundary conditions and the representation of the coast line are dependent on the used discretization method. In finite difference methods, the grid point representation allows only a poor representation of the boundary conditions and the coast line. If longitude/latitude grids are used, neighbored grid edges are either aligned with each other, or they span a right angle; staircase patterns are apparent. Due to the use of staggering, the effective boundary conditions can depend on the alignment of the coast line with the grid axis (see Adcroft and Marshall

1998, for the analysis of an Arakawa C-grid). These problems should not appear in finite element models, in which the velocity field is defined as a two-dimensional vector quantity all along the coast. Furthermore, finite element models allow the use of boundary conforming grid generators in which the boundary grid points are aligned to the coast line.

In Fluid Dynamics, boundary separation of steady flows can be described by the classical theory of Prandtl (Prandtl 1904). But the mechanism of separation of unsteady flows – such as the separation of the Gulf stream – is still not sufficiently understood, and a clear, widely accepted, and easily applicable definition of boundary separation points in unsteady flows is still missing. Recently, new theories were developed for unsteady flow separation, which are developed from dynamical systems theory, or based on considerations of flow topology (see for example Haller 2004; Ghil et al. 2004; Lekien and Haller 2008).

An analysis of the properties of boundary currents and boundary separation in finite element models with realistic coast lines for ocean modeling, a detailed study of the discretized physical fields along a coast line as it is used in ocean models, and a test of the applicability of the theories by Haller, Lekien and Haller, and Ghil et al., in ocean modeling has not been done. Therefore, we study the following research questions in the third part of this thesis (Chapter 4):

- How good is the numerical representation of boundary currents in the $P_1^{DG}P_2$ finite element shallow-water model?
- Can we find proper criteria to detect boundary separation points in a finite element shallow-water model, for no-slip and free-slip boundary conditions?
- What are the properties of separation points of Gulf stream type flows in the $P_1^{DG}P_2$ finite element shallow-water model?

1.4 Thesis Outline

The Chapters 2, 3, and 4 of this thesis are written in the style of journal publications. As a consequence, they contain their own abstract, introduction, and conclusions, and can be read independently of one another. While Chapter 2 has been published already, Chapter 3 and Chapter 4 are in preparation for submission. For editorial consistency, references to the publication underlying Chapter 2 have been changed to references to the respective Chapter.

- In **Chapter 2**, we develop a finite element shallow-water model on the sphere. The used $P_1^{DG}P_2$ finite element approach is a new candidate to form the dynamical cores of future weather or climate models, since it has the remarkable property

to fulfill a stability criteria for finite element methods (the LBB conditions) and to hold the geostrophic balance, at the same time. Furthermore, we evaluate the use of the stereographic projection in global finite element modeling. The model results are analyzed with respect to their error convergence, conservation properties, and energy spectra. This part of the thesis is published in the *Journal of Computational Physics* (Düben et al. 2012).

- In **Chapter 3**, we study the use of grid refinement in geophysical modeling. We use the finite element model developed in Chapter 2 and perform model simulations for a set of six test cases, that we particularly arranged to investigate the influence of local grid refinement. We study the scattering and reflection at the transition between coarse and fine parts of a grid, and the influence of grid refinement on the representation of geostrophic balance and turbulent cascades. Furthermore, we investigate the scope of improvements possible for simulations of flow over topography, local wave patterns, and western boundary currents. This part of the thesis is currently being prepared for submission.

- In **Chapter 4**, we study boundary currents and boundary separation in a global finite element shallow-water model, with no-slip or free-slip boundary conditions. We evaluate the influence of local resolution, eddy viscosity, the grid structure, and the boundary conditions on the numerical representation of boundary currents, and try to identify proper criteria to detect boundary separation points in ocean modeling. To find proper criteria, we study the physical fields along the coast line, and evaluate classical and recent theories for flow separation in Fluid Dynamics. This part of the thesis is currently being prepared for submission.

- In **Chapter 5**, we give a short summary of the main findings of the thesis, and offer an Outlook.

Chapter 2

A discontinuous/continuous low-order finite element shallow-water model on the sphere

We study the applicability of a new finite element in atmosphere and ocean modeling. The finite element under investigation combines a second order continuous representation for the scalar field with a first order discontinuous representation for the velocity field and is therefore different from continuous and discontinuous Galerkin finite element approaches. The specific choice of low-order approximation spaces is attractive because it satisfies the Ladyzhenskaya-Babuska-Brezzi condition and is, at the same time, able to represent the crucially important geostrophic balance.

The finite element is used to solve the viscous and inviscid shallow-water equations on a rotating sphere. We introduce the spherical geometry via a stereographic projection. The projection leads to a manageable number of additional terms, and the associated scaling factors can be exactly represented by second order polynomials.

We perform numerical experiments considering steady and unsteady zonal flow, flow over topography, and an unstable zonal jet stream. For ocean applications, the wind driven Munk gyre is simulated. The experiments are performed on icosahedral geodesic grids and analyzed with respect to convergence rates, conservation properties, and energy and enstrophy spectra. The results match quite well with results published in the literature and encourage further investigation of this type of element for three-dimensional atmosphere/ocean modeling.

2.1 Introduction

Finite element schemes are successfully employed in numerous computational fluid dynamics applications. Finite element methods rely on a powerful mathematical apparatus and offer a good representation of the physical fields that are approximated using sets of basis functions of chosen accuracy. Finite element methods are applicable to unstructured grids and can accommodate grid refinement.

Today most dynamical cores of global atmosphere and ocean models are based on finite difference, or spectral transform schemes – mostly due to the ease of implemen-

tation and computational efficiency (Bryan 1969; Roeckner et al. 2003). Compared to those discretization methods, finite element schemes allow more flexibility with regard to unstructured or locally refined grids and can approximate physical fields with higher order polynomials. There are dynamical cores of global ocean or atmosphere models based on finite element schemes using continuous low-order finite element methods (Danilov et al. 2004), spectral elements (Taylor et al. 1997), or Discontinuous Galerkin (DG) finite element methods (Giraldo et al. 2002; Giraldo 2006; Nair et al. 2005; Läuter et al. 2008).

Global scale presents special challenges for the dynamical core of an atmospheric or ocean model. In a finite element framework, four important properties need to be considered:

1. The core needs to enable high-resolution simulations.

2. To support a smooth representation of topography and coastlines, one should be able to use very small grid cells. The second property is different to the first one since the internal resolution inside the grid cells can vary for different discretization schemes.

3. The core must be able to represent the geostrophic balance between the Coriolis force and the pressure gradient force.

4. The element must satisfy the Ladyzhenskaya-Babuska-Brezzi-condition (LBB-condition) - a necessary condition for stability of the discretization scheme.

The first two properties suggest low-order elements. Unfortunately, it is difficult to find a low-order element that fullfills the properties three and four at the same time. Failing in one of them leads to spurious modes (Le Roux et al. 1998). Therefore, continuous low-order finite element methods often require stabilization schemes (Danilov et al. 2004).

A hybrid finite element approach that combines a second order continuous representation for the scalar field with a first order discontinuous representation for the velocity field ($P_1^{DG}P_2$) was proposed as a potential candidate to combine the four properties above. It was shown for the linear equations that the element is LBB-stable and is able to represent the geostrophic balance (Cotter et al. 2009a,b). The analysis of the $P_1^{DG}P_2$ element in terms of a Helmholtz decomposition for the linearized shallow-water equations showed that the element has no spurious pressure or Rossby modes. Spurious modes occur in the least harmful place via inertia oscillations that do not propagate (Cotter and Ham 2011).

In this paper we contribute to the understanding of the $P_1^{DG}P_2$ element. We use the element to solve the spherical shallow-water equations with and without viscous dissipation and on unbounded domains as well as on domains with lateral boundaries.

The solutions are analyzed with respect to their convergence, conservation properties, and energy spectra.

While there exists extensive literature on how to obtain stable finite element models when only continuous or only discontinuous field representations are used, it is not obvious how to obtain an adequate model setup for the hybrid continuous/discontinuous $P_1^{DG}P_2$-element. As opposed to continuous finite element configurations, we need to solve a Riemann problem at cell boundaries due to the discontinuous velocity field, and, for a stable model setup, we need to perform a partial integration of the nonlinear divergence term in the scalar equation. As opposed to typical DG approaches, we use the non-conservative form of the shallow-water equations and non-orthogonal Lagrange polynomials as basis functions. Since the continuous scalar field is well defined on cell boundaries, our Riemann problem reduces to two dimensions for the two components of the velocity field, this is different to DG methods. Except for the Riemann solver, our finite element configuration is similar to the one presented in Comblen et al. (2010) for a $P_1^{DG}P_2$ finite element model on the plane. In Comblen et al. (2010) the weak form of the equations was derived from the non-conservative shallow-water equations while the three-dimensional Riemann solver for velocity and scalar fields was deduced from the conservative form.

The introduction of the spherical geometry for global finite element methods requires some care. To develop the physical fields into sets of basis functions, the triangles in physical space need to be mapped onto a reference triangle on which the basis functions are defined. On the sphere, the geometry of the physical triangles is given by trigonometric functions and cannot be mapped exactly onto a reference triangle, which is typically defined on the plane. In the literature, three different approaches can be found to introduce curved manifolds, such as the sphere, to finite element models. In the first approach, the differential equations are written for the curved manifold. This is done in the case of the cubed sphere, for example (Ronchi et al. 1996). In the second approach, the differential equations are formulated in the three-dimensional space and a global Cartesian coordinate system is considered. The vector fields are forced to stay on the manifold via constraints (Giraldo 1997). In the third approach, the vector fields are written in the local tangent basis while the fluxes and spatial operators are expressed in the three dimensional Cartesian basis (Bernard et al. 2009).

We propose the use of the stereographic projection to introduce the spherical geometry to global finite element models. The projection is part of the first approach mentioned above. It has already been used for finite difference and finite volume methods (Phillips 1957; Chen and Kuo 1986; Lanser et al. 2000, CCSR Ocean Component Model). In the stereographic projection, the sphere is projected from one of the poles onto a plane at the opposite side of the sphere. The pole itself is mapped to infinity. Global circulation models either use a combination of two stereographic projections from each pole that are connected at the equator or two stereographic projection from

each pole that are connected to a Mercator projection in tropical regions (Browning et al. 1989; Phillips 1957).

For an ocean model, it is sufficient to use one projection since the pole can be placed on land. For a global atmosphere model, we use two projections from each pole that are connected at the equator. The scaling factors that appear can be represented exactly by second order polynomials. The projection leads to a manageable number of additional terms in the differential equations.

In section two, we give an overview of the model setup, including the equations of motion, the discontinuous/continuous finite element discretization, and the incorporation of the spherical geometry. In section three, we apply the model to the standard test set for global shallow-water models and a Munk gyre ocean test case. In section four, we present a summary and conclusions.

2.2 Model setup

2.2.1 The viscous shallow-water equations

The viscous shallow-water equations can be written in several different forms which are analytically equivalent but have different properties when discretized.

One of those forms is the non-conservative form

$$\partial_t \mathbf{u} + \mathbf{u} \cdot (\nabla \mathbf{u}) + f\mathbf{k} \times \mathbf{u} + g\nabla h - \frac{1}{H}\nabla \cdot (H\nu (\nabla \mathbf{u})) = \boldsymbol{\tau}, \tag{2.1}$$

$$\partial_t h + \nabla \cdot (H\mathbf{u}) = 0, \tag{2.2}$$

where $\mathbf{u}$ is the two dimensional velocity vector, f is the Coriolis parameter, $\mathbf{k}$ is the vertical unit vector, g is the gravitational acceleration, ν is the eddy viscosity, $\boldsymbol{\tau}$ is a forcing term (for example, bottom friction or wind stress in ocean applications), h is the surface elevation, and H is the height of the fluid column given by $H = h - h_b$, where h_b is the bathymetry. The prognostic variables are the height and the velocity. Viscosity is not needed for stability reasons; we incorporated it for the sake of completeness.

In this work, we utilize three different types of boundary conditions. For the inviscid case, we introduce no normal flow boundary conditions ($\mathbf{u} \cdot \mathbf{n} = 0$ on $\partial\Omega$). For the viscous case, we either introduce no-slip ($\mathbf{u} = 0$ on $\partial\Omega$) or free-slip boundary conditions ($\mathbf{u} \cdot \mathbf{n} = 0$ and $\partial_{\mathbf{n}}\mathbf{u} = 0$ on $\partial\Omega$).

2.2.2 The discontinuous/continuous finite element discretization

The weak form

We divide the domain Ω into non-overlapping triangular grid cells E_i ($\bigcup_{i=1}^{N} E_i = \Omega$, $E_i \cap E_j = \emptyset$ for $i \neq j$ and $i, j = 1, 2, ..., N$). For each grid cell, we multiply the equations

(2.1) and (2.2) with arbitrary smooth test functions ($\phi_{\boldsymbol{u}}$ and ϕ_h) and integrate by parts to obtain

$$\begin{aligned}
\partial_t \int_{E_i} \mathbf{u}\phi_{\boldsymbol{u}}\,dx + \int_{\partial E} \begin{pmatrix} u^2 n_x + uvn_y \\ uvn_x + v^2 n_y \end{pmatrix} \phi_{\boldsymbol{u}}\,dS - \int_E \mathbf{u}\left(\nabla\cdot(\mathbf{u}\,\phi_{\boldsymbol{u}})\right)dx \\
+ \int_{E_i} (f\mathbf{k}\times\mathbf{u})\,\phi_{\boldsymbol{u}}\,dx + \int_{\partial E_i} gh\phi_{\boldsymbol{u}}\mathbf{n}\,dS - \int_E gh\,(\nabla\phi_{\boldsymbol{u}})\,dx \\
- \int_{\partial E_i} \nu\,(\nabla\mathbf{u})^{\mathrm{T}}\cdot\mathbf{n}\,\phi_{\boldsymbol{u}}\,dS + \int_{E_i} \nu\,(\nabla\mathbf{u})^{\mathrm{T}}\,\nabla\phi_{\boldsymbol{u}}\,dx \\
- \int_{E_i} \nu\frac{1}{H}\,(\nabla\mathbf{u})^{\mathrm{T}}\,(\nabla H)\,\phi_{\boldsymbol{u}}\,dx = \int_{E_i} \boldsymbol{\tau}\phi_{\boldsymbol{u}}\,dx, \qquad (2.3)
\end{aligned}$$

$$\partial_t \int_{E_i} h\phi_h\,dx + \int_{\partial E_i} H\mathbf{u}\cdot\mathbf{n}\phi_h\,dS - \int_{E_i} H\mathbf{u}\cdot\nabla\phi_h\,dx = 0, \qquad (2.4)$$

where $\mathbf{n}$ is the exterior unit normal vector at the boundary of the grid cell E_i.

We perform partial integration of the gravity forcing and the advection term in the velocity equation and of the nonlinear divergence term in the height equation. This is a typical approach for discontinuous Galerkin methods.

Assuming that the continuous solution is smooth we can sum over all cells and obtain the weak form of the equations

$$\begin{aligned}
\sum_{i\in I_E} \partial_t \int_{E_i} \mathbf{u}\phi_{\boldsymbol{u}}\,dx + \sum_{i\in I_{int}} \int_{\gamma_i} \begin{pmatrix} u^2 n_x + uvn_y \\ uvn_x + v^2 n_y \end{pmatrix} [\phi_{\boldsymbol{u}}]\,dS + \sum_{i\in I_{ext}} \int_{\gamma_i} \begin{pmatrix} u^2 n_x + uvn_y \\ uvn_x + v^2 n_y \end{pmatrix} \phi_{\boldsymbol{u}}\,dS \\
- \sum_{i\in I_E} \int_{E_i} \mathbf{u}\left(\nabla\cdot(\mathbf{u}\,\phi_{\boldsymbol{u}})\right)\,dx + \sum_{i\in I_E} \int_{E_i} (f\mathbf{k}\times\mathbf{u})\,\phi_{\boldsymbol{u}}\,dx \\
+ \sum_{i\in I_{int}} \int_{\gamma_i} g\,[\phi_{\boldsymbol{u}}]\,h\mathbf{n}\,dS + \sum_{i\in I_{ext}} \int_{\gamma_i} g\phi_{\boldsymbol{u}} h\mathbf{n}\,dS \\
- \sum_{i\in I_E} \int_{E_i} g\,(\nabla\phi_{\boldsymbol{u}})\,h dx - \sum_{i\in I_{int}} \int_{\gamma_i} \nu\,(\{\nabla\mathbf{u}\})^{\mathrm{T}}\cdot\mathbf{n}\,[\phi_{\boldsymbol{u}}]\,dS \\
- \sum_{i\in I_{ext}} \int_{\gamma_i} \nu\,(\nabla\mathbf{u})^{\mathrm{T}}\cdot\mathbf{n}\,\phi_{\boldsymbol{u}}\,dS + \sum_{i\in I_E} \int_{E_i} \nu\,(\nabla\mathbf{u})^{\mathrm{T}}\,\nabla\phi_{\boldsymbol{u}}\,dx \\
- \sum_{i\in I_E} \int_{E_i} \nu\frac{1}{H}\,(\nabla\mathbf{u})^{\mathrm{T}}\,(\nabla H)\,\phi_{\boldsymbol{u}}\,dx = \sum_{i\in I_E} \int_{E_i} \boldsymbol{\tau}\phi_{\boldsymbol{u}}\,dx \\
+ \sum_{i\in I_{int}} \int_{\gamma_i} \nu\frac{(p+1)\,(p+2)}{l}\,[\mathbf{u}]\,[\phi_{\boldsymbol{u}}]\,dS, \qquad (2.5)
\end{aligned}$$

$$\sum_{i\in I_E} \partial_t \int_{E_i} h\phi_h \, dx + \sum_{i\in I_{int}} \int_{\gamma_i} H\mathbf{u}\cdot\mathbf{n}\,[\phi_h] \, dS + \sum_{i\in I_{ext}} \int_{\gamma_i} H\mathbf{u}\cdot\mathbf{n}\phi_h \, dS - \sum_{i\in I_E} \int_{E_i} H\mathbf{u}\cdot\nabla\phi_h \, dx = 0, \tag{2.6}$$

where we fix the direction of the normal vector $\mathbf{n}$ at the interior inter-element boundaries; [.] is the jump in a quantity across an edge (the sign depends on the direction of $\mathbf{n}$), {.} is the average of a quantity from both sides of an edge, I_E is the set of element indices, $\{\gamma_i, i \in I_{int}\}$ is the set of edges in the interior of Ω, and $\{\gamma_i, i \in I_{ext}\}$ are the edges on the exterior boundary of Ω.

We added a penalty term to equation (2.5) (the last term on the right hand side) that ensures the velocity field to be smooth enough at cell boundaries. Penalty terms push the model dynamics towards a desired constraint. The setup avoids severe impacts on the model dynamics that would be caused by a direct introduction of the constraint. It is known from discontinuous Galerkin methods, that the discontinuity can lead to model instabilities. Similar to discontinuous Galerkin methods the $P_1^{DG}P_2$ model needs a penalty term to stabilize the model setup for the viscous equations. The choice of the penalty term is non trivial. If it is too small, the solution is unstable. If it is too large, it will degrade the solution. In our model, we use the same penalty term as Comblen et al. (2010). p is the polynomial order of the finite element, and l is a typical length scale of the grid cell (Shahbazi 2005).

For no normal flow boundary conditions, we set the normal velocity flux at the boundary equal to zero. For free-slip boundary conditions, we set the normal velocity flux at the boundary equal to zero and drop the exterior surface integral in equation (2.5) which comes from the diffusion term. We introduce no-slip boundary conditions in a weak form by adding the following term to the right hand side of equation (2.5)

$$-\sum_{i\in I_{ext}} \int_{\gamma_i} \sigma\mathbf{u}\phi_{\boldsymbol{u}} \, dS. \tag{2.7}$$

This penalty term forces the velocity at the boundary towards zero. σ is the penalty parameter, here it is a constant value that needs to be adjusted experimentally. Additionally we set the normal velocity flux at the boundary equal to zero.

The integrals over external boundaries in equation (2.6) drop for each boundary condition since the flux through external boundaries is allways zero. When the velocity value at the boundary has been determined by solving the Riemann problem (see below), the integrals over interior edges in equation (2.6) disappear since test functions ϕ_h assume the same values on both sides, and the height of the fluid column H is continuous.

Approximation functions

We represent the primary unknowns velocity and height as linear combinations of basis functions

$$\mathbf{u} = \sum_{i=1}^{N_u} \mathbf{u}_i N_i \qquad \text{and} \qquad h = \sum_{i=1}^{N_h} h_i M_i.$$

In our discretization, we employ globally discontinuous piecewise linear Lagrange polynomials for the velocity field and globally continuous quadratic Lagrange polynomials for the height field. While the linear representation needs three degrees of freedom, the quadratic representation requires six degrees of freedom in each triangle. While the degrees of freedom of the continuous height field are shared with the surrounding cells, this is not the case for the discontinuous velocity fields (Figure 2.1). The overall number of degrees of freedom for the height field is reduced to about one third compared to a discontinuous Galerkin approximation in which the height field is represented by piecewise quadratic discontinuous basis functions. We follow the Bubnov-Galerkin finite element approach and set the test functions ϕ_u and ϕ_h to be equal to the basis functions N_i and M_i of the corresponding physical fields.

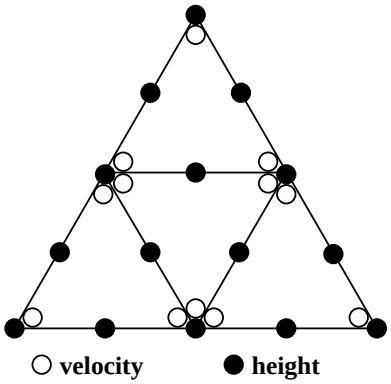

Figure 2.1: Node distribution of the Lagrange polynomials on the triangle for the velocity and the height fields.

A modified Riemann problem

In a DG approach, all physical fields are represented by discontinuous basis functions. The height fields and the two components of the velocity fields are not uniquely defined on interior boundaries between grid cells. The surface integrals must be replaced with suitable numerical fluxes obtained by solving the Riemann problem (LeVeque 1992). Since the height field is continuous in our approach, its value is well defined on the boundary. Thus the Riemann problem reduces to a two-dimensional problem for the

two components of velocity. This is different to the DG approach and to the $P_1^{DG}P_2$ finite element discretization in Comblen et al. (2010). The flux through the boundary of the grid cell is given by

$$\mathbf{F}(\mathbf{u},\mathbf{n}) = \begin{pmatrix} u^2 n_x + uvn_y \\ uvn_x + v^2 n_y \end{pmatrix}.$$

We solve the Riemann problem using the Lax-Friedrich method. The numerical flux is given by

$$\hat{\mathbf{F}}_L(\mathbf{n}_L,\mathbf{u}_L,\mathbf{u}_R) = \frac{1}{2}\left(\mathbf{F}(\mathbf{u}_L,\mathbf{n}_L) + \mathbf{F}(\mathbf{u}_R,\mathbf{n}_L)\right) + \frac{1}{2}|\hat{\lambda}|(\mathbf{u}_L - \mathbf{u}_R) = -\hat{\mathbf{F}}_R(\mathbf{n}_R,\mathbf{u}_L,\mathbf{u}_R).$$

Indices L and R indicate the two sides of the boundary; $\mathbf{n}_L$ (or $\mathbf{n}_R$) denotes an exterior unit normal vector to the cell with the corresponding index L (or R), and $\hat{\lambda}$ is the maximum absolute eigenvalue of the matrix

$$\begin{pmatrix} \frac{\partial F_x}{\partial u} & \frac{\partial F_x}{\partial v} \\ \frac{\partial F_y}{\partial u} & \frac{\partial F_y}{\partial v} \end{pmatrix} = \begin{pmatrix} 2un_x + vn_y & un_y \\ vn_x & un_x + 2vn_y \end{pmatrix}.$$

The eigenvalues are given by

$$\lambda_1 = un_x + vn_y \qquad \text{and} \qquad \lambda_2 = 2un_x + 2vn_y.$$

If the velocity field changes its sign along an edge of a triangle, $|\hat{\lambda}|$ stops being a polynomial function on the edge. In this case, the Lax-Friedrich flux is not calculated exactly, when numerical quadrature is used. Nevertheless, we assume the error to be small. Conservation properties are not affected since the flux is the same on both sides of the edge (with opposite sign).

2.2.3 The spherical geometry

Here we extend the $P_1^{DG}P_2$ finite element discretization to applications on the sphere by applying a stereographic projection. The sphere is projected from one of the poles onto a plane on the opposite side of the sphere (see Figure 2.2). We do not use the projections of the spherical edges as grid edges in our model runs (red lines in Figure 2.2). Instead we use straight edges connecting the projected vertices in the stereographic domain (green dashed lines in Figure 2.2). Therefore, our model works with planar triangles in the planar stereographic domain. A projection between the triangles in the numerical grid, and the reference triangle on which the finite element basis functions are defined, can be performed exactly by a linear mapping. Without the stereographic projection, we were not able to obtain a stable model using second order accuracy for the mapping between the spherical triangles and the planar reference triangle.

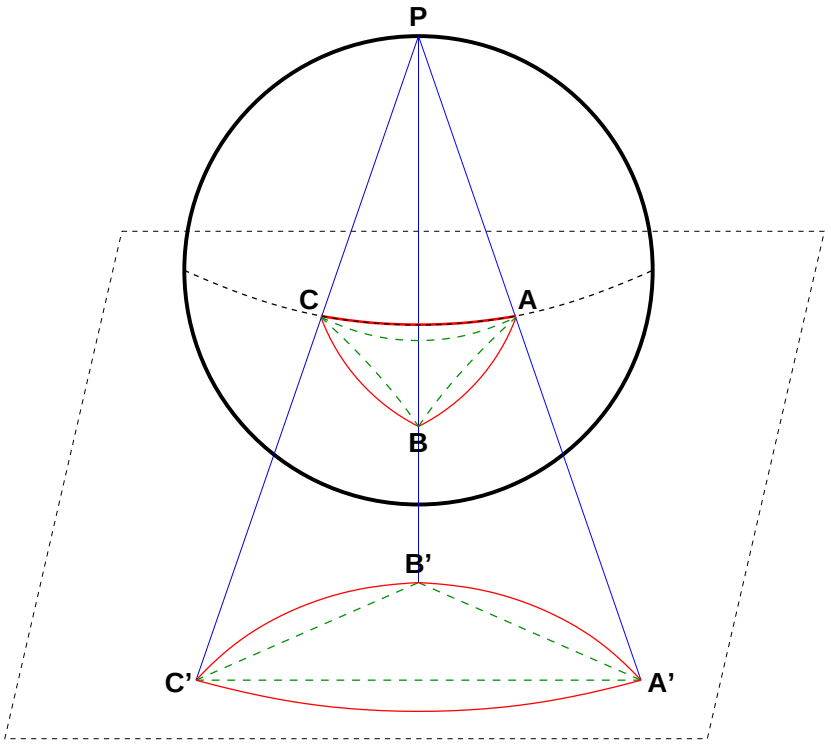

Figure 2.2: Sketch of the stereographic projections. The sphere is projected from the north pole onto a plane below the sphere. The continuous red lines show the edges of a triangle in the original grid on the sphere, and their projected counterparts. The dashed green lines show the edges used for numerical simulations, that are straight in the stereographic domain.

The stereographic projection leads to variations in the grid spacing dependent on the distance to the pole. Nevertheless, the velocity scales with the same factor as the grid spacing, and constraints concerning the maximal possible time step remain unchanged.

The stereographic projection is not able to represent the pole from which the sphere is projected, because this point is mapped to infinity. For an ocean model, this problem can be solved by putting the pole onto a landmass. In the case of an atmospheric model, the problem can be solved by using one projection from each pole and a transition zone between the projections at the equator. The coupling of two projections for the atmospheric model produces a small gap between the grid cells at the boundary between the two projections. The gap occurs because the dashed green lines at the equator of the sphere in Figure 2.2 bend in the opposite directions, when the northern and the southern projection are coupled. When mapping a grid edge at the boundary from the two projections back onto the sphere, the edge will be different, while the corresponding vertices are situated at the same positions. Therefore, the flux through the edges is

not identical for both subdomains. This leads to a small mass inconsistency. The error is decreasing with increasing resolution (see also subsection 2.3.2). It is not necessary that the coupling of the projections is located at the equator, but the error cannot be avoided by moving the transition zone.

Introducing the stereographic projection into the model involves rewriting the system of equations for the projection planes. This is done by introducing scale coefficients into the shallow-water equations. As shown in Williamson et al. (1992), the inviscid shallow-water equations in non-conservative form turn into

$$\partial_t U + \frac{U}{m}\partial_x U + \frac{V}{m}\partial_y U - fV + \left(V^2\partial_x \frac{1}{m} - UV\partial_y \frac{1}{m}\right) + \frac{g}{m}\partial_x h = \tau_x, \tag{2.8}$$

$$\partial_t V + \frac{U}{m}\partial_x V + \frac{V}{m}\partial_y V + fU - \left(VU\partial_x \frac{1}{m} - U^2\partial_y \frac{1}{m}\right) + \frac{g}{m}\partial_y h = \tau_y, \tag{2.9}$$

$$\partial_t h + \frac{U}{m}\partial_x H + \frac{V}{m}\partial_y H + \frac{H}{m}\partial_x U + \frac{H}{m}\partial_y V - HU\partial_x \frac{1}{m} - HV\partial_y \frac{1}{m} = 0, \tag{2.10}$$

where U and V are the velocities in the projected coordinate system, x and y are the Cartesian coordinates on the projection plane, and $1/m$ is the metric coefficient given by

$$\frac{1}{m} = \frac{2}{1 \pm \sin(\theta)},$$

dependent on the longitude λ and the latitude θ. We use '+' for the projection from the southern and '−' for the projection from the northern pole. Expressed in the coordinates of the projected plane $1/m$ is given by

$$\frac{1}{m} = \frac{x^2 + y^2 + 4a_e^2}{4a_e^2},$$

where a_e is the radius of the earth. Clearly, $\frac{1}{m}$ as well as its derivatives can be represented exactly by second order polynomials in x and y.

U and V are given by

$$U = m\frac{dx}{dt} = -u\sin(\lambda) \mp v\cos(\lambda),$$

$$V = m\frac{dy}{dt} = u\cos(\lambda) \mp v\sin(\lambda),$$

where u is the zonal, and v is the meridional velocity. When the sphere is projected out of the southern pole, the coordinate transformation is given by

$$\lambda = \begin{cases} \arccos\left(\frac{x}{R}\right), & \text{if } y \geq 0, \\ -\arccos\left(\frac{x}{R}\right), & \text{if } y < 0, \end{cases}$$

$$\theta = 2\arctan\left(\frac{2a_e}{R}\right) - \frac{\pi}{2}, \tag{2.11}$$

where $R = \left(x^2 + y^2\right)^{\frac{1}{2}}$. For the north pole projection, replace θ by $-\theta$ in (2.11). The inverse transformation to the Cartesian coordinates is given by

$$\begin{aligned} x &= \frac{a_e \cos(\lambda)\cos(\theta)}{m} \\ y &= \frac{a_e \sin(\lambda)\cos(\theta)}{m}, \end{aligned}$$

using the corresponding value of $1/m$.

The diffusion term valid for the shallow-water equation in the stereographic projection can be obtained by introducing the gradient and divergence operators written for the stereographic projection ∇_{St} into the diffusion term of the Cartesian shallow-water equations (2.1). The divergence operator in the stereographic coordinates is given by (Lanser et al. 2000)

$$\nabla_{St} \cdot \mathbf{U} = \frac{1}{m}\partial_x U + \frac{1}{m}\partial_y V - U\partial_x \frac{1}{m} - V\partial_y \frac{1}{m}.$$

The divergence operator can be split into two parts. The first two terms of the right hand side originate in the standard spatial derivatives multiplied with a scaling factor. The last two terms express the change of the scaling factor. The nabla operator has a similar structure.

Except for the immediate vicinity of the pole from which we project, the scaling factor changes very slowly with latitude. We assume that the spatial derivatives of the scaling factors that appear in (2.12) and in the corresponding formula for the gradient are negligible. Then the diffusion term reads as follows

$$\frac{1}{H}\nabla_{St} \cdot \left(H\nu\left(\nabla_{St}\mathbf{U}\right)\right) \approx \begin{pmatrix} \frac{\nu}{H\,m^2}\partial_x\left(H\partial_x U\right) + \frac{\nu}{H\,m^2}\partial_y\left(H\partial_y U\right) \\ \frac{\nu}{H\,m^2}\partial_x\left(H\partial_x V\right) + \frac{\nu}{H\,m^2}\partial_y\left(H\partial_y V\right) \end{pmatrix}. \tag{2.12}$$

The discretization of the shallow-water equations written for the stereographic projection is performed in the same way as explained in the previous subsection for the shallow-water equations in Cartesian space. In the finite element setup, the weak form of equations (2.8) – (2.10) with the added diffusion term (2.12) reads

$$\sum_{i\in I_E}\partial_t\int_{E_i}\mathbf{U}\phi_{\boldsymbol{U}}\,dx+\sum_{i\in I_{int}}\int_{\gamma_i}\frac{1}{m}\begin{pmatrix}U^2n_x+UVn_y\\UVn_x+V^2n_y\end{pmatrix}[\phi_{\boldsymbol{U}}]\;dS$$
$$+\sum_{i\in I_{ext}}\int_{\gamma_i}\frac{1}{m}\begin{pmatrix}U^2n_x+UVn_y\\UVn_x+V^2n_y\end{pmatrix}\phi_{\boldsymbol{U}}\,dS-\sum_{i\in I_E}\int_{E_i}\frac{\mathbf{U}}{m}\left(\nabla\cdot(\mathbf{U}\,\phi_{\boldsymbol{U}})\right)\,dx$$
$$+\sum_{i\in I_E}\int_{E_i}\begin{pmatrix}VV\partial_x\frac{1}{m}-UU\partial_x\frac{1}{m}-2UV\partial_y\frac{1}{m}\\-2UV\partial_x\frac{1}{m}+UU\partial_y\frac{1}{m}-VV\partial_y\frac{1}{m}\end{pmatrix}\phi_{\boldsymbol{U}}\,dx$$
$$+\sum_{i\in I_E}\int_{E_i}(f\mathbf{k}\times\mathbf{U})\,\phi_{\boldsymbol{U}}\,dx+\sum_{i\in I_{int}}\int_{\gamma_i}g\,[\phi_{\boldsymbol{U}}]\,\frac{h}{m}\mathbf{n}\,dS$$
$$+\sum_{i\in I_{ext}}\int_{\gamma_i}g\phi_{\boldsymbol{U}}\frac{h}{m}\mathbf{n}\,dS-\sum_{i\in I_E}\int_{E_i}g\,(\nabla\phi_{\boldsymbol{U}})\,\frac{h}{m}dx$$
$$-\sum_{i\in I_E}\int_{E_i}g\phi_{\boldsymbol{U}}h\nabla\frac{1}{m}dx-\sum_{i\in I_{int}}\int_{\gamma_i}\frac{\nu}{m^2}\left(\{\nabla\mathbf{U}\}\right)^{\mathrm{T}}\cdot\mathbf{n}\;[\phi_{\boldsymbol{U}}]\;dS$$
$$-\sum_{i\in I_{ext}}\int_{\gamma_i}\frac{\nu}{m^2}\left(\nabla\mathbf{U}\right)^{\mathrm{T}}\cdot\mathbf{n}\,\phi_{\boldsymbol{U}}\,dS+\sum_{i\in I_E}\int_{E_i}\frac{\nu}{m^2}\left(\nabla\mathbf{U}\right)^{\mathrm{T}}\nabla\phi_{\boldsymbol{U}}\,dx$$
$$-\sum_{i\in I_E}\int_{E_i}\frac{\nu}{m^2}\frac{1}{H}\left(\nabla\mathbf{U}\right)^{\mathrm{T}}(\nabla H)\,\phi_{\boldsymbol{U}}\,dx=\sum_{i\in I_E}\int_{E_i}\boldsymbol{\tau}\phi_{\boldsymbol{U}}\,dx$$
$$+\sum_{i\in I_{int}}\int_{\gamma_i}\nu\frac{(p+1)\,(p+2)}{l}\,[\mathbf{U}]\,[\phi_{\boldsymbol{U}}]\;dS-\sum_{i\in I_{ext}}\int_{\gamma_i}\sigma\mathbf{U}\phi_{\boldsymbol{U}}\,dS,\tag{2.13}$$

$$\sum_{i\in I_E}\partial_t\int_{E_i}h\phi_h\,dx+\sum_{i\in I_{int}}\int_{\gamma_i}\frac{H}{m}\mathbf{U}\cdot\mathbf{n}\,[\phi_h]\;dS+\sum_{i\in I_{ext}}\int_{\gamma_i}\frac{H}{m}\mathbf{U}\cdot\mathbf{n}\phi_h\,dS$$
$$-\sum_{i\in I_E}\int_{E_i}\frac{H}{m}\mathbf{U}\cdot\nabla\phi_h\,dx-\sum_{i\in I_E}\int_{E_i}2\,H\phi_h\mathbf{U}\cdot\nabla\frac{1}{m}\,dx=0.\tag{2.14}$$

2.3 Numerical results

We evaluate our model using the standard suite of global shallow-water test cases for the inviscid equation ($\nu=0$) as well as a non-linear Munk gyre test with boundaries for the viscous case.

Geodesic grids

For our numerical experiments, we use icosahedral geodesic grids (Baumgardner and Frederickson 1985), due to their quasiuniform coverage of the sphere. In principle,

Grid level	Number of cells	Averaged edge length on the sphere [m]	DOF for velocity component	DOF for height
1	320	1914397	960	642
2	1280	961256	3840	2562
3	5120	481137	15360	10242
4	20480	240632	61440	40962
5	81920	120324	245760	163842
6	327680	60163	983040	655362

Table 2.1: Properties of the triangular grids at different resolutions.

each spherical triangular grid could be used for simulations. The grids can be refined to the next level by bisecting the sides of the triangles; the new vertices are then projected onto the surface of the sphere (Figure 2.3). The properties of the grids used are summarized in Table 2.1. To calculate the area integrals on the triangles we use Gaussian quadrature rules of fifth order.

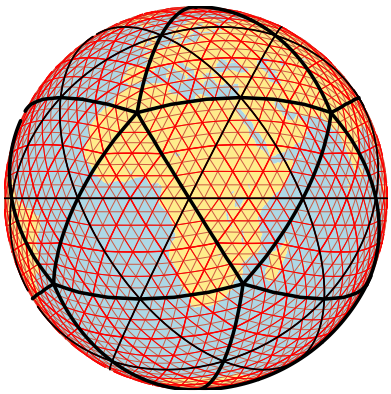

Figure 2.3: Icosahedral geodesic grid for different refinement levels.

Time discretization and linear solver

To discretize the evolution in time we use the explicit three level Adams-Bashforth time stepping. The equation

$$\partial_t \boldsymbol{\psi} = R(\boldsymbol{\psi}),$$

where R denotes the right-hand-side of the system, and $\boldsymbol{\psi}$ is the vector of prognostic variables, is discretized in time by

$$\boldsymbol{\psi}^{n+1} = \boldsymbol{\psi}^n + \Delta t \left(\frac{23}{12} R(\boldsymbol{\psi}^n) - \frac{4}{3} R(\boldsymbol{\psi}^{n-1}) + \frac{5}{12} R(\boldsymbol{\psi}^{n-2}) \right),$$

where $\boldsymbol{\psi}^i$ is the vector of state variables at the i-th time step.

We apply the time discretization to equations (2.13) and (2.14) and obtain a linear system of equations since we use Lagrange polynomials for the representation of the physical fields, and the mass matrix is non-diagonal. We obtain the new state vector $\boldsymbol{\psi}^{n+1}$ by solving the system of linear equations. To this end we could use a standart CG solver since the mass matrix is symmetric. However, we observed that a diagonal preconditioner which reduces the conditioning number of the matrix but turns the matrix into an unsymmetric one, in combination with a BiCGSTAB solver is faster. This speed up can be explained since the use of the stereographic projection, which is not area preserving, leads to triangles of various size, and increases the conditioning number of the mass matrix.

Evaluation

The results are analyzed with regard to the conservation of mass and energy, convergence in the L^1- and the L^2-norms, and the energy spectra. We calculate the global energy at timestep n using the following formula

$$E^n = \int_\Omega \left(\frac{1}{2} h^n \mathbf{u}^n \cdot \mathbf{u}^n + \frac{1}{2} g \left(h^n h^n - h_b^n h_b^n \right) \right) dx. \tag{2.15}$$

The global mass is given by

$$M^n = \int_\Omega \left(h^n - h_b^n \right) dx. \tag{2.16}$$

We calculate the integrals in equations (2.15) and (2.16) using Gaussian quadrature rules of at least fifth order. We compute the relative error for energy and mass at timestep n using the initial value of the corresponding variable as a reference

$$\eta_E \left(t_n \right) = \frac{\left| E^0 - E^n \right|}{E^0} \qquad \text{and} \qquad \eta_M \left(t_n \right) = \frac{\left| M^0 - M^n \right|}{M^0}.$$

2.3.1 Steady and unsteady solid body rotation

In this subsection, the convergence behavior of the developed model is evaluated by considering the height field error with increasing grid resolution. The global steady-state nonlinear zonal geostrophic flow test proposed in Williamson et al. (1992) (test case 2) and the unsteady solid body rotation test proposed in Läuter et al. (2005) (example 3) are simulated. The steady case specifies a zonal westerly flow with the maximum velocity of ca. 39 m/s and the fluid depth varying between 1000 and 3000 m.

Grid level	L^1-error	Order	L^2-error	Order
1	2.84e-03		3.08e-03	
2	2.42e-04	3.57	2.80e-04	3.48
3	2.32e-05	3.39	2.86e-05	3.30
4	2.59-06	3.16	3.21e-06	3.15
5	3.76e-07	2.78	4.58e-07	2.81

Table 2.2: Steady solid body rotation with $\alpha = 0$: L^1- and L^2-errors for the height field after five days and the order of convergence.

Velocity and height fields are initialized in such a way that the initial state is a stationary solution of the nonlinear shallow-water equations. The inclination of the westerly flow can be controlled by angle α between the axis of the solid body rotation and the polar axis of the spherical coordinate system. To balance the initial conditions, the value of the Coriolis parameter needs to be changed (details are given in Williamson et al. 1992). Tests were performed with $\alpha = 0$ and $\alpha = \frac{\pi}{2} - 0.05$.

The unsteady solid body rotation test is another example of solid body rotation with inclination. It represents a wave that travels westwards around the globe and reaches its initial position after one day of integration. In this case, the maximum velocity is ca. 39 m/s, and the fluid depth varies between 12000 and 14000 m.

Model runs for both test cases are performed, and the L^1- and L^2-errors of the height field are calculated following the equations

$$L^1(h) = \frac{\int_E |h^n - h_a^n|\, dx}{\int_E |h_a^n|\, dx} \qquad \text{and} \qquad L^2(h) = \sqrt{\frac{\int_E (h^n - h_a^n)^2\, dx}{\int_E (h_a^n)^2\, dx}},$$

where h^n is the computed height at timestep n compared to the analytical solution h_a^n.

Figure 2.4 shows the height fields for both test cases after five days of integration. Note that the height field did not change its shape compared to the initial condition.

Figures 2.5 and 2.6 show convergence of the height field for both test cases after five days of integration. The error decreases with increasing grid resolution.

Tables 2.2 - 2.4 show the convergence rates we have measured for the performed test cases. The unsteady and the solid body rotation tests with inclination show second order convergence whereas the simple steady test without inclination shows third order accuracy.

Though one would expect a convergence of up to order two due to the piecewise linear polynomials used for the velocity representation, it was found in Comblen et al. (2010) that the $P_1^{DG}P_2$-element shows super-optimal convergence of third order for the height field when a linear Stommel gyre testcase was considered but reverts to the second order convergence when nonlinearity comes into play. Using a Helmholtz decomposition for

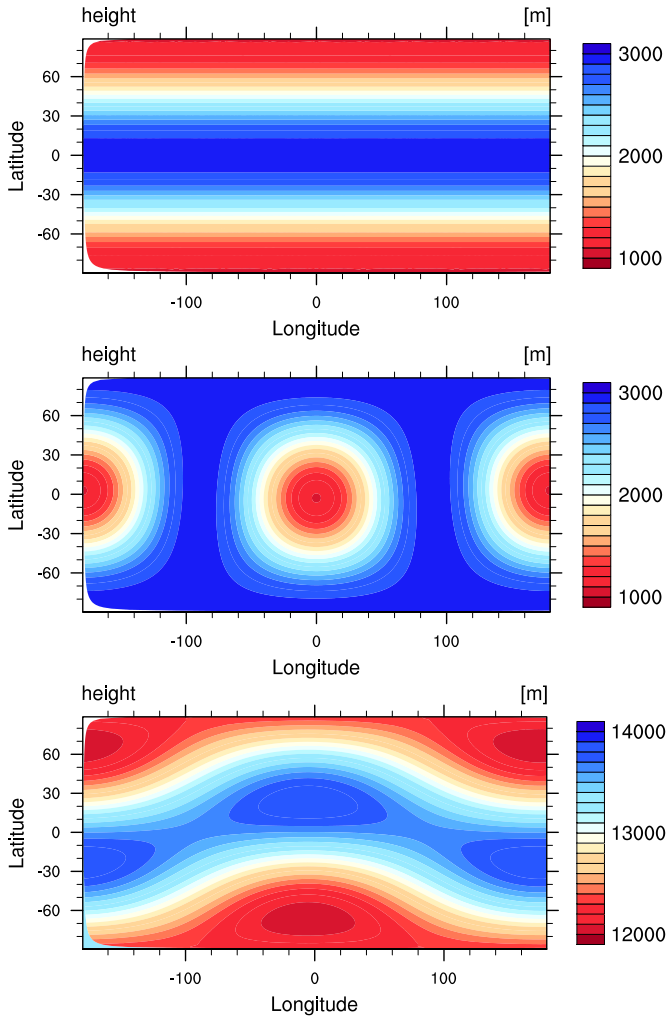

Figure 2.4: Global height field $[m]$ after five days for grid level 4. From top to bottom: Steady solid body rotation with $\alpha = 0.0$; steady solid body rotation with $\alpha = \frac{\pi}{2} - 0.05$; unsteady solid body rotation.

the linear shallow-water equations Cotter and Ham (2011) showed that the $P_1^{DG}P_2$-element exhibits third order convergence rates for inertia-gravity waves with f-plane approximation and for Rossby waves with β-plane approximation.

Figure 2.7 compares the L^2-error for the height field after ten days for the developed finite element model and ICONSWM, a shallow-water model based on a mixed finite volume/finite difference approach. The ICONSWM data was taken from Table 5 in Rípodas et al. (2009). The simulations were performed on the same grids. Although the finite element model appears to have a much smaller error, a direct comparison of the results is not quite fair since the finite element model uses circa three times as

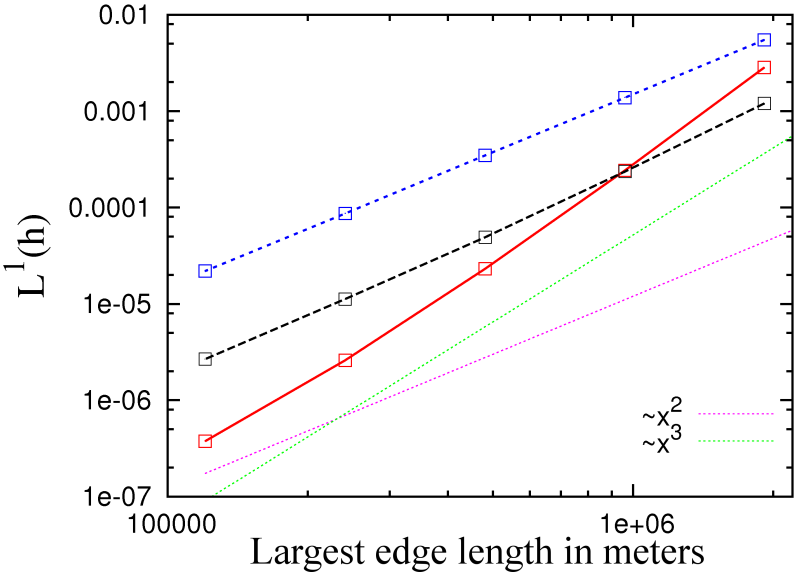

Figure 2.5: L^1-error of the height field for different grid resolutions after five days. Red continuous line: Steady state, $\alpha = 0.0$; Black dashed line: Steady state, $\alpha = \frac{\pi}{2} - 0.05$; Blue dotted line: Unsteady state.

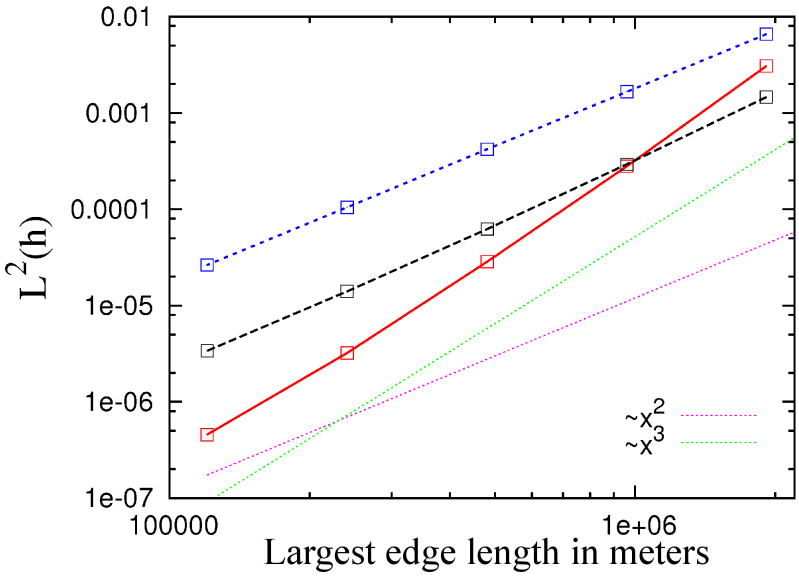

Figure 2.6: L^2-error of the height field for different grid resolutions after five days. Red continuous line: Steady state, $\alpha = 0.0$; Black dashed line: Steady state, $\alpha = \frac{\pi}{2} - 0.05$; Blue dotted line: Unsteady state.

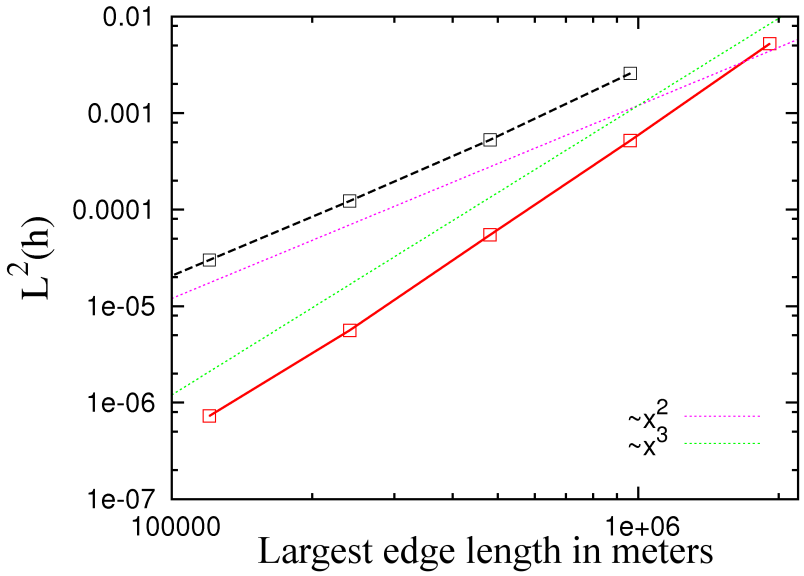

Figure 2.7: L^2-error of the height field for the steady state $\alpha = 0.0$ test for different grid resolutions after ten days. Red continuous line: the finite element model; Black dashed line: ICONSWM.

many degrees of freedom on the same grid and thus has a larger approximation space.

2.3.2 Rossby-Haurwitz wave

A detailed description of the Rossby-Haurwitz test can be found in the reference paper Williamson et al. (1992) (test case 6). It is based on the analytical solution of the nonlinear barotropic vorticity equations on the sphere. Although there is no comparable solution for the shallow-water equation the wave should travel in zonal direction and maintain its basic structure at least for the first fifteen days (Thuburn and Li 2000).

Grid level	L^1-error	Order	L^2-error	Order
1	1.20e-03		1.46e-03	
2	2.36e-04	2.36	2.94e-04	2.32
3	4.93e-05	2.27	6.24e-05	2.24
4	1.12e-05	2.14	1.40e-05	2.15
5	2.67e-06	2.07	3.38e-06	2.06

Table 2.3: Steady solid body rotation with $\alpha = \frac{\pi}{2} - 0.05$: L^1- and L^2-errors for the height field after five days and the order of convergence.

Grid level	L^1-error	Order	L^2-error	Order
1	5.48e-03		6.58e-03	
2	1.38e-03	2.00	1.67e-03	1.99
3	3.48e-04	1.99	4.20e-04	1.99
4	8.68e-05	2.00	1.05e-04	2.00
5	2.19e-05	1.99	2.64-05	1.99

Table 2.4: Unsteady solid body rotation: L^1- and L^2-error for the height field after five days and the order of convergence.

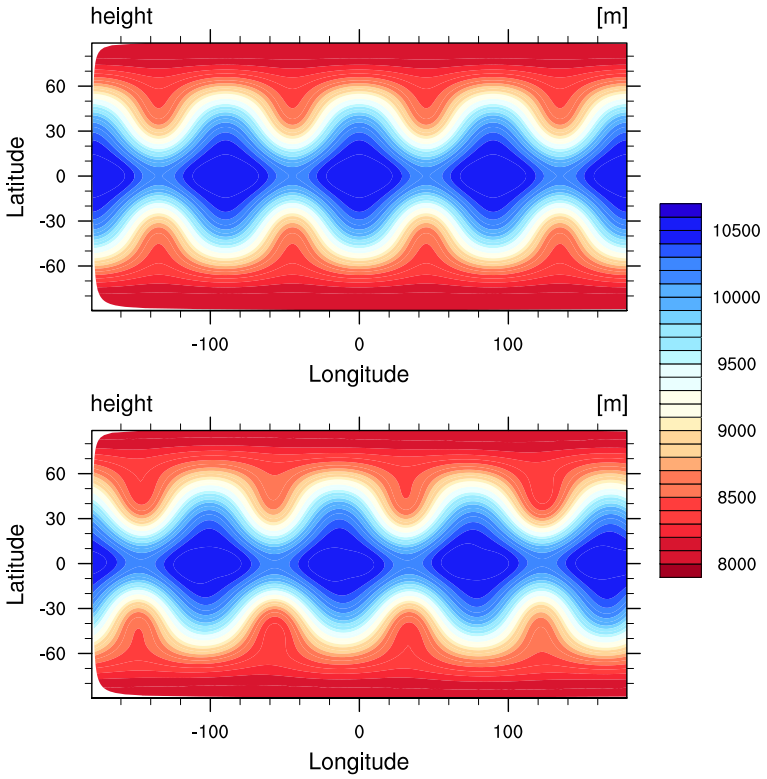

Figure 2.8: Height field $[m]$ of the Rossby-Haurwitz wave test for grid level 4. Top: Initial condition; bottom: After 15 days.

In Figure 2.8, the height of the Rossby-Haurwitz wave is shown in the initial state and after 15 days of integration. Except for the expected movement in zonal direction only small changes in the height field can be observed.

Figure 2.9 shows the behavior of the relative error for mass and its change with spatial resolution and time. We observe that the mass is not conserved in our model runs. The error is caused by the coupling of the 'northern' and 'southern' stereographic

projections. The small gap at the boundary leads to mass inconsistencies. Nevertheless the error is very small and decreases with increasing grid resolution.

The relative error for the global energy is given in Figure 2.10. The initial values for energy and mass are approximately $E^0 = 2.35 \cdot 10^{23} m^5 s^{-2}$ and $M^0 = 4.86 \cdot 10^{18} m^3$, and vary slightly with the resolutions. The error decreases with increasing grid resolution.

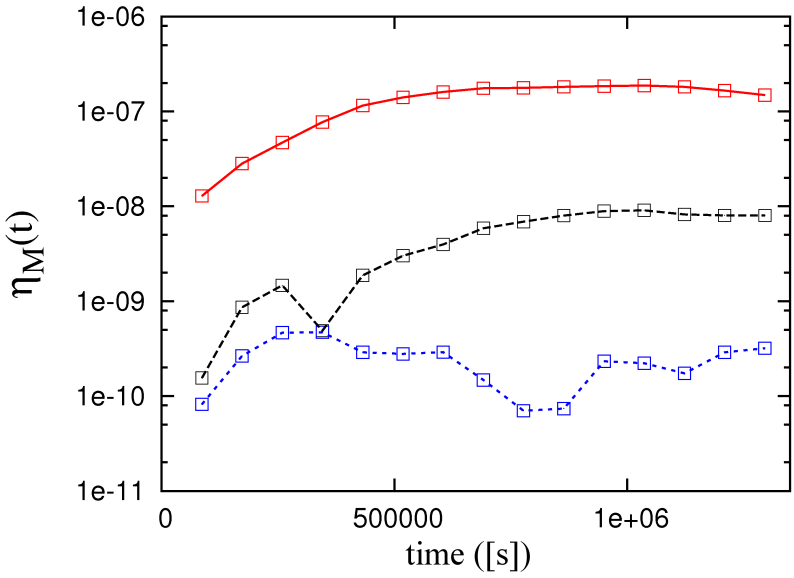

Figure 2.9: Rossby-Haurwitz wave: Time evolution of the relative error for mass. Red continuous line: Grid level 3, black dashed line: Grid level 4, blue dotted line: Grid level 5.

2.3.3 Zonal flow over an isolated mountain

This test is also known from Williamson et al. (1992) (test case 5). The initial conditions have the same shape as the steady state solid body rotation test without inclination in subsection 2.3.1, but the maximum velocity (20 m/s) and the fluid depth (varying between 5960 and 7960 m) are different. A mountain is introduced into the northern hemisphere behind which Rossby waves form and propagate over the globe, including the southern hemisphere.

Figure 2.11 shows the height and the relative vorticity after 15 days. The visible distortion of the vorticity in the direct vicinity of the poles is a postprocessing artifact and occurs since the zonal velocity is not defined at the poles.

Figure 2.12 shows a difference plot between the relative vorticity field after fifteen days obtained with the $P_1^{DG} P_2$ model, compaired to a high-resolution reference run with the NCAR spectral transform shallow-water model (NCAR STSWM, the spectral

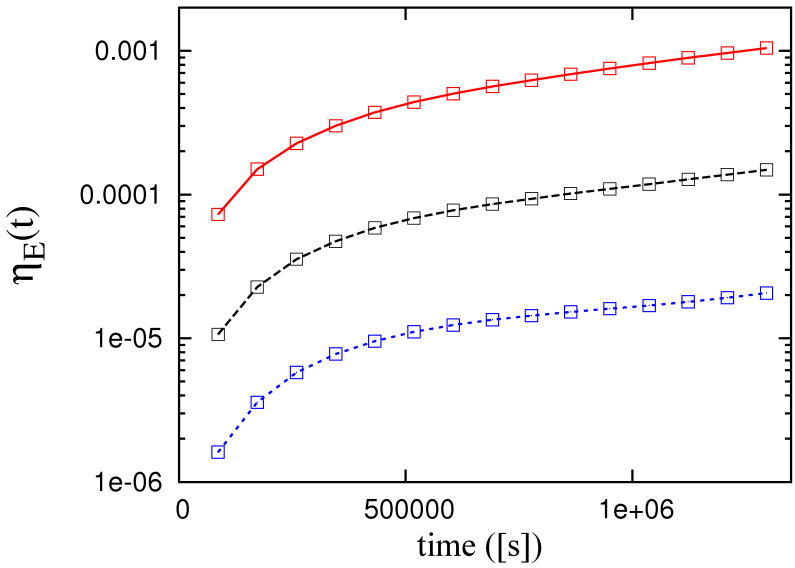

Figure 2.10: Rossby-Haurwitz wave: Time evolution of the relative error for energy. Red continuous line: Grid level 3, black dashed line: Grid level 4, blue dotted line: Grid level 5.

resolution is T426). Figure 8 in Rípodas et al. (2009) shows the same plot compairing the same reference solution to ICONSWM. The ICONSWM simulations were performed on the same grids. As before, the visible distortion of the vorticity in the direct vicinity of the poles is a postprocessing artifact and occurs since the zonal velocity is not defined at the poles. It is furthermore possible that some of the small-scale features are caused by the postprocessing necessary to get comparable data sets.

Figures 2.13 and 2.14 show the behavior of the relative error for mass and energy at different spatial resolution and time. The initial values for energy and mass are approximately $E^0 = 8.0 \cdot 10^{22} m^5 s^{-2}$ and $M^0 = 2.87 \cdot 10^{18} m^3$, and vary slightly with the resolutions. Similarly to the results in subsection 2.3.2, the model errors converge with increasing resolution.

In order to calculate kinetic energy and enstrophy spectra of the Rossby waves created by the flow over the mountain, we proceed as follows. In the first step, the relative vorticity and divergence are calculated as curl and divergence of the velocity on the sphere. In the second step, vorticity and divergence are mapped onto a Gaussian grid. In the third step, the spectral coefficients of vorticity and divergence (ζ_n^m and δ_n^m) are calculated. Steps two and three are performed using the Climate Data Operator tools (CDO, Müller and Schulzweida 2010).

The spectra of the kinetic energy E_{kin}^n and enstrophy Z^n are then given by

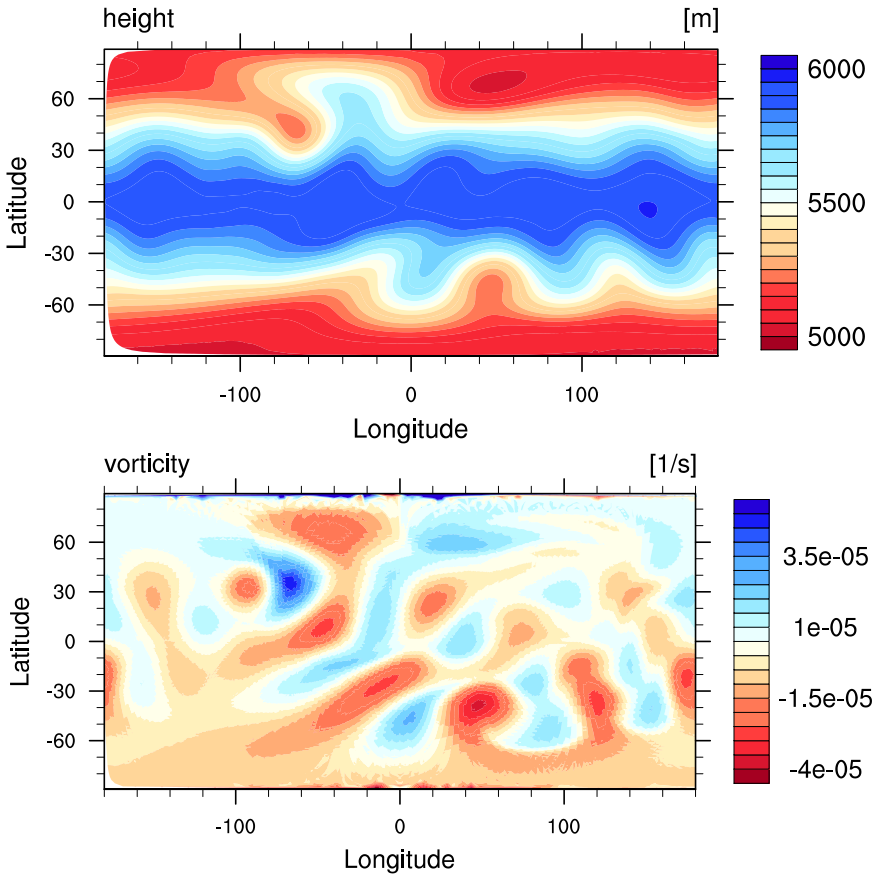

Figure 2.11: Isolated mountain test after fifteen days for grid level 4. Top: Height field $[m]$; bottom: Relative vorticity $[s^{-1}]$.

$$E^n_{\text{kin}} = \frac{a_e^2}{4n\,(n+1)} \left(\left|\zeta_n^0\right|^2 + \left|\delta_n^0\right|^2 + 2\sum_{m=1}^{n} \left|\zeta_n^m\right|^2 + 2\sum_{m=1}^{n} \left|\delta_n^m\right|^2 \right) \tag{2.17}$$

$$Z^n = \frac{1}{4} \left(\left|\zeta_n^0\right|^2 + \sum_{m=1}^{n} 2\left|\zeta_n^m\right|^2 \right),$$

where n is the wavenumber. A derivation of equation (2.17) is shown in Jakob et al. (1993).

The waves behind the mountain are decaying and an energy cascade is initialized. For a two dimensional turbulent cascade we expect the kinetic energy spectra to show a n^{-3}, and the enstrophy spectra to shows a n^{-1} decay with the wavenumber (Salmon 1998). In Figure 2.15, the spectra of the kinetic energy and enstrophy are plotted for grid level 4 after 15, 25, 50, and 75 days. The spectra are smooth and approach the

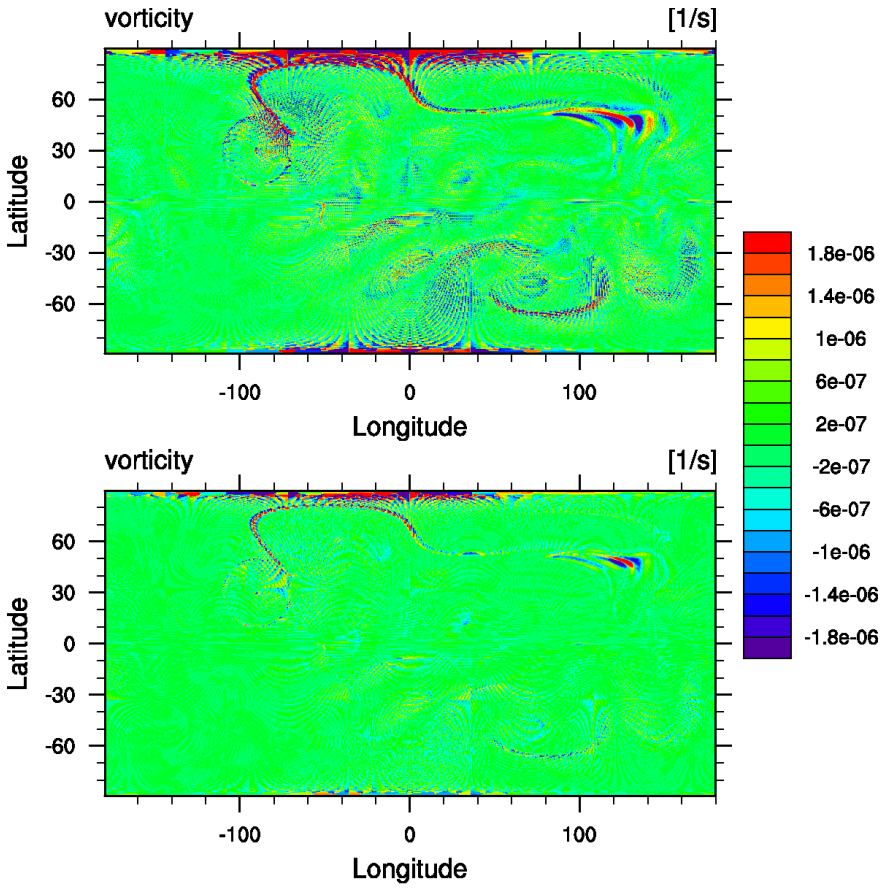

Figure 2.12: Isolated mountain test: Differences between the developed finite element model and a high-resolution NCAR STSWM run for relative vorticity $[s^{-1}]$ after fifteen days. Top: Grid level 5; bottom: Grid level 6.

expected slopes when time is increasing. The energy spectra after 15 days are similar to high-resolution runs of other models such as the ICON shallow-water or the NCAR STSWM model (Rípodas et al. 2009). No additional diffusion was used in our model runs ($\nu = 0$).

2.3.4 Perturbed jet stream

A detailed prescription of the perturbed jet stream test case can be found in Galewsky et al. (2004). The setting represents a barotropically unstable mid latitude jet balanced by the height field. A small height perturbation is added to the initial state to destabilize the setup. After several days of integration the perturbation leads to a turbulent decay of the solution. In the original paper, the test case is simulated using a spectral model that performs well on the test. As the jet is fairly strong and localized (between

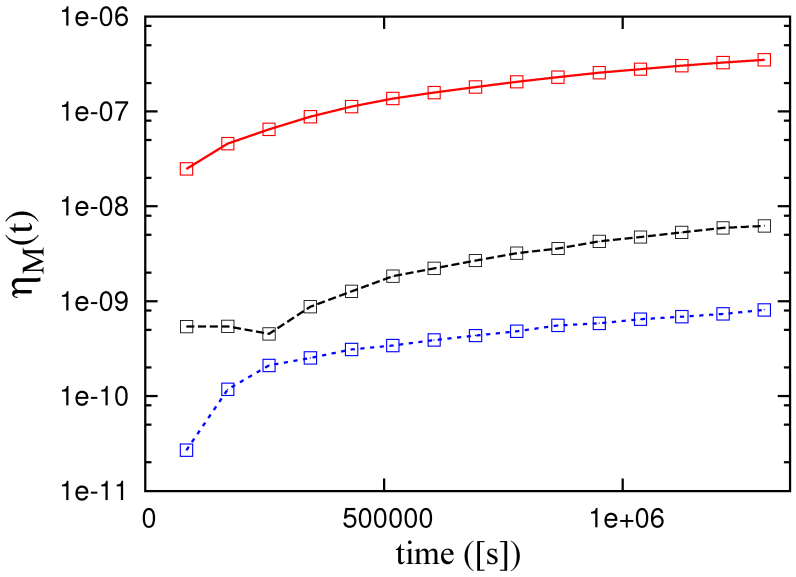

Figure 2.13: Isolated mountain test: Time evolution of the relative error for mass. Red continuous line: Grid level 3, black dashed line: Grid level 4, blue dotted line: Grid level 5.

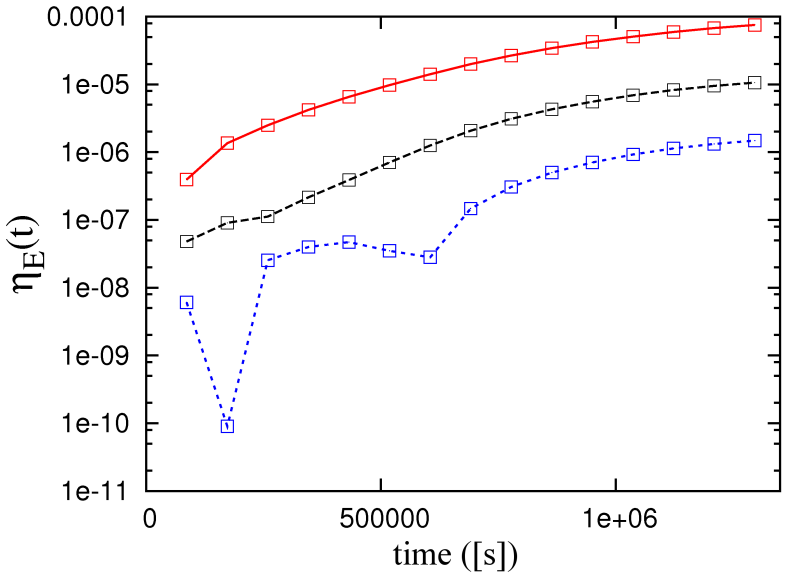

Figure 2.14: Isolated mountain test: Time evolution of the relative error for energy. Red continuous line: Grid level 3, black dashed line: Grid level 4, blue dotted line: Grid level 5.

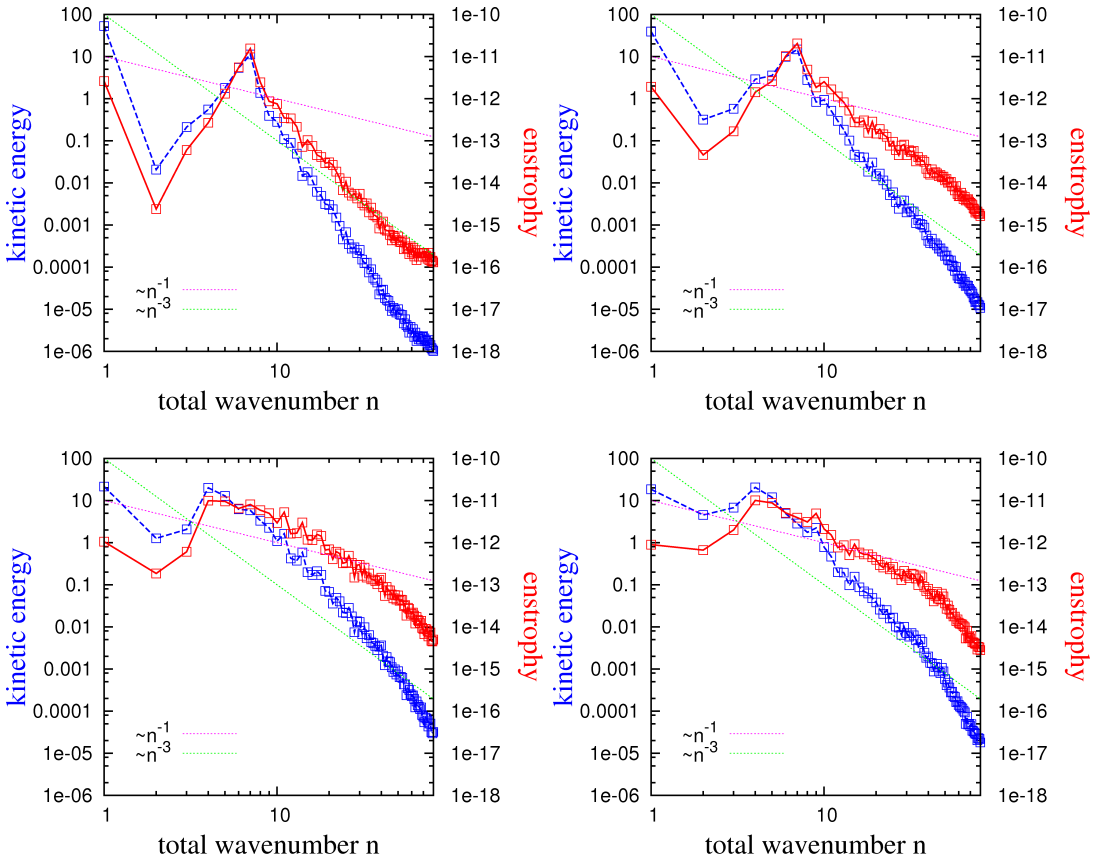

Figure 2.15: Isolated mountain test: Kinetic energy spectra (blue dashed line) and enstrophy spectra (red continuous line) for grid level 4. Upper left: After 15 days; Upper right: After 25 days; Lower left: After 50 days; Lower right: After 75 days.

25 and 65 degrees north) the test is challenging for gridpoint models, particularly if a low-order field representation is used. The smooth initial condition must be represented in an appropriate way. Small perturbations that occur due to model errors are sufficient to destabilize the initial solution – unless the grid resolution is high enough (Shin et al. 2010).

In view of this, the $P_1^{DG}P_2$ model requires a rather high grid resolution to produce model runs where the jet remains stable for more than six days. In Figure 2.16, the vorticity field of the unperturbed test is shown at the initial time and after six days of integration on grid level 6. Even the highest resolution used for simulations in this paper displays the wave 5 pattern which is caused by the broken rotational symmetry of the icosahedral grid.

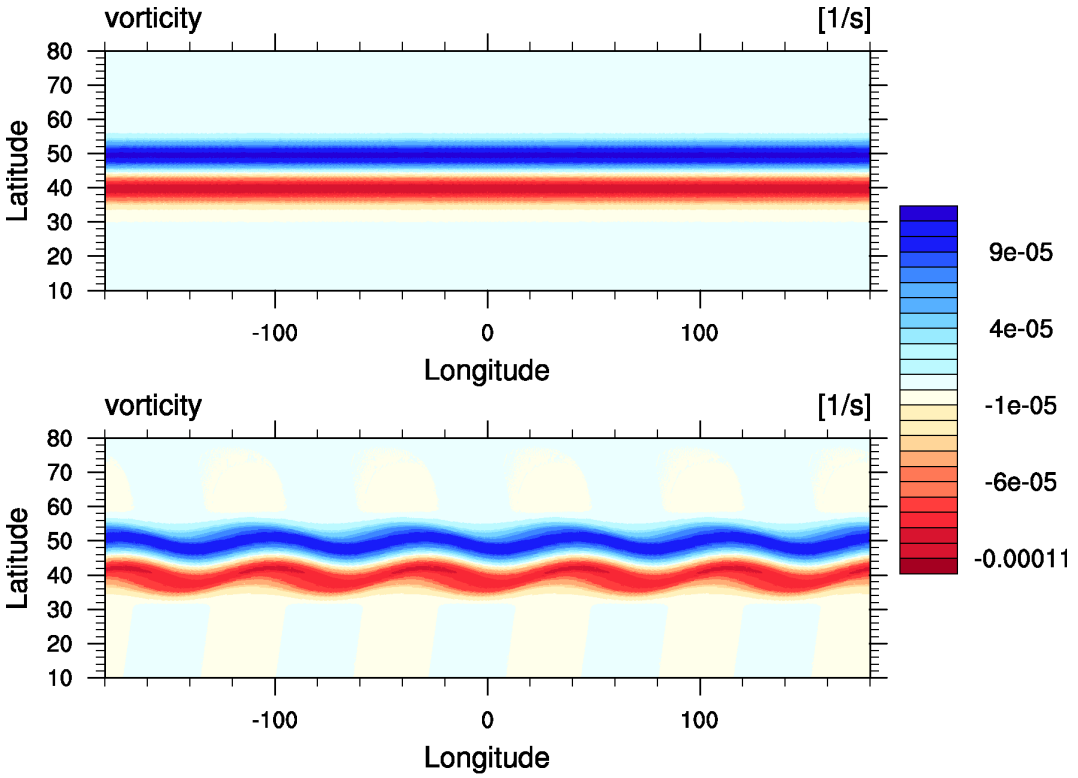

Figure 2.16: Vorticity field $[s^{-1}]$ of the Galewsky test without initial perturbations for grid level 6. Top: Initial state; bottom: After six days of integration.

Nevertheless, the artifacts produced by the model are much smaller than the perturbations introduced in the initial condition for the perturbed jet. Figure 2.17 shows the vorticity field for the perturbed case after four, five, and six days of integration for grid level 6. The numerical solutions produced by our model match very well those from the literature (Galewsky et al. 2004; Läuter et al. 2008; Ullrich et al. 2010).

2.3.5 Munk gyre test case

We continue the numerical study of our finite element model with an ocean test case. We consider an ocean gyre in the northern hemisphere that is forced by the wind and is rotating in clockwise direction. The test should verify the correct implementation of boundary conditions and diffusion. Due to the change of the Coriolis parameter in the meridional direction, the gyre is intensified towards the western boundary, and a western boundary current develops (Pedlosky 1996). The test is performed for the viscous case ($\nu = 50000\frac{m}{s^2}$) with free-slip and no-slip boundary conditions. Viscosity is chosen in such a way that the Munk layer at the western boundary is resolved by at least two gridcells (Griffies 2004).

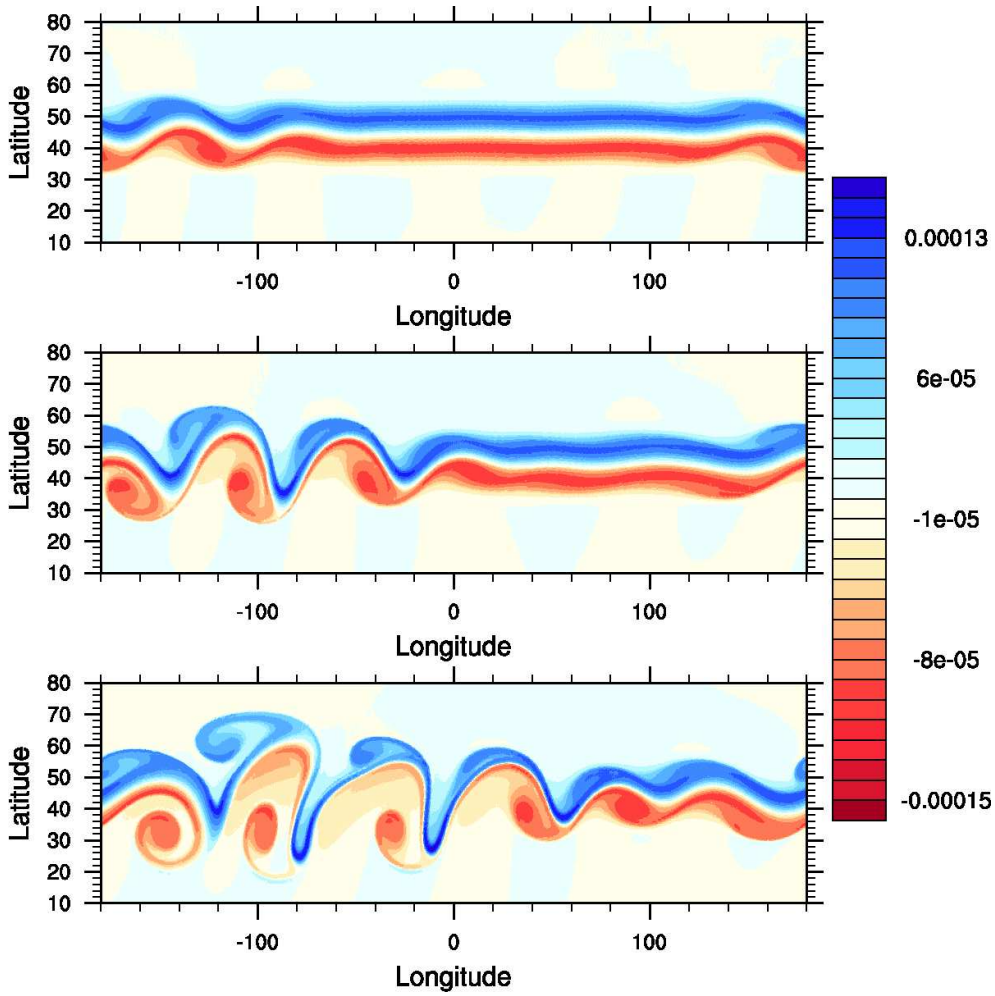

Figure 2.17: Vorticity field $[s^{-1}]$ of the Galewsky test with initial perturbations for grid level 6. After four, five, and six days (from top to bottom).

The domain is nearly rectangular on a longitude/latitude projection and extends from the equator up to about 60° north and over about 72° in zonal directions. Wind forcing and bottom friction are introduced to the differential equation using the following terms

$$\boldsymbol{\tau} = \frac{\boldsymbol{\tau}^s}{H} - \gamma \mathbf{u},$$

where $\boldsymbol{\tau}^s$ is the surface wind stress, and γ is the bottom friction coefficient set to $10^{-6} s^{-1}$.

While the meridional wind stress is zero, the zonal wind stress is set to

$$\tau_\lambda^s = -7 \cdot 10^{-3} \cdot \cos\left(\frac{\pi\phi}{60°}\right) \frac{m^2}{s^2}.$$

The model runs are performed on a grid that consists of 7680 cells that are distributed nearly uniformly. The height field is initialized with a constant water depth of $5000m$; the velocity is set to zero.

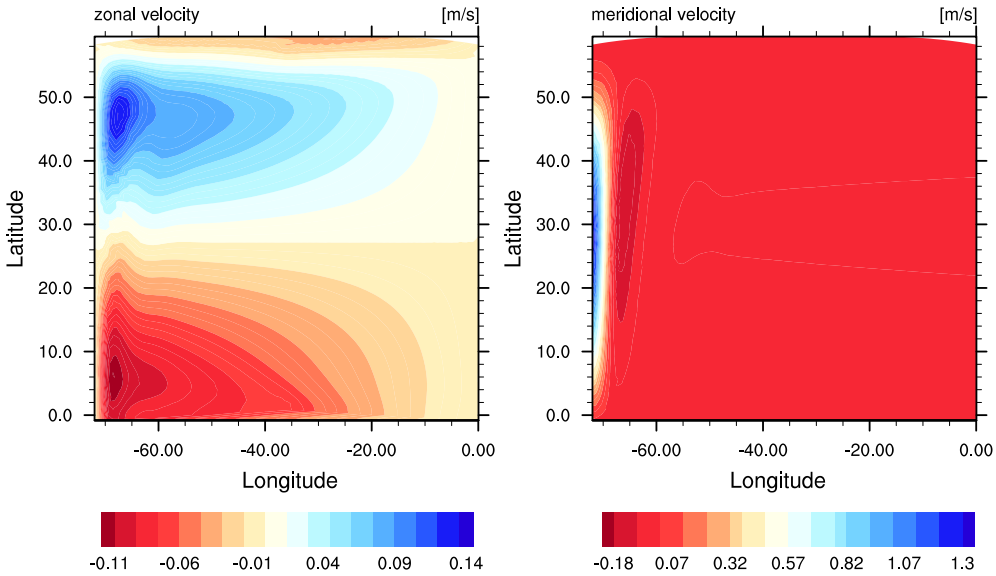

Figure 2.18: Munk gyre test with advection and free-slip boundary conditions. Left: Zonal velocity $[\frac{m}{s}]$; right: Meridional velocity $[\frac{m}{s}]$.

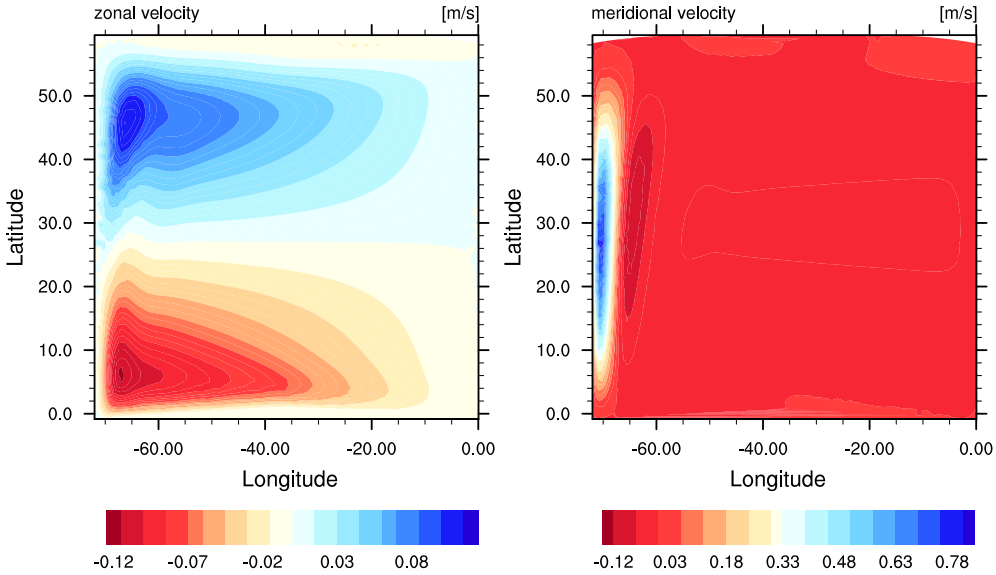

Figure 2.19: Munk gyre test with advection and no-slip boundary condition. Left: Zonal velocity $[\frac{m}{s}]$; right: Meridional velocity $[\frac{m}{s}]$.

Figures 2.18 and 2.19 show the physical fields after 250 days of integration. The model appears to be in equilibrium. The model runs are stable and the boundary conditions are properly satisfied. For both tests, the Munk layer is represented smoothly and shows the expected width.

Tests performed with the inviscid equations are stable as well and show a reasonable representation of the no-flow boundary conditions. For zero viscosity, the Munk layer is intensified at the edge of the western boundary. It cannot be resolved properly by the model, just as expected.

2.4 Conclusions

We investigate the potential applicability of the $P_1^{DG}P_2$ finite element pair in atmosphere and ocean modeling. We present a stable $P_1^{DG}P_2$ discretization for the viscous and inviscid shallow-water equations on the sphere. We do not observe any spurious modes that necessitate additional diffusion or stabilization schemes.

Regarding the convergence properties and kinetic energy spectra, our discretization shows the expected behavior. A comparison to the ICON shallow-water model shows very promissing results. For the conservation properties of our $P_1^{DG}P_2$-discretization, we note an error in global mass conservation if two projections are coupled together. While this can easily be avoided in ocean applications it constitutes a shortcoming for atmosphere applications, at least for long integration times. For atmospheric models, it might be advisable to introduce the spherical geometry by an approach different from the stereographic projection. To this end, the method presented in Bernard et al. (2009) appears qualified. It seems to be more expensive than the stereographic projection approach, but it should enable a mass conservative $P_1^{DG}P_2$ model for atmospheric applications, and was successfully applied to a discontinuous Galerkin finite element model.

Based on the results from this paper, we can conclude that the considered finite element shows very promising properties for use in dynamical cores of global weather or climate models and encourages further investigation of this type of element for three-dimensional atmosphere and ocean models.

Chapter 3

Variable resolution modeling in atmosphere and ocean is less painful than expected

We consider the use of static grid refinement in a global, low-order finite element model. Through the study of the transition of waves between coarse and fine parts of a grid, the robustness of the model to grid refinement, and the influence of grid refinement on the representation of geostrophic balance and turbulent cascades, we investigate possible sources of errors for applications of grid refinement in ocean and atmosphere modeling. Furthermore, we investigate improvements that are possible through grid refinement, evaluating the representation of topography, local wave patterns, and western boundary currents.

We arrange a set of six test cases on planar and spherical domains to investigate the use of static, local grid refinement. Simulations are performed on grids with abrupt changes in grid spacing, and we vary the ratio of the resolution in the coarse and the fine part of the grid, and the shape of the transition zone. The results are compared to model runs on uniform grids, and evaluated considering the spectra of kinetic energy and enstrophy, energy conservation, and error norms.

As expected, the reflection and scattering of waves is strong for small-scale flow patterns. Nonetheless, the results show that improvements possible with a deliberated use of static, local grid refinement justify the risk of errors, since large-scale flow patterns, turbulent cascades, and the representation of the geostrophic balance are not disturbed.

3.1 Introduction

Despite the current trend towards cloud and eddy-resolving simulations, the affordable resolution in atmosphere and ocean modeling is still far from sufficient. This motivates the investigation of grid refinement as a tool to gain efficiency. In global ocean or atmosphere modeling local grid refinement could be used to increase the resolution in a specific region of interest – such as a single country or continent, arctic or tropical regions. Local grid refinement could also be used to improve the representation of important local features that have a large impact on the whole simulation – such as boundary currents, sea overflows, islands, and deep water formations in an ocean

model, and mountains, tropical cyclones, and convection areas in an atmosphere model. The purpose of this paper is to study the influence of grids of variable resolution to fundamental features of geophysical modeling, such as wave propagation, the representation of turbulent cascades, or geostrophic adjustment. We focus on the quality of the solution on statically refined grids. For this purpose we propose several test cases that capture important dynamical aspects. We do not focus on the computational efficiency.

Grid refinement is used successfully in Computational Fluid Dynamics for numerous applications, such as for simulations of flow around airfoils or cars, mostly in models based on finite element and finite volume discretization methods. These models appear to be very robust for the use on refined grids. Currently, there are attempts to build up global ocean or atmosphere models that would allow the use of local grid refinement (Giraldo et al. 2002; Giraldo 2006; Nair et al. 2005; Läuter et al. 2008), and there are promising approaches to modeling of atmosphere and ocean on the global scale, using unstructured grids in which the lattice spacing can vary significantly within the domain (Piggott et al. 2008; Ringler et al. 2011).

When refined grids are used in numerical modeling, the user needs to be aware of the reflection and scattering of waves at the transition between coarse and fine parts of the grids. It is well known from literature that small-scale waves with a wave length close to the grid spacing can be affected strongly when simulations are performed on refined grids, while large-scale features typically appear rather unaffected. While classical papers on errors caused by grid refinement mostly consider applications in Computational Fluid Dynamics (see for instance Trefethen 1982; Vichnevetsky 1987), recent publications also focus on refinement errors in possible dynamical cores for geophysical applications (Ullrich and Jablonowski 2011; Long and Thuburn 2011). Dispersion relations and group velocities can be calculated for the considered discretization methods and linear equations; this allows the prediction and detailed analysis of wave properties at the transition zones between coarse and fine grids. Results indicate that, as long as the wave length is of the same order of magnitude as the grid spacing, severe reflection and scattering occur for almost every discretization scheme.

In this paper, we investigate the use of grid refinement in a shallow-water model based on a new hybrid finite element. The shallow-water system provides a meaningful first test ground for geophysical applications. The used numerical model is based on a low-order finite element method that is a potential candidate to form the dynamical core of future weather or climate models. The new approach combines a continuous second order representation for the height field with a discontinuous first order representation for the velocity field on a triangular grid – the $P_1^{DG}P_2$ finite element (Cotter et al. 2009a, Chapter 2). The element fulfills the Ladyzhenskaya-Babuska-Brezzi-condition, which is a necessary condition for convergence in finite element modeling, and is able to represent the geostrophic balance at the same time (Cotter et al. 2009a,b). This is remarkable for a low-order finite element and necessary to avoid spurious modes in

geophysical applications (Le Roux et al. 1998). In principle, the considered element allows h- and r-refinement (either new grid points are introduced into the domain, or given grid points are moved towards regions of specific interest), and has already been used on unstructured and refined grids (Comblen et al. 2010).

An analytical investigation of the error caused by grid refinement appears to be hardly possible for geophysical models in two or three dimensions, based on nonlinear, viscous equations, and discretized on unstructured grids. Still, it is crucially important to ensure that the wave propagation and the turbulent cascade is not strongly affected by grid refinement, before using refined grids for geophysical applications. Geostrophic balance and conservation properties need to be maintained on the refined grids, as well.

To the authors knowledge, a detailed investigation of errors and improvements possible with the use of grid refinement has not been done for non-linear equations and geophysical applications; neither for the specific $P_1^{DG}P_2$ low-order finite element, nor for finite element methods in general. We consider the following research questions, to evaluate grid refinement in a global $P_1^{DG}P_2$ finite element model:

1. Up to which wave length – compared to the grid spacing – is grid refinement leading to spurious behavior? Is grid refinement influencing large-scale flow features?
2. What is the influence of the structure of the transition zone between coarse and fine parts of the grid? How does the error behave when the change of resolution is increased?
3. What are the limits of stability for model simulations on refined grids?
4. Is the ability to represent the geostrophic balance influenced by grid refinement for the considered finite element setup?
5. What is the influence of grid refinement on the turbulent cascade and energy conservation for the considered finite element setup?
6. In which applications can grid refinement improve the simulations of the shallow-water model?
7. What are appropriate diagnostics to assess the error caused by local grid refinement?

To this end we simulate wave packets with various internal wave lengths, a Gaussian hill in geostrophic balance, two-dimensional turbulent cascades, and typical test cases for global shallow-water models, namely the decay of a zonal flow over an isolated mountain, a perturbed jet stream, and a wind driven ocean gyre. The model runs are evaluated with kinetic energy and enstrophy spectra, L^1- and L^2- error norms, and energy conservation.

We perform simulations on refined grids, where refinement is realized by introducing new grid points to the original grid (h-refinement). It is known from the literature that a change in resolution has a more severe influence on low-order than on high-order finite element methods (Medina and Rosales 1987), and that visible errors that are caused by grid refinement are mostly apparent if abrupt changes of the grid spacing are considered. We solely investigate abrupt changes where grid resolution is increased by a factor of two, four, or eight within one grid spacing of the unrefined grid. Since we investigate a low-order finite element model, we consider our setup as a kind of extreme case scenario for general finite element models.

In section two, we give a brief overview about the model setup. In section three, we present numerical results. In section four, we draw the conclusions.

3.2 Model setup

This section will give a brief introduction to the functionality of the used model, including the shallow-water equations, the discretization in space and time, and the mechanism of grid refinement. A detailed description of the model setup can be found in Chapter 2.

3.2.1 The viscous shallow-water equations

We consider the viscous shallow-water equations in non-conservative form

$$\partial_t \mathbf{u} + \mathbf{u} \cdot (\nabla \mathbf{u}) + f\mathbf{k} \times \mathbf{u} + g\nabla h - \frac{1}{H}\nabla \cdot (H\nu\,(\nabla \mathbf{u})) = \boldsymbol{\tau}, \tag{3.1}$$

$$\partial_t h + \nabla \cdot (H\mathbf{u}) = 0, \tag{3.2}$$

where $\mathbf{u}$ is the two dimensional velocity vector, f is the Coriolis parameter, $\mathbf{k}$ is the vertical unit vector, g is the gravitational acceleration, ν is the eddy viscosity, $\boldsymbol{\tau}$ is a forcing term (for example bottom friction or wind stress in ocean applications), h is the surface elevation, and H is the height of the fluid column given by $H = h - h_b$, where h_b is the bathymetry. The prognostic variables are the surface elevation and the velocity.

3.2.2 Discretization

Following the typical finite element approach, we expand the physical fields into sets of basis functions N_i and M_i

$$\mathbf{u} = \sum_{i=1}^{N_u} \mathbf{u}_i N_i \qquad \text{and} \qquad h = \sum_{i=1}^{N_h} h_i M_i.$$

We use a $P_1^{DG}P_2$ finite element to discretize the equations. This means that we employ discontinuous linear Lagrange polynomials for the representation of the velocity field (N_i), and globally continuous quadratic Lagrange polynomials for the representation of the height field (M_i). Each triangular cell has three degrees of freedom for each component of velocity located at the vertices of the cells and six degrees of freedom for the height field located at the vertices and edges. While the degrees of freedom of the height field are shared with the surrounding cells, the degrees of freedom of the velocity field belong to a specific cell, which leads to a discontinuous representation.

To expand the physical fields into sets of basis functions, the triangles in physical space need to be mapped onto a reference triangle on which the basis functions are defined. On the sphere, the geometry of the physical triangles is given by trigonometric functions and cannot be mapped exactly onto a reference triangle, which is typically defined on the plane. To this end a stereographic projection is introduced into the model. The projection is mapping the sphere onto a planar domain below the sphere. The physical triangles can be defined to be planar triangles on the stereographic domain, this allows an exact mapping to the reference triangle.

Time integration is performed by an explicit three level Adams-Bashforth method. The equation

$$\partial_t \boldsymbol{\psi} = R(\boldsymbol{\psi}),$$

where R denotes the right hand side of the system, and $\boldsymbol{\psi}$ is the vector of prognostic variables, is discretized in time by

$$\boldsymbol{\psi}^{n+1} = \boldsymbol{\psi}^n + \Delta t \left(\frac{23}{12} R(\boldsymbol{\psi}^n) - \frac{4}{3} R(\boldsymbol{\psi}^{n-1}) + \frac{5}{12} R(\boldsymbol{\psi}^{n-2}) \right),$$

where $\boldsymbol{\psi}^i$ is the vector of state variables at the i-th time step.

3.2.3 Grids and grid refinement

In principle the model is applicable to each kind of triangular grid. In this publication, we use two types of standard grids on which refinement is performed. On the one hand, we use structured triangular grids that provide a uniform coverage of the plane. The grids are developed from rectangular grids by bisecting each rectangular into two triangles. On the other hand, we use icosahedral geodesic grids that provide a quasi-uniform coverage of the sphere (Baumgardner and Frederickson 1985).

In the h-refinement procedure used to refine the (quasi-) uniform standard grids, an area of specific interest is specified where the original triangles are split into four new triangles (sketched in Figure 3.1). Changes in the grid spacing are always performed in an abrupt way, which means that the grid spacing is changing by a factor of two, four, or eight within one grid spacing of the coarse grid. In the standard procedure the

triangles in the transition zone between coarse and fine parts of a grid are split into two new triangles, as shown in Figure 3.1. For global applications, the new vertices are projected onto the sphere.

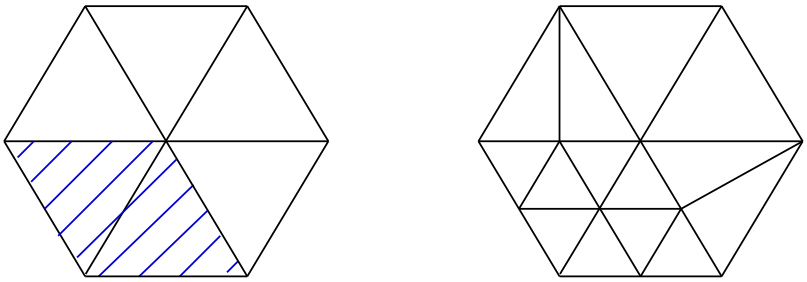

Figure 3.1: Sketch of the refinement procedure. An area of interest is specified in the original grid (left), the triangles are divided into four new triangles, and a transition zone is introduced (right).

3.3 Numerical results

In this section we perform six test cases, in order to tackle the research questions stated in the introduction.

In the first three tests, we investigate idealized test setups to study the error and effect caused by grid refinement in the considered shallow-water setup. In the first test (subsection 3.3.1), we investigate wave packets that cross the interface between coarse and fine, and fine and coarse parts of a grid. The test allows a detailed analysis of the error caused for waves with variable wave lengths. In the second test (subsection 3.3.2), we investigate a Gaussian water hill in geostrophic balance, for the linear shallow-water equations with Coriolis force. The test evaluates the effect of grid refinement to the representation of geostrophic balance. In the third test (subsection 3.3.3), we consider randomly initialized physical fields, to investigate the effect of grid refinement on turbulent decays.

In the last three tests, we consider applications in which grid refinement can possibly improve the simulations of the shallow-water model. In the fourth test (subsection 3.3.4), we simulate the flow over an isolated mountain to consider possible improvements for the representation of topography. In the fifth test (subsection 3.3.5), we consider the decay of a perturbed jet stream to investigate possible improvements for the representation of local wave patterns. In the sixth test (subsection 3.3.6), we simulate wind driven ocean gyres to evaluate possible improvements for the representation of western boundary currents. All subsections close with a short summary of the results.

Parameter	Value
u_a	$2.0\frac{m}{s}$
u_g	$250.0\frac{m}{s}$
σ^2	$0.006\ L_x^2$
L_x	$10^7 m$
L_y	$1.6 \cdot 10^6 m$
x_0	$0.25\ L_x$

Table 3.1: Initial conditions for the wave packets affected by grid refinement test.

3.3.1 Wave packets affected by grid refinement

In this subsection we consider the transition of wave packets between coarse and fine areas of a grid. The test shall investigate the influence of refinement on waves with variable wave length, the influence of the structure of the transition zone, and the influence of the ratio of resolution in the coarse and the fine part of a grid. To this end, we evaluate four different wave lengths of the internal wave in the wave packet, perform simulations on grids with an abrupt change in resolution by a factor of two, four, and eight, and consider two different types of transition zones and two different angles the incoming waves form with the change in resolution. The model results are evaluated with regard to the error in energy conservation, and the change of the spectra of kinetic energy and enstrophy.

The wave packets are initialized as follows

$$u = u_a \exp\left(-\frac{(x-x_0)^2}{2\,\sigma^2}\right) \sin\left(\frac{2\pi n\,(x-x_0)}{L_x}\right), \qquad v = 0,$$

$$\text{and} \qquad h = \frac{u_g^2}{g} + \frac{u_a \cdot u_g}{g} \exp\left(-\frac{(x-x_0)^2}{2\,\sigma^2}\right) \sin\left(\frac{2\pi n\,(x-x_0)}{L_x}\right),$$

where u_a is the maximal absolute value of the zonal velocity, u_g is the group velocity of the wave packet, σ is the standard deviation that adjusts the width of the packet, x_0 is the center of the packet, and n is the wave number which indicates the ratio how often the wave length of the inner frequency of the packet fits into the length of the domain L_x. Simulations are performed on a plane with periodic boundary conditions.

The initial values used for our simulations are given in Table 3.1. For the given standard deviation, the envelop of the wave packet, which is located in the left half of the domain, reduces to less than one percent of its peak value at the left boundary, and in the middle of the domain. We simulate the inviscid non-linear shallow-water equations without Coriolis force (equations (3.1) and (3.2) with $f = \nu = 0$).

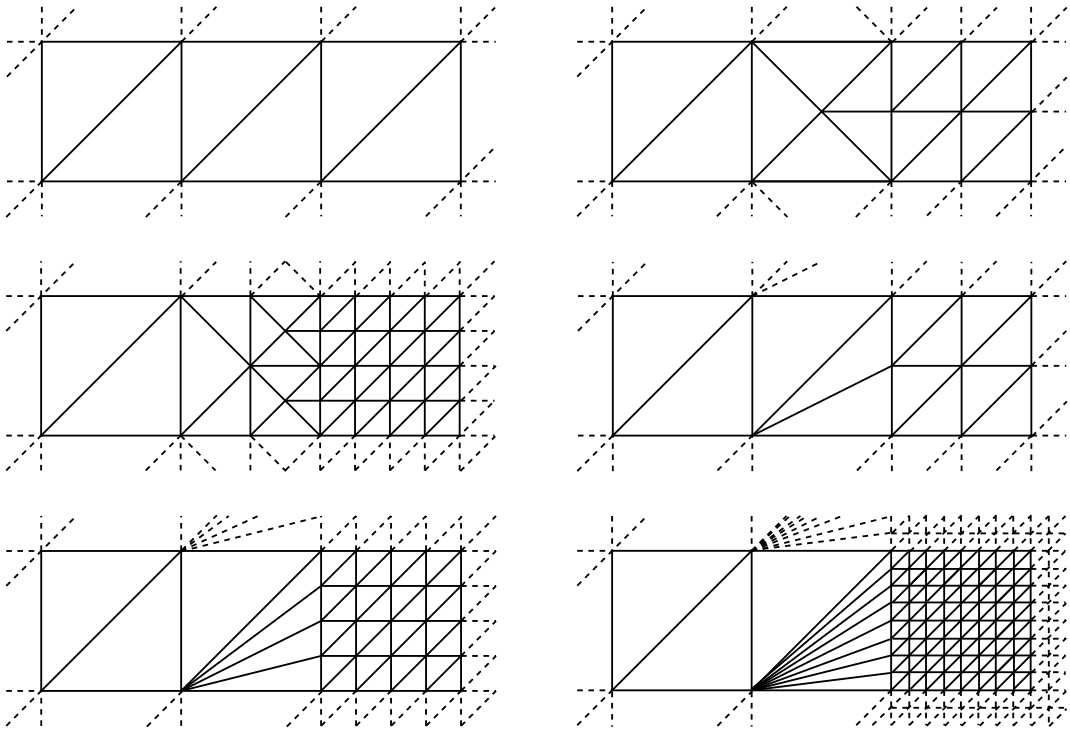

Figure 3.2: Transition zone between the left and the right hand side of the grids. Upper left: H_0; Upper right: $H_0T_1R_1$; Middle left: $H_0T_1R_2$; Middle right: $H_0T_2R_1$; Lower left: $H_0T_2R_2$; Lower right: $H_0T_2R_3$.

We use a grid that consists of 50x8 squares, each of them divided into two triangles, as the unrefined starting point for grid refinement (H_0). We refine either the left or the right half of the domain, and increase the resolution by a factor of two, four, or eight. We use two different types of transition zones between the refined and unrefined areas. Both of them lead to an abrupt change in resolution. The transition zones of the grids are sketched in Figure 3.2. In the first type the triangles at the transition zone do not have steep angles ($H_0T_1R_1$, $H_0T_1R_2$). In the second type, the triangles at the transition show steep angles ($H_0T_2R_1$, $H_0T_2R_2$, $H_0T_2R_3$; there are angles with less than 6 degrees). Additionally to the grids in Figure 3.2 we use grids in which the left half of the domain is refined ($H_0T_1L_1$, $H_0T_1L_2$, $H_0T_2L_1$, $H_0T_2L_2$, $H_0T_2L_3$), and uniformly refined grids in which the whole domain offers doubled or four times the resolution of the coarse grid (H_1,H_2). In the nomenclature of the grids the subscript of H indicates the coarsest resolution in the domain compared to the initial grid H_0, the subscript of T indicates the type of the transition zone, and L or R indicate whether the left or the right side was refinement by the number of levels indicated by the subscript.

At least two grid points are necessary to resolve a given wave length in a grid point

finite difference model. The number of cells by which one wave length of the internal wave is resolved on the coarse grid H_0 is given by $50/n$. For our simulations, we consider two wave packets where the internal wave should be resolved properly ($n = 5$, and $n = 10$), and two wave packets where the coarse resolution is very close to, or below the possible minimum to resolve the wave packet ($n = 20$, and $n = 30$).

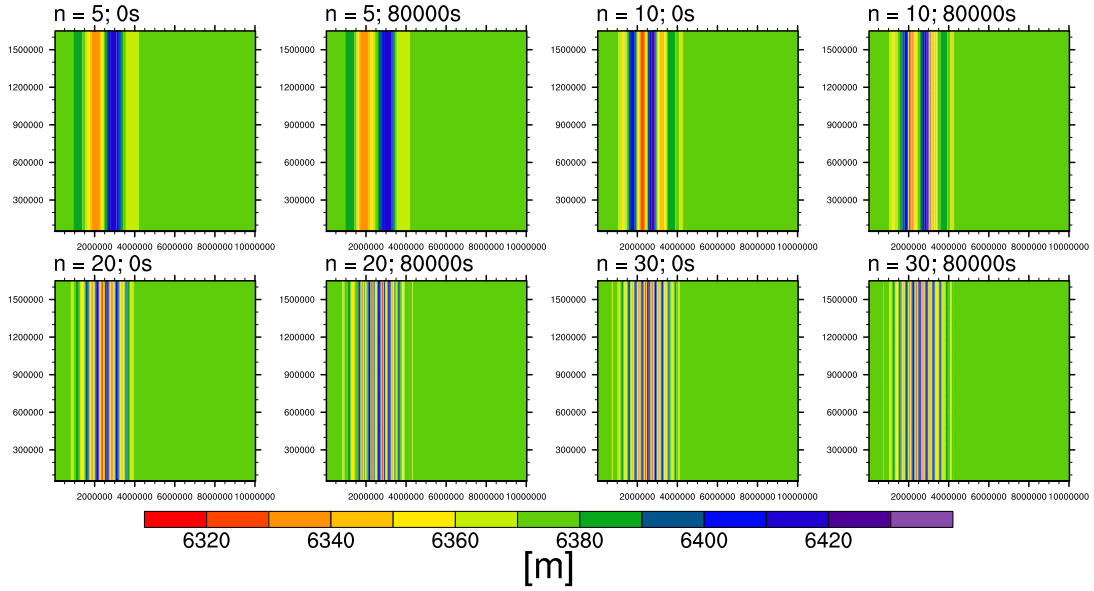

Figure 3.3: Height field at initialization (left plot of a couple) and after 80000 seconds (right plot of a couple) for $n = 5$, $n = 10$, $n = 20$, and $n = 30$ (from top left to bottom right), for simulations on the finest uniform grid (H_2).

Figure 3.3 shows the height field of the reference runs on the finest uniform grid (H_2) at initialization and after 80000s seconds. The height field has reached the initial position again for the second time. Changes in the shape are hardly visible. Figure 3.4 shows the spectra of kinetic energy for the same simulations. The procedure to calculate the spectral coefficients is described in the Appendix 3.A. All spectral coefficients E_{ij} are zero for j different from zero, since the physical fields only vary in the x and not in the y direction. The kinetic energy spectrum of the initial wave packet has the form of a Gaussian distribution centered around n. The initial Gaussian distribution is slowly getting weaker with increasing time, and additional Gaussian distributions form at multiples of the wave number n. We assume that the wave packets are sufficiently resolved on the H_2 grid, and advection induces weak scale interactions. The changes increase for increasing n.

Figure 3.5 shows the height field after 20000 seconds for simulations on the $H_0T_2L_3$ and the $H_0T_2R_3$ grid. That specific time step is interesting because the wave packet has crossed the transition zone once, and traveled for the same time on each side of the

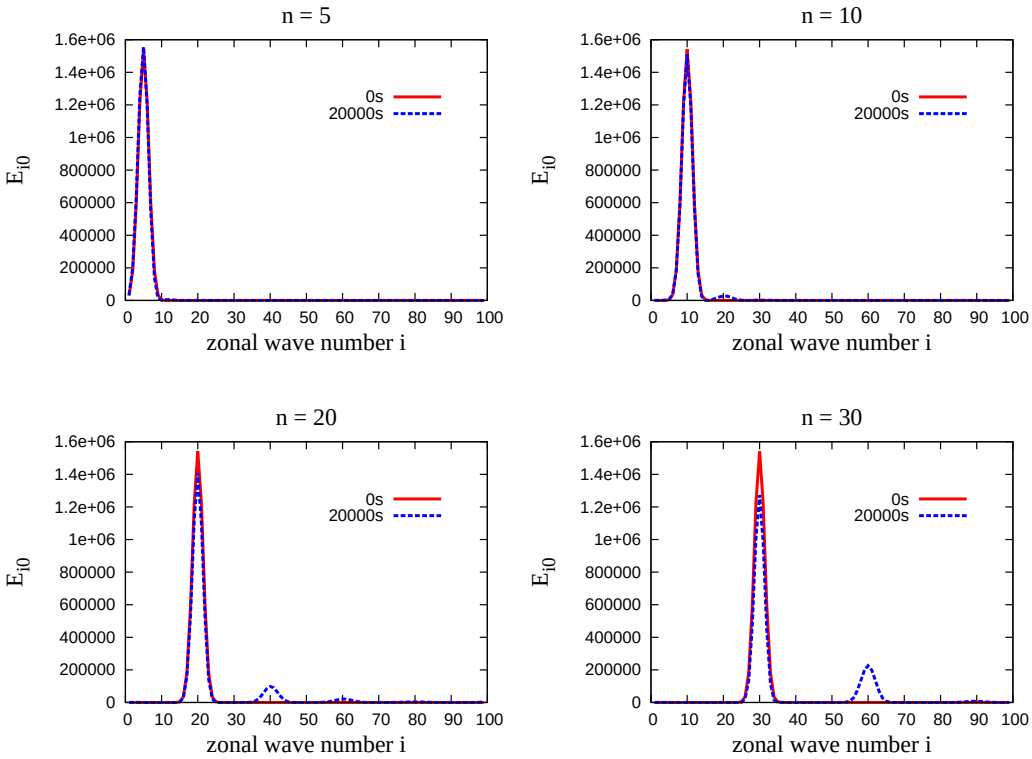

Figure 3.4: Kinetic energy spectra calculated at initialization and after 20000 seconds for $n = 5$, $n = 10$, $n = 20$, and $n = 30$ (from top left to bottom right) for simulations on the finest uniform grid (H_2). The spectra are calculated by evaluating all of the 200x64 vertices of the grid, for the discrete Fourier transformations.

grid. For the sufficiently resolved waves with $n = 5$ and $n = 10$ the differences between the grids are hardly visible. For higher values of n, differences become clearly visible. Plots for the model runs on grids with lower refinement level (not shown here) look very similar to the runs on the $H_0T_2L_3$ and the $H_0T_2R_3$ grid.

A consideration of the spectra of kinetic energy and enstrophy could give a better impression of the errors caused by grid refinement. Unfortunately, a calculation of the discrete Fourier transformation of a physical field, which is needed to calculate the kinetic energy and enstrophy spectra (see Appendix 3.A), is – to our best knowledge – only possible for equidistant grids. A grid in which local refinement has been performed is not equidistant by definition. A chance to get an approximation of the spectra of the physical fields is to calculate discrete Fourier transformations using only the equidistant grid points of the initial, unrefined grids. The obtained spectra are not equal to the 'real' energy spectra of the physical fields, but they offer a good approximation. The major shortcoming of this procedure is that the obtained spectra cover only wave lengths

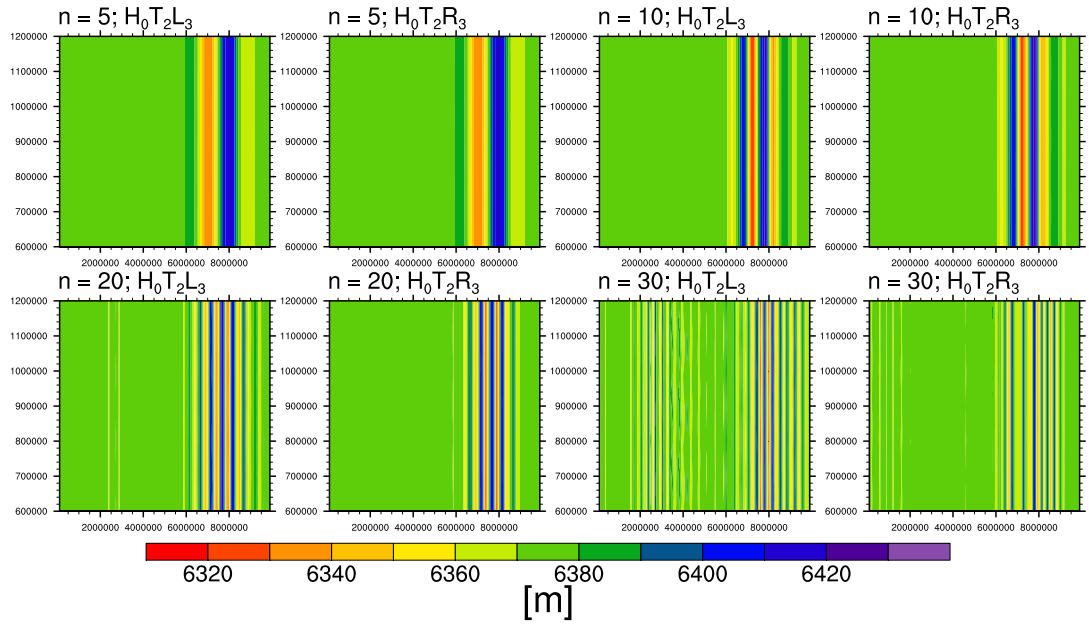

Figure 3.5: Height field after 20000s on the $H_0T_2L_3$ (left plot of a couple) and the $H_0T_2R_3$ grid (right plot of a couple), for $n = 5$, $n = 10$, $n = 20$, and $n = 30$ (from top left to bottom right).

down to the doubled grid spacing of the initial, unrefined grid. Small-scale structures that are resolved only in the refined areas are not represented in the calculated spectra.

Figure 3.6 shows the approximated kinetic energy spectra obtained by the method described above after 20000 seconds for different values of the wavenumber n on the different grids. We note that changes of the total level of the kinetic energy spectra do not indicate a change of total energy within the simulation. Energy can be transferred into potential energy or higher wave numbers that are not covered by the approximated spectra. The spectra show a different height of the peak of the Gaussian functions than in Figure 3.6, since the values of the discrete Fourier transformation are dependent on the number of grid points evaluated.

For $n = 5$ and $n = 10$ the spectra do change in the height of the Gaussian. We obtain three different energy levels for uniform grids, grids where the left hand side has been refined, and grids where the right hand side has been refined (color code). Differences for the different types of the transition zone and the change of resolution are marginal. The same properties are still visible for $n = 20$, although the H_0 run gives different results than the other two runs on uniform grids (H_1 and H_2). This indicates that the hardly resolved wave is already unstable on the coarsest grid. For the unresolved case with $n = 30$ it is difficult to draw conclusions from the approximated spectra, since most of the visible structures in the spectra are caused by aliasing effects. Still, since

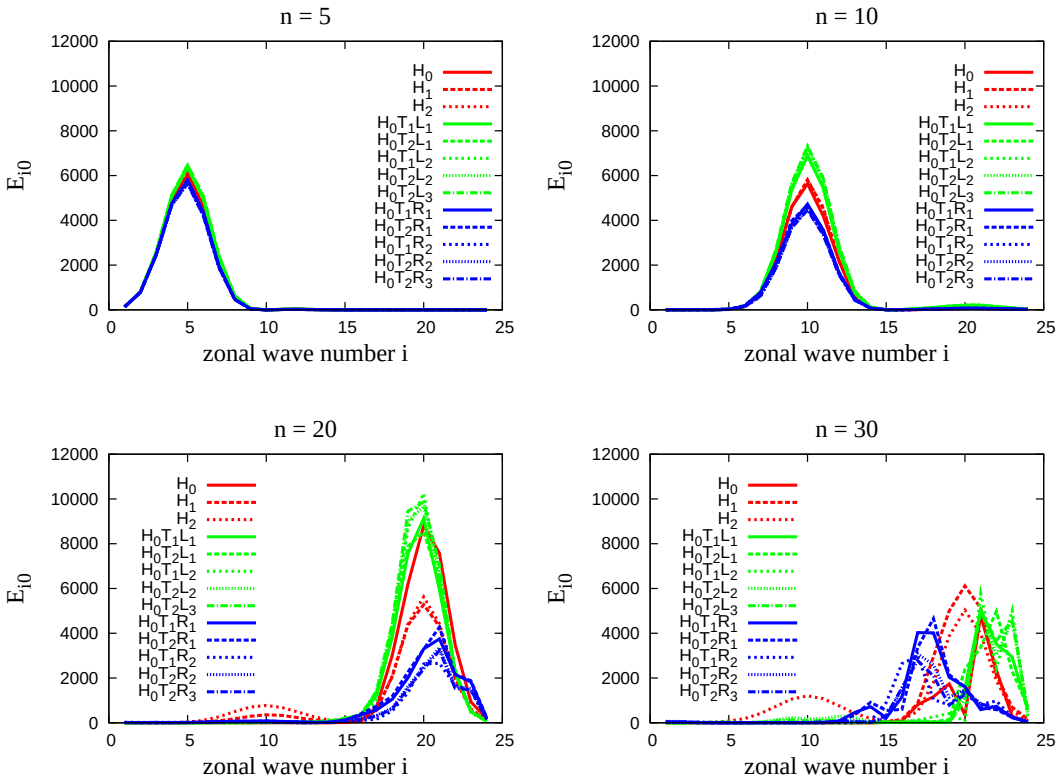

Figure 3.6: Approximated kinetic energy spectra after 20000 seconds for $n = 5$, $n = 10$, $n = 20$, and $n = 30$ (from top left to bottom right). The spectra are calculated evaluating all of the 50x8 vertices of the coarsest uniform grid, for the discrete Fourier transformations.

the spectra differ for all model runs, we can assume that the model fails to represent the wave packet on the coarsest and the refined grids.

We know that the considered shallow-water setup does not strictly conserve energy, although the error is very small (Chapter 2). Since energy conservation is very important for long term climate simulations, we test how the error is influenced by grid refinement. Figure 3.7 shows the relative error for energy for the different grids used. The procedure to calculate the relative error for energy is described in Appendix 3.B. For the grids in which the right hand side is refined (blue lines), the error follows the H_0 run, till the wave packet reaches the transition zone. Afterwards, the error depends only little on the refinement level and marginally on the type of transition zone. For the grids in which the left hand side is refined (green lines), the errors follow the uniform model runs with corresponding resolution, till the wave packet reaches the transition zone. Again, the errors differ only marginally for the different types of the transition zone. Ignoring the model runs on the $H_0T_2L_3$ and the $H_0T_2R_3$ grid, the relative er-

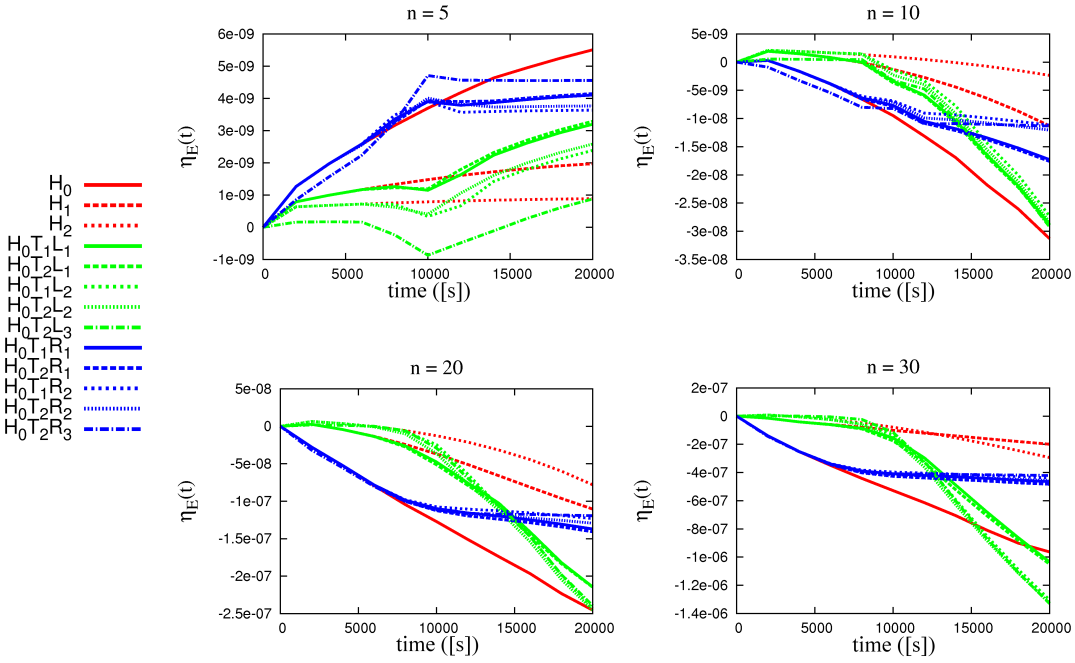

Figure 3.7: Time evolution of the relative error for energy for $n = 5$, $n = 10$, $n = 20$, and $n = 30$ (from top left to bottom right).

rors on the different grids lie in between the relative errors of the runs on the finest and coarsest uniform grids, for the cases where the wave packet is sufficiently resolved ($n = 5$ and $n = 10$). The model runs on the $H_0T_2L_3$ and the $H_0T_2R_3$ grid differ from the other runs for large wave length ($n = 5$ and $n = 10$). The limit for an unproblematic resolution difference between neighbored cells might be reached, but the errors might also be caused by the very steep angles used in the specific grids.

In simulations of atmosphere and ocean, wave patterns will hit a transition zone between coarse and fine parts of a grid with all angles. To test the influence of the angle a wave forms with the transition zone, we divide the rectangular domain by a diagonal, where either the lower left (H_0L_1diag), or the upper right (H_0R_1diag) part of the grid is refined by one refinement level, increasing the resolution by a factor of two. Figure 3.8 shows the approximated energy spectra of model runs on the two refined, and the uniform H_1 grid. Results are similar as for the runs where either the left or the right half of the domain is refined. The spectra are parted by the hand side of the grid that is refined.

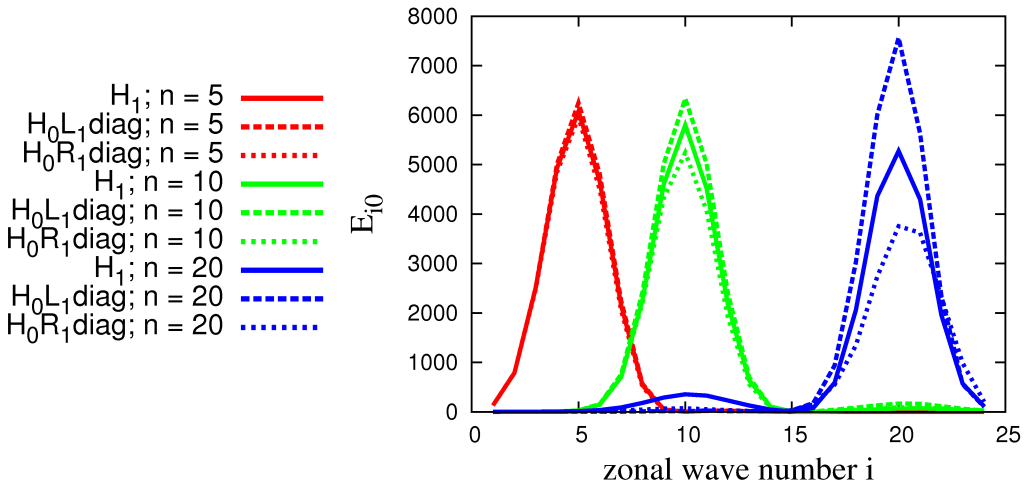

Figure 3.8: Test on diagonally refined grids: Approximated kinetic energy spectra after 20000s for different wave numbers. The spectra are calculated evaluating all of the 50x8 vertices of the coarsest uniform grid, for the discrete Fourier transformations.

Summary of the results

Waves that are hardly resolved on one side of the grid (less than five grid cells per wave length) are influenced severely when resolution is changing. Errors appear to be rather independent of the structure of the transition zone, and the amount of increase or decrease in resolution. The errors decrease fast with increasing wave length. Errors are dependent on the direction the resolution is changing (fine $\rightarrow$ coarse, or coarse $\rightarrow$ fine) and the wave length. The error in energy conservation is influenced by grid refinement, but it is typically getting smaller compared to the error on the corresponding unrefined grids. A change of the angle the incoming waves form with the change in resolution does not change the results qualitatively.

3.3.2 Geostrophic balance affected by grid refinement

In this subsection we simulate a steady Gaussian water hill in geostrophic balance. The test is well known from the literature to test the ability of newly developed discretization schemes to represent geostrophic balance. It is known from the results in Cotter et al. (2009a) that the considered $P_1^{DG}P_2$ element is able to represent the geostrophic balance on unstructured but uniform grids.

We evaluate a linearized version of the unforced, inviscid shallow-water equations, given by

$$\partial_t \mathbf{u} + f\mathbf{k} \times \mathbf{u} + g\nabla h = 0,$$

Parameter	Value
h_0	$5000.0\ m$
h_1	$500.0\ m$
L_x	$5.0 \cdot 10^6\ m$
L_y	$5.0 \cdot 10^6\ m$
σ_x^2	$\frac{9}{800} L_x^2$
σ_y^2	$\frac{9}{800} L_y^2$
f	$6.147 \cdot 10^{-5} \frac{1}{s}$

Table 3.2: Initial conditions for the geostrophic balance affected by grid refinement test.

$$\partial_t h + h_0 \nabla \cdot \mathbf{u} = 0,$$

using the f-plane approximation. We initialize the velocity field such that the height field is balanced in a steady state. The initial conditions are given by

$$u = g h_1 \frac{y - 0.5\ L_y}{f \sigma_y^2} \exp\left(-\frac{(x - 0.5\ L_x)^2}{2\ \sigma_x^2} - \frac{(y - 0.5\ L_y)^2}{2\ \sigma_y^2} \right),$$
$$v = -g h_1 \frac{x - 0.5\ L_x}{f \sigma_x^2} \exp\left(-\frac{(x - 0.5\ L_x)^2}{2\ \sigma_x^2} - \frac{(y - 0.5\ L_y)^2}{2\ \sigma_y^2} \right),$$
$$h = h_0 + h_1 \exp\left(-\frac{(x - 0.5\ L_x)^2}{2\ \sigma_x^2} - \frac{(y - 0.5\ L_y)^2}{2\ \sigma_y^2} \right).$$

where σ_x and σ_y are the standard deviations in the zonal and the meridional direction. The initial values used for our simulations are given in Table 3.2. The test is performed with periodic boundary conditions.

We use a grid that consists of 20x20 squares, each of them divided into two triangles, as the unrefined starting point for grid refinement. We develop two refined grids with two refinement levels, where each refinement level increases resolution by a factor of two. The refined region either forms a cross or a ring centered on the Gaussian hill. The grids are plotted in Figure 3.9.

Figure 3.10 shows the height field at initialization and after 1000 days for the different grids used. The height field remains steady in all simulations. Since we know the analytical solution, we can calculate the L^1- and L^2-error norms of the height field, given by

$$L^1(h) = \frac{\int_\Omega |h^n - h_a^n|\, dx}{\int_\Omega |h_a^n|\, dx}, \qquad \text{and} \qquad L^2(h) = \sqrt{\frac{\int_\Omega (h^n - h_a^n)^2\, dx}{\int_\Omega (h_a^n)^2\, dx}},$$

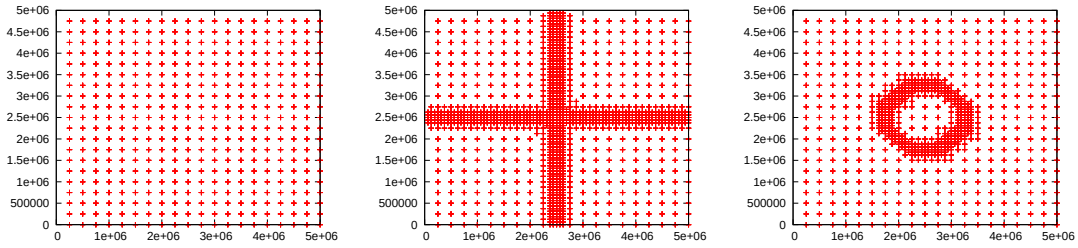

Figure 3.9: Positions of the vertices in the three grids used for the geostrophic balance affected by grid refinement test.

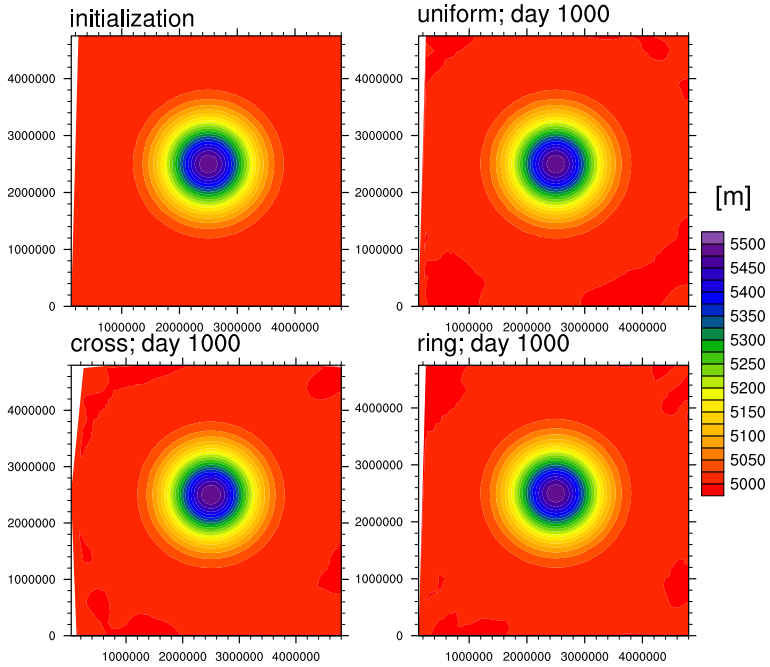

Figure 3.10: Height field at initialization (upper left) and after 1000 days for the uniform (upper right), the cross (lower left), and the ring grid (lower right).

where h^n is the computed height at time step n compared to the analytical solution h_a^n. Ω indicates that we integrate over the whole domain.

Figure 3.11 shows the L^1- and L^2-error norms of the height field against time for the different grids. The biggest contribution to the error is rooted in the initialization and not in the model error developing in the ongoing simulation. The developing error behaves similarly in all simulations.

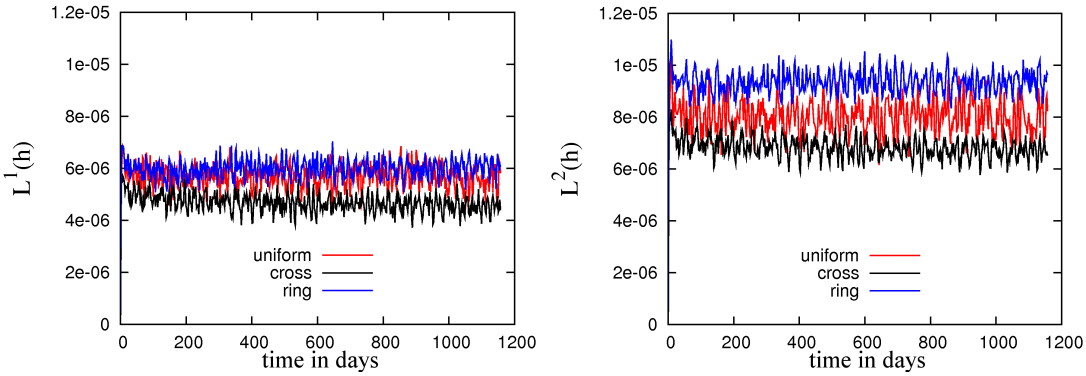

Figure 3.11: L^1-error (left) and L^2-error norm (right) of the height field against time for the different grids.

Summary of the results

The test shows that the used $P_1^{DG}P_2$ finite element setup is able to represent the geostrophic balance when grids of variable resolution are used.

3.3.3 Turbulent decay of randomly initialized fields

In this subsection we consider a test case in which the physical fields are initialized randomly on a plane. The test is typically used to evaluate the cascade of kinetic energy and enstrophy in turbulent two dimensional flows (McWilliams 2006), or for model evaluation (Ringler and Randall 2002; Bonaventura and Ringler 2005). In this publication, the test shall investigate the influence of grid refinement to turbulent decays.

In two dimensional turbulent flows, energy is transferred from smaller to larger scales. This is inverse compared to three dimensional turbulence (McWilliams 2006). The kinetic energy spectra should show a n^{-3}, and the enstrophy spectra a n^{-1} cascade with the wave number (Salmon 1998).

We use a grid that consists of 60x60 squares, each of them divided into two triangles, as the coarse uniform grid (H_0) for a periodic domain. We refine the H_0 grid on the whole domain to obtain a second uniform grid with doubled resolution (H_1). Furthermore, we build up two grids in which the resolution in the right hand side of the H_0 grid is increased by a factor of two or four (H_0R_1 and H_0R_2). The grids are plotted in Figure 3.12. The transition zone between the coarse and fine part of the grid is the same as for the $H_0T_1R_1$ and the $H_0T_1R_2$ grid, plotted in Figure 3.2.

To apply the same 'random' initial conditions on each grid, we need to provide the initial conditions as analytical functions. We initialize the fields as follows

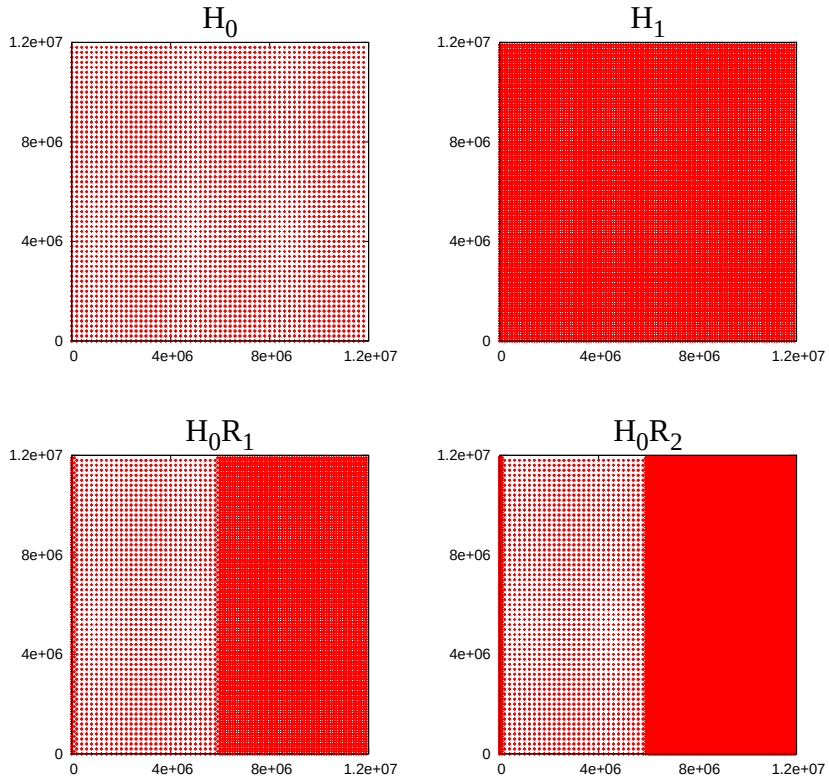

Figure 3.12: Positions of the vertices in the four grids used for the turbulent decay of randomly initialized fields test.

$$\phi(x,y) = \phi_0 + \sum_{i=1}^{30}\sum_{j=1}^{30} \phi_1 \sin\left(\frac{2\pi i x}{L_x} + r_{1,i}\right) \sin\left(\frac{2\pi j y}{L_y} + r_{2,j}\right) + \sum_{i=1}^{30} \phi_1 \sin\left(\frac{2\pi i x}{L_x} + r_{1,i}\right) + \sum_{j=1}^{30} \phi_1 \sin\left(\frac{2\pi j y}{L_y} + r_{2,j}\right),$$

where ϕ_0 and ϕ_1 are constants associated with the physical field ϕ, and $r_{1,i}$ and $r_{2,j}$ are random numbers that are equally distributed between zero and 2π. The initial values used for our simulations are written in Table 3.3. They result in absolute values of the velocity field that vary between $0.0\frac{m}{s}$ and $0.5\frac{m}{s}$, and a fluid depth between $350m$ and $450m$. The given initialization stimulates all kinetic energy modes that are possibly described on the H_0 grid with the same amplitude (white noise). Since the same initialization is performed for all grids, not all modes possible on the finer grids are stimulated. Tests are performed on an f-plane ($f = 1.0 \cdot 10^{-4} s^{-1}$) for the inviscid equations ($\nu = 0$), with a domain size of 12000x12000 km.

Parameter	Value
u_0	0.0
u_1	$0.01\frac{m}{s}$
v_0	0.0
v_1	$0.01\frac{m}{s}$
h_0	$400.0m$
h_1	$1.0m$

Table 3.3: Initial conditions for the energy decay for randomly initialized fields test.

Figure 3.13 shows the zonal velocity field on the different grids, and its evolution in time. It is visible that the eddy size increases with increasing time, and that the fields are finer resolved but qualitatively equivalent on the refined grids.

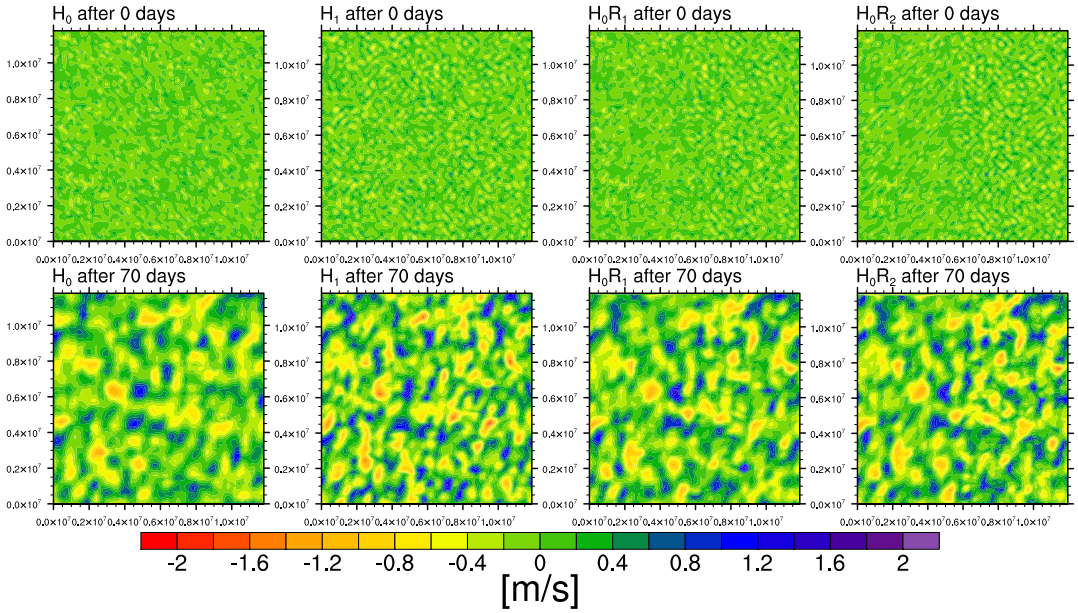

Figure 3.13: Zonal velocity on the H_0, H_1, H_0R_1, and H_0R_2 grid (from left to right) initially (top), and after 70 days (bottom).

To get a better impression of the influence of grid refinement to the turbulent cascade, we consider the energy and enstrophy spectra. To obtain an approximation of the kinetic energy and enstrophy spectra on the refined grids, we evaluate only the gridpoints in the initial, unrefined grid, as it is already done in subsection 3.3.1. Since it is difficult to read information from the two dimensional energy and enstrophy spectra, we present the spectra in one dimensional form. To this end, we take the average of all spectral coefficients that represent a wave length $\lambda = \sqrt{\lambda_x^2 + \lambda_y^2}$ within an interval

between L_x/i and $L_x/(i+1)$, $\forall i = 1, ..., 59$.

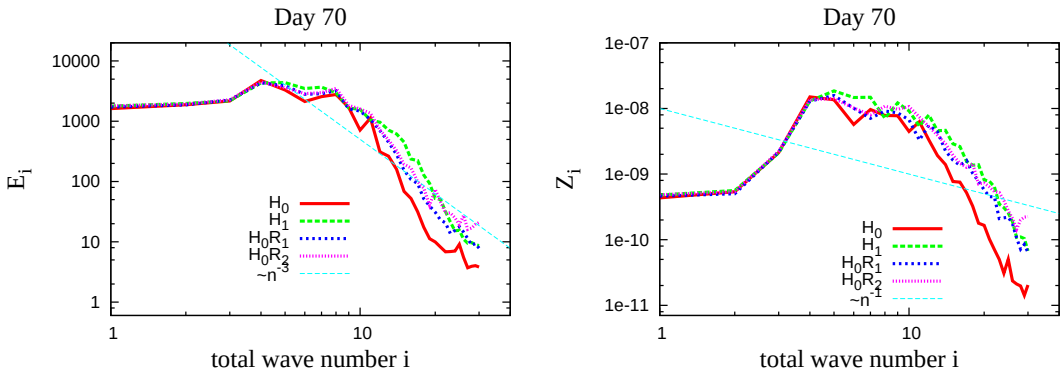

Figure 3.14: Approximated one dimensional kinetic energy (left) and enstrophy spectra (right) after 70 days. The spectra are calculated evaluating all of the 60x60 vertices of the coarsest uniform grid, for the discrete Fourier transformations.

Figure 3.14 shows the one dimensional kinetic energy and enstrophy spectra of the model runs. The spectra of the partly refined grids lie between the H_0 and H_1 spectra. The grid that was refined in two refinement levels, has a different higher energy and enstrophy spectra for the very small wave length; a behavior we would expect for a finer resolved model simulation, since less numerical diffusion is present.

Summary of the results

While the resolution is increased in the refined areas, we can not observe any spurious behavior at the transition zones between coarse and fine parts of the grids; neither in the physical fields, nor in the kinetic energy or enstrophy spectra. Unfortunately, the approximated spectra on the refined grids can not cover wave length that are smaller than two times the coarsest grid spacing.

3.3.4 Decay of a zonal flow over an isolated mountain

In this subsection we consider a test typically performed to evaluate atmospheric shallow-water models on the sphere. The test shall investigate the improvements possible with local grid refinement for the representation of topography in global applications. The test is known from Williamson et al. (1992) (test case 5) and consists of a global steady-state nonlinear zonal geostrophic flow that is perturbed by a mountain introduced into the northern hemisphere, behind which Rossby waves form and propagate over the globe.

The steady case specifies a zonal westerly flow with a maximum velocity of ca. 20 ms^{-1} and a fluid depth varying between 5960 and 7960 m. The test is performed

	Number of cells	Typical edge length on the sphere [m]	DOF for velocity component	DOF for height
H_0	1280	960000	3840	2562
H_1	5120	480000	15360	10242
H_2	20480	240000	61440	40962
H_0Re	1596	480000-960000	4788	3194
H_1Re	6182	240000-480000	18546	12366

Table 3.4: Properties of the grids used for the zonal flow over an isolated mountain test.

without viscosity ($\nu = 0$).

We perform simulations on five grids. Three of them are uniform icosahedral geodesic grids (H_0 - H_2). Additionally, we use the two refined grids H_0Re and H_1Re, in which the resolution around the mountain is increased by a factor of two starting from the H_0 or the H_1 grid. The refinement area spans the rectangular between the longitude values of -2.2 and -0.8 and the latitude values of 0.1 and 1.1 (in radian). Details on the grids are given in Table 3.4. In the refined grids, the number of degrees of freedom is increased by less the 25% compared to the unrefined partners.

Figure 3.15 shows the relative vorticity of the model runs for different time steps and grids. The visible distortion in the direct vicinity of the poles is a postprocessing artifact and occurs since the zonal velocity is not defined at the poles. It can be seen that the Rossby waves that form behind the mountain initialize a turbulent cascade. The transition zones between different refinement levels are not visible by eye.

Figure 3.16 and 3.17 show the kinetic energy and enstrophy spectra calculated for different time steps and grids. The procedure to calculate the kinetic energy spectra on a sphere is described in the Appendix 3.A. All spectra are in good agreement. For the long term runs (day 100) the refined grids produce a spectra closer to the runs on uniform grids with higher resolution, compared to their unrefined partners.

Summary of the results

The test shows that grid refinement allows considerable improvements for the representation of topography with small additional computational costs. No spurious behavior is visible. Neither in the physical fields, nor for the calculated spectra.

3.3.5 Perturbed jet stream

In this subsection we simulate the decay of a perturbed jet stream test proposed in Galewsky et al. (2004). The test is typically performed to test the accuracy of global shallow-water models. We use the test to investigate possible improvements with grid

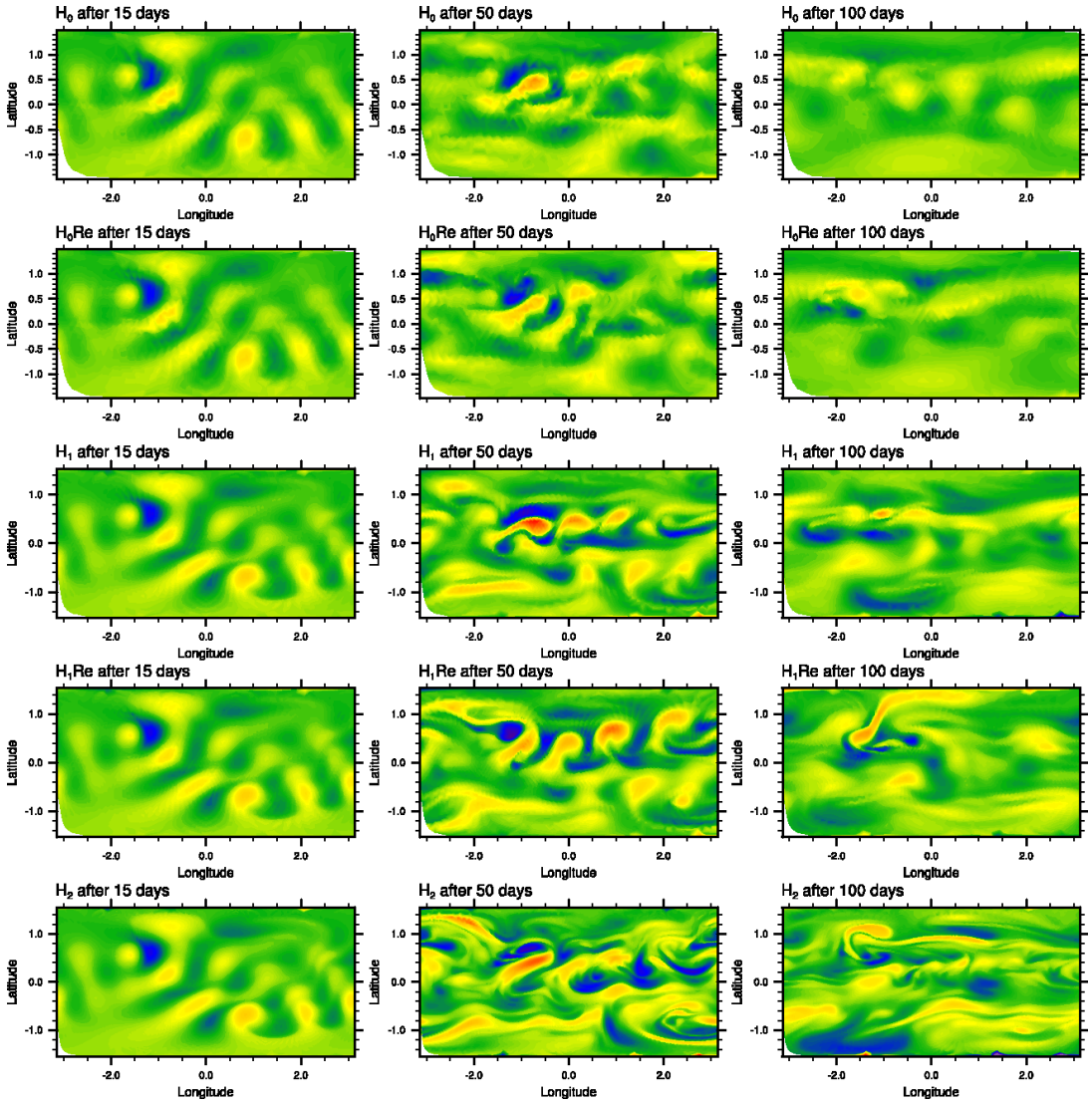

Figure 3.15: Relative vorticity for the different grids (H_0, H_0Re, H_1, H_1Re, and H_2, from top to bottom) and different time steps (after 15, 50, and 100 days, from left to right).

refinement for the representation of local wave patterns. The setting represents a barotropically unstable mid latitude jet balanced by the height field, for the inviscid equations ($\nu = 0$). While a model run initialized only with the jet stream should stay unchanged, a small height perturbation is added to the initial state to destabilize the whole setup. After several days of integration the perturbation leads to a turbulent decay of the solution.

A sufficient resolution is required to perform a proper decay of the perturbed jet. If

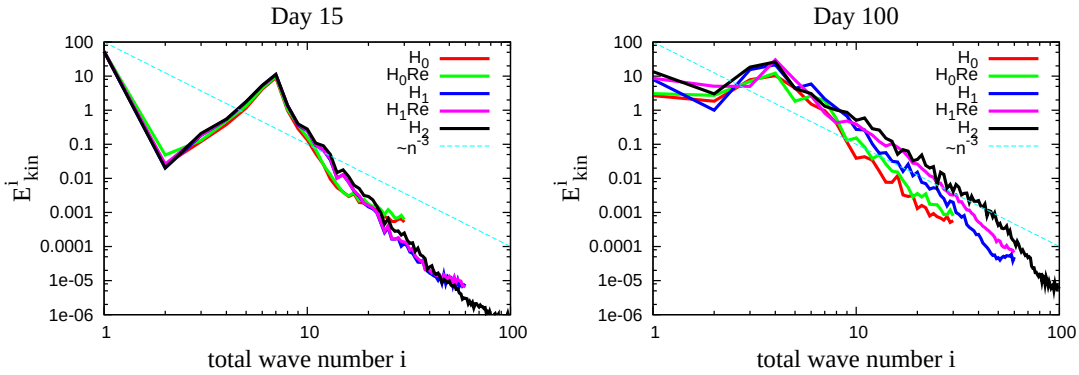

Figure 3.16: One dimensional kinetic energy spectra on the sphere for the different grids. After 15 (left) and 100 days (right).

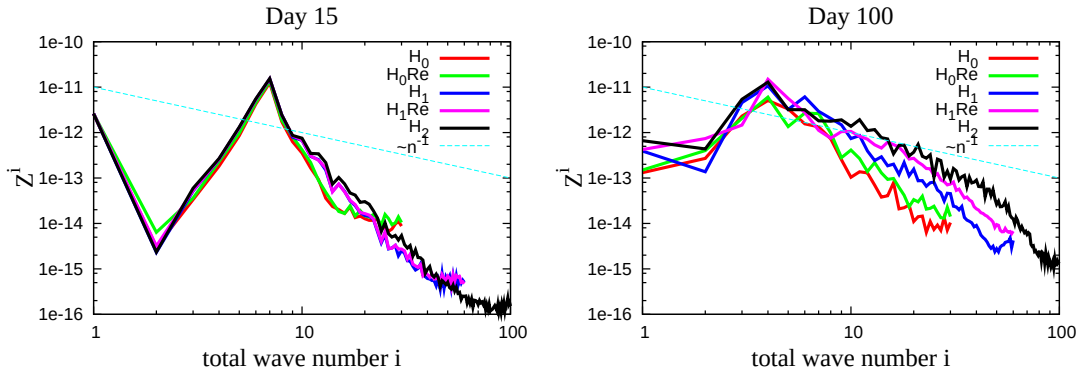

Figure 3.17: One dimensional enstrophy spectra on the sphere for the different grids. After 15 (left) and 100 days (right).

the resolution is too coarse, the model error initializes a premature decay of the jet. We performed model simulations on four different grids that are described in Table 3.5. Grid 1, Grid 2, and Grid 3 are uniform icosahedral geodesic grids of different resolution. Grid 4 is a refined grid that is developed starting from a coarse uniform geodesic grid. It is refined in three levels towards the mid latitudes in which the jet is located.

Figure 3.18 shows the decay of the perturbed jet on the different grids. Only the tests with the highest local resolution at the jet are able to perform a proper decay that is similar to results from the literature (Galewsky et al. 2004). These are the runs performed on the uniform Grid 3 and the refined Grid 4. For the very localized jet, grid refinement manages to reduce the number of degrees of freedom in Grid 4 by a factor of more than four, compared to Grid 3, obtaining the qualitatively same results.

	Number of cells	Typical edge length on the sphere [m]	DOF for velocity component	DOF for height
Grid 1	20480	240000	61440	40962
Grid 2	81920	120000	245760	163842
Grid 3	327680	60000	983040	655362
Grid 4	73770	60000-480000	221310	147542

Table 3.5: Properties of the grids used for the perturbed jet stream test.

Summary of the results

The test shows that grid refinement allows a significant reduction of computational cost to obtain the same quality of results for simulations of a local wave pattern. The number of the used degrees of freedom was reduced by a factor of more than four. No spurious modes are visible.

3.3.6 Ocean gyre test case

In this subsection we consider an ocean test case of a wind driven ocean gyre on a planar rectangular domain. The test shall investigate the improvements possible with local grid refinement for the representation of western boundary currents. A similar test was performed in Comblen et al. (2010) to test the properties of several finite elements discretization methods, including the considered $P_1^{DG}P_2$ element. In difference to Comblen et al. (2010) we particularly focus on improvements possible with grid refinement and use grids with abrupt changes of the grid spacing.

A wind forcing induces a clockwise circulation in a planar rectangular ocean basin. Due to the change of the Coriolis parameter in the meridional direction the gyre is intensified towards the western boundary, and a western boundary current develops (Pedlosky 1996). The test is realized with free-slip boundary conditions ($\mathbf{u}\cdot\mathbf{n}=0$, and $\frac{\partial \mathbf{u}}{\partial \mathbf{n}}=0$ on $\partial\Omega$).

The domain has the dimensions of 1000x1000 km and is located in the northern hemisphere. The Coriolis parameter is given in β-plane approximation by

$$f = 10^{-4}s^{-1} + 4.0 \cdot 10^{-11} y s^{-1},$$

where y is the meridional coordinate.

Wind forcing and bottom friction are introduced to the differential equation with the following forcing terms

$$\boldsymbol{\tau} = \frac{\boldsymbol{\tau}^s}{H} - \gamma \mathbf{u},$$

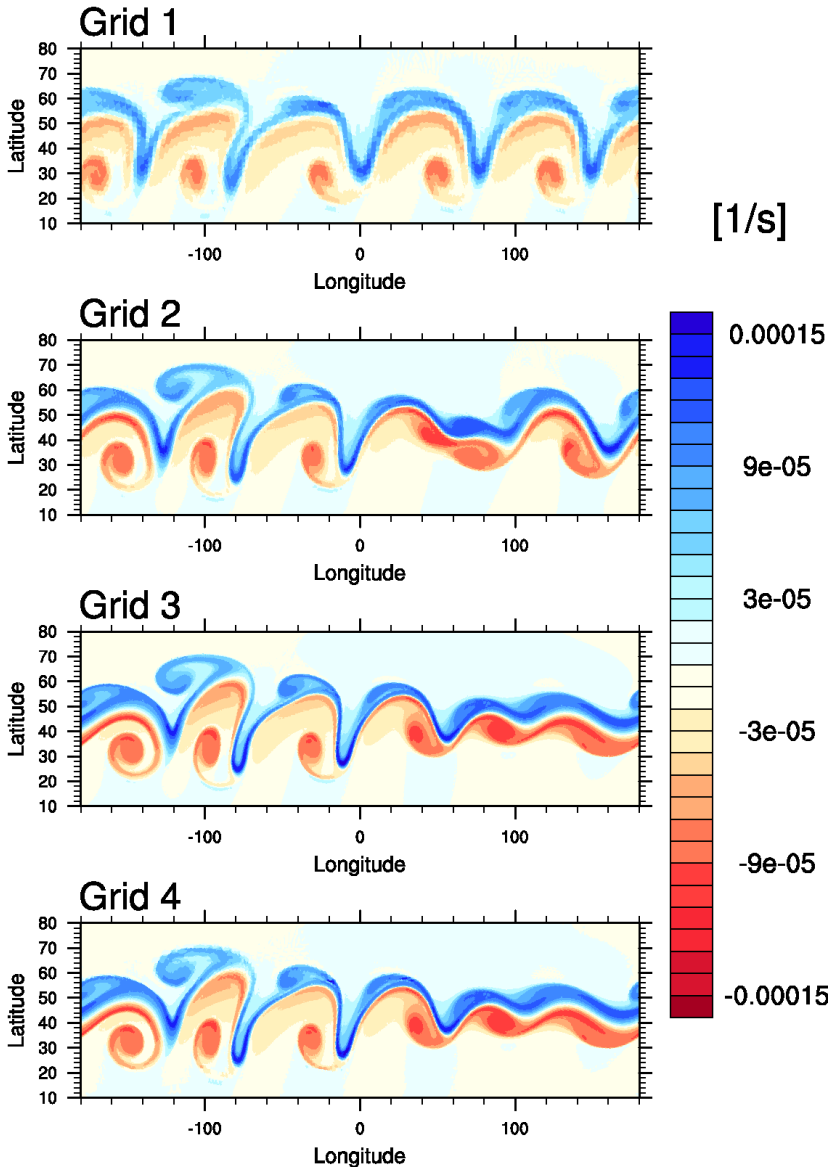

Figure 3.18: Vorticity field of the perturbed jet stream test on the uniform Grid 1, Grid 2, and Grid 3, and the refined Grid 4 after six days (from top to bottom).

where $\boldsymbol{\tau}^s$ is the surface wind stress, and γ is the bottom friction coefficient set to $10^{-6}s^{-1}$.

While the meridional wind stress is zero, the zonal wind stress is set to

$$\tau_x^s = -1.5 \cdot 10^{-3} \cdot \cos\left(\frac{\pi y}{L}\right) \frac{m^2}{s^2},$$

where L is the length of the domain in meridional direction.

Grid	Number of cells	DOF for velocity component	DOF for height	Viscosity ν in $[m^2 s^{-1}]$
Grid 1	796	2388	1683	1637
Grid 2	2048	6144	4225	1637
Grid 3	1829	5487	3810	205
Grid 4	8192	24576	16641	205

Table 3.6: Properties of the grids used for the ocean gyre test.

The test case is initialized with a constant water depth of $1000m$; velocity is set to zero.

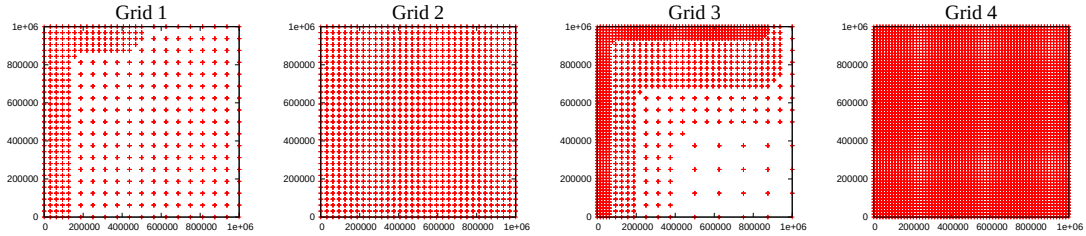

Figure 3.19: Positions of the vertices in the Grid 1-4 (from left to right) used for the ocean gyre test.

We use four different grids for the simulations. Two grids that offer a uniform resolution (Grid 2 and Grid 4), and two grids in which the area interesting for the representation of the western boundary current is refined (Grid 1 and Grid 3). The Grids 1 and 2, and 3 and 4 have the same maximal resolutions. The positions of the degrees of freedom for the velocity field are plotted in Figure 3.19 for the different grids. In the test runs viscosity is chosen such that the Munk layer at the western boundary is resolved by at least two grid cells, and is therefore dependent on the grid resolution at the western boundary. The constraint that assures that the Munk layer is resolved by at least N grid points in a global finite difference model is given by (Griffies 2004)

$$\nu > 3.82 \cdot 10^{-12} \left(N \Delta s\right)^3 \cos\left(\theta\right) m^{-1} s^{-1}, \tag{3.3}$$

where Δs is the lattice spacing and θ is the latitude. We calculate the values needed for eddy viscosity, to resolve the Munk layer with two grid cells, with an equation similar to equation (3.3) derived for the β-plane approximation. Using a lower viscosity leads to an insufficiently resolved western boundary current. The number of cells in the different grids and the used values for viscosity are written in Table 3.6.

Figure 3.20 shows the height field of the model runs on the different grids after 200 days. Differences between the model results on refined or uniform grids with the same

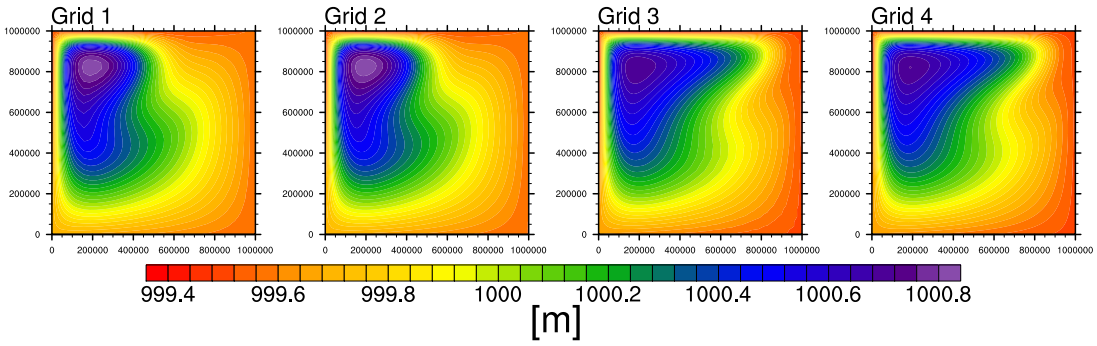

Figure 3.20: Height field of the ocean gyre simulations on Grid 1-4 (from left to right).

maximal resolution and eddy viscosity are hardly visible, although the grid refinement can decrease the number of degrees of freedom by a factor up to more than 4.

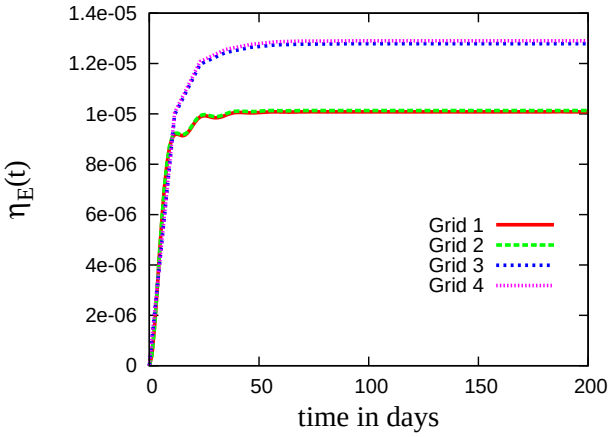

Figure 3.21: Time evolution of the relative change in energy for the different grids.

Energy is not conserved in the considered system, since the applied wind forcing acts as a source, the bottom friction as a sink of energy. For the given resolution we expect the model runs to be steady, and the total energy to equilibrate at a fixed value, after some time. Figure 3.21 shows the relative change of total energy with time. After 200 days, the system is well equilibrated. It is visible that the total energy in the system is dependent on the viscosity value. Refined and unrefined grids obtain the same results for total energy.

Summary of the results

The test shows that grid refinement allows a marked improvement of the representation of boundary currents. The increased resolution at the western coast line allows a

reduction of eddy viscosity, which leads to a more realistic representation of ocean flows.

3.4 Conclusion

Concerning the set of research questions stated in the introduction, we conclude:

1. The simulations of wave packets (subsection 3.3.1) show that waves represented by less than five grid cells per wave length are strongly reflected and scattered at the transition between coarse and fine grids. Large-scale flow features are unaffected by grid refinement in all tests performed. At the small lengths scales in which errors appear, diffusion is very much apparent and might remove spurious waves or oscillations quickly.

2. The simulations of wave packets (subsection 3.3.1) show that errors are fairly independent of the structure of the transition zone and the change of resolution between fine and coarse parts of the grids.

3. The finite element shallow-water configuration appears robust for the use on refined grids in all tests performed. The model performs well for abrupt changes in grid resolution tested for up to a factor of 8. However, the use of grids with very steep angles – less than 10 degrees – can lead to a small increase of the error in energy conservation (subsection 3.3.1).

4. The simulations of a Gaussian water hill in geostrophic balance (subsection 3.3.2) show that grid refinement does not perturb the representation of the geostrophic balance in the considered finite element configuration.

5. The simulations of randomly initialized physical fields (subsection 3.3.3) show that grid refinement does not deteriorate turbulent cascades in the considered finite element configuration. The simulations of wave packets (subsection 3.3.1) show that the error in energy conservation is influenced by grid refinement, but it is typically getting smaller compared to the error on the corresponding unrefined grids.

6. Grid refinement can lead to a significant improvement of the representation of topography, local wave patterns, and western boundary currents. This is shown by simulations of a decay of a zonal flow over an isolated mountain (subsection 3.3.4), a perturbed jet stream (subsection 3.3.5), and wind driven ocean gyres (subsection 3.3.6).

7. The simulation of wave packets (subsection 3.3.1) and turbulent cascades (subsection 3.3.3), combined with a calculation of approximated spectra for kinetic

energy and enstrophy, using discrete Fourier transformations, allows a qualitative description of the errors caused by grid refinement. However, a quantitative description, as it is possible for linear systems via analytic considerations, is not delivered by the results of this publication.

The results of this paper indicate that the improvements possible with a deliberated use of static, local grid refinement, justify the risk of spurious reflections and scatterings in the considered finite element shallow-water model for geophysical applications.

3.A Kinetic energy and enstrophy spectra on plane and sphere

The model runs are evaluated with kinetic energy and enstrophy spectra. Using a discrete Fourier transformation, we calculate the spectral coefficients $\hat{\phi}_{ij}$ of a two dimensional physical field ϕ on an regular equidistant grid on the plane via

$$\hat{\phi}_{kl} = \sum_{m=0}^{N_x-1} \sum_{n=0}^{N_y-1} \phi_{mn} \exp\left(-2\pi \mathrm{i} \frac{mk}{N_x}\right) \exp\left(-2\pi \mathrm{i} \frac{nl}{N_y}\right),$$

where $\phi_{mn} = \phi(x_m, y_n)$ is the value of the physical field at a given grid point ($\forall m = 1, 2, 3, ..., N_x$, and $\forall n = 1, 2, 3, ..., N_y$). We define the factor $\frac{1}{N_x N_y}$ to be introduced in the inverse transformation back to physical space.

Calculating the spectral coefficients for the two components of the velocity fields ($\hat{u}_{kl}$ and $\hat{v}_{kl}$), we consider the two dimensional spectra of the kinetic energy calculated by

$$E_{kl} = \frac{1}{4}\left(|\hat{u}_{kl}|^2 + |\hat{v}_{kl}|^2\right).$$

Calculating the spectral coefficients for vorticity ($\hat{\zeta}_{kl}$), we calculate the enstrophy spectra by

$$Z_{kl} = \frac{1}{4}\left|\hat{\zeta}_{kl}\right|^2.$$

To calculate the spectra of the kinetic energy and enstrophy on the sphere, we proceed as follows. In a first step, the relative vorticity and divergence are calculated as curl and divergence of the velocity. In a second step, vorticity and divergence are mapped onto a Gaussian grid. In a third step, the spectral coefficients of vorticity and divergence (ζ_n^m and δ_n^m) are calculated. Steps two and three are performed using the Climate Data Operator tools (CDO, Müller and Schulzweida 2010).

The spectra of kinetic energy E_{kin}^n and enstrophy Z^n are given by

$$E_{\text{kin}}^{n} = \frac{a_e^2}{4n\,(n+1)} \left(\left|\zeta_n^0\right|^2 + \left|\delta_n^0\right|^2 + 2\sum_{m=1}^{n} |\zeta_n^m|^2 + 2\sum_{m=1}^{n} |\delta_n^m|^2 \right), \tag{3.4}$$

$$Z^n = \frac{1}{4} \left(\left|\zeta_n^0\right|^2 + \sum_{m=1}^{n} 2\,|\zeta_n^m|^2 \right),$$

where n is the wave number. A derivation of equation (3.4) is given in Jakob et al. (1993).

3.B Energy conservation

We calculate the global energy at time step n using the following formula

$$E^n = \int_\Omega \left(\frac{1}{2} h^n \mathbf{u}^n \cdot \mathbf{u}^n + \frac{1}{2} g\,(h^n h^n - h_b^n h_b^n) \right) dx.$$

We compute the relative error for total energy at time step n using the initial value as a reference

$$\eta_E\,(t_n) = \frac{\left|E^0 - E^n\right|}{E^0}. \tag{3.5}$$

Chapter 4

A study of model parameters and discretized fields that influence boundary separation

We study boundary currents and boundary separation in a finite element shallow-water model. First, we evaluate the influence of local resolution, eddy viscosity, the grid structure, and the boundary conditions on the numerical representation of boundary currents. Then, we identify appropriate criteria to detect boundary separation points in ocean modeling. To find these criteria, we study the physical fields along the coast line, and evaluate classical and recent theories for flow separation in Fluid Dynamics.

For our investigations we simulate steady separation of western boundary currents from idealized and realistic coast lines, and unsteady separation at an island in a geostrophic flow. The used finite element model offers a sound representation of the coast line and the boundary conditions. The use of grid refinement allows a detailed investigation of boundary separation at reasonable numerical cost.

4.1 Introduction

The mechanisms that influence the separation of boundary currents in the ocean are poorly understood. Numerical models can provide only a small contribution to a better understanding of boundary separation, since the properties of the coast line as it is represented in today's ocean models are fairly different to the properties of the coast line in real-world oceans, mainly due to the coarse resolution. The purpose of the first part of this paper is to improve our understanding of boundary currents and boundary separation in finite element ocean models. The purpose of the second part of this paper is to identify proper criteria to detect boundary separation points in ocean modeling.

For the separation of boundary currents in the ocean, such as the separation of the Gulf stream, there are many possible mechanisms that might influence the position of the separation point. For the Gulf stream these mechanisms are a change of the direction in the wind field, a potential vorticity crisis, an adverse pressure gradient, a collision with another western boundary current, an outcropping of isopycnals, inter-

actions with the deep western boundary current, the coast line geometry, the bottom topography, or eddy-topography interactions (see Chassignet and Marshall 2008, and the references therein).

While the Gulf stream tends to overshoot the separation point of the real world in standard numerical ocean models, state-of-the-art high-resolution model simulations, with a grid resolution of $1/10^\circ$ or higher, obtain an improved representation of Gulf stream separation (Bryan et al. 2007; Chassignet and Garrao 2001). However, high-resolution does not guarantee a proper representation of the Gulf stream, and the separation point remains sensitive to changes in the model setup, such as changes in viscosity parameterization (Bryan et al. 2007). The choice of boundary conditions is known to have a significant influence on the separation behavior, as well (Dengg 1993).

The discretization method that is mainly used in today's state-of-the-art ocean models – the finite difference method – offers only a poor representation of the coast line. To introduce a coast line into a finite difference model, grid points on land are typically removed from a fixed grid. The structured longitude/latitude grids only allow an angle of 0 or 90 degrees between neighbored grid edges along the boundary. This leads to staircase patterns at the coast line. Furthermore, due to the staggering of the velocity components, the effective boundary conditions can be dependent on the angle between the coast line and the coordinate axis of the numerical grid (see Adcroft and Marshall 1998, for the analysis on an Arakawa C-grid). These problems should not appear in finite element models, in which the velocity field is defined as two-dimensional vector quantity all along the coast line. The high geometric flexibility allows the use of boundary conforming grid generators, in which the boundary grid points are aligned to the coast line.

For investigations of boundary separation in ocean models, much can be learned from theories for continuous flow separation in Fluid Dynamics. Although we are not able to recapitulate all of the numerous publications in Fluid Dynamics that investigate boundary separation, we will give a short introduction to the most important literature for this paper. The first successful attempt to understand boundary separation was carried out by Prandtl in 1904 (Prandtl 1904). He developed a theory for flow separation of steady flows on no-slip boundaries, based on the wall shear and its gradient. The theory does not capture unsteady separation (Sears and Tellionis 1975). One of the most famous approaches to unsteady flow separation was the development of the Moore-Rott-Sears criteria. Unfortunately, it is difficult to evaluate these criteria, since the trajectory of a separation point needs to be known *a priori* (Williams 1977).

In a recent approach to unsteady boundary separation, Haller studied separation from a dynamical systems point of view. He developed a theory for unsteady but fixed separation of two dimensional flows from no-slip boundaries (Haller 2004). The flow trajectory at the separation point is assumed to be non-hyperbolic. He derived higher order approximations for the unsteady separation profile in the vicinity of the

separation point, evaluating only the physical fields along the coast line. The theory includes necessary and sufficient criteria for flow separation points. Hallers criteria extend Prandtls criteria to unsteady but fixed separation.

Another approach from dynamical systems theory was done by Lekien and Haller for free-slip boundaries (Lekien and Haller 2008). Here, the flow trajectories at the separation points are assumed to be hyperbolic, and not non-hyperbolic as in the no-slip case. Lekien and Haller elaborated necessary and sufficient criteria for unsteady and moving flow separation points.

Both approaches from dynamical systems theory have one major drawback: In principle the separation criteria are only valid if integrated over an infinite time interval. This is not applicable for numerical simulations. The use of limited integration times is known to be problematic in the evaluation of dynamical systems quantities based on infinite time integrations (see for example Branicki and Wiggins 2010).

Another recent approach to unsteady separation studied the topology of flow fields. In a series of papers (Ma and Wang 2001; Ghil et al. 2001, 2004, 2005) Ghil, Ma, and Wang present a theory to determine structural bifurcations of two dimensional incompressible vector fields. They investigated mainly no-slip, but also free-slip boundary conditions. In contrast to the approaches discussed above, the theory provides criteria for the emergence of a new separation point, together with a reattachment point, from a flow field parallel to the coast. The criteria are dependent on the vorticity along the coast line.

Despite the improved coast line representation in finite element methods, a detailed analysis of the properties of boundary currents and boundary separation has not been done for finite element models with realistic coast lines for ocean models. The same is true for a detailed study of the behavior of the physical fields along a coast line as used in ocean models, and a test of the applicability of the theories by Haller, Lekien and Haller, and Ghil, Ma, and Wang, in ocean modeling. This paper is meant to close these gaps.

In the first part of this paper (section 4.4), we study the numerical representation of western boundary currents in finite element models and compare the results to finite difference simulations from the literature. We simulate the separation of steady western boundary currents from idealized coast lines, and coast lines as used in ocean models. We vary the resolution, the eddy viscosity, the grid structure, the coast line, the alignment between the velocity components and the coast line, and between no-slip and free-slip boundary conditions. We evaluate the influence of these properties on boundary currents, and boundary separation. The test setups used in this publication do not fundamentally differ from setups used in publications such as Dengg (1993), Haidvogel et al. (1992), or Özgökmen et al. (1997) for simulations with finite difference models with vorticity as prognostic quantity. The main difference is that we use a finite element model, and velocity and height as prognostic quantities.

In the second part of this paper (section 4.5), we try to identify proper criteria to detect boundary separation points in ocean modeling, for free-slip and no-slip boundary conditions. To this end, we evaluate the physical fields along the coast line. If we are able to identify separation points, by evaluating a specific physical quantity, it is very likely that this quantity does trigger or at least influence boundary separation. Our study can therefore improve the understanding of the mechanism of boundary separation in numerical models, and probably also in real oceans. A proper criterion to detect flow separation points might also allow a proper definition of flow separation points in ocean models, or enable to adapt the local grid resolution and parameterization in the vicinity of a detected separation point, within a running ocean model.

Our investigations to detect separation points are based on the theories by Prandtl, Haller, Lekien and Haller, and Ghil, Ma, and Wang, but also on the analysis of the mechanism of flow separation performed within this publication. We study five approaches to identify separation points, where each approach evaluates specific physical quantities along the coast line. These quantities are the change of the tangential velocity in the normal direction, the vorticity, the change of the tangential velocity in the tangential direction, the change of the normal velocity in the normal direction, the ratio between the tangential and the normal components of velocity, and the gradient of the height field. All approaches are analyzed for no-slip and free-slip boundary conditions. We use some of the evaluated criteria beyond their theoretical limits, since it is possible that a criterion provides good results to detect separation points, when it is applied to flow fields that are not captured by the theoretical derivation.

For simplicity, we try to detect separation points during post processing, but all approaches could also be evaluated within a model run, in the same way. All of the evaluated methods are computationally cheap, since they solely consider the physical fields along the one-dimensional coast line. Since all approaches are tested for the same set of equations, and with the same model, this paper allows a direct comparison of the results for the different theories for boundary separation.

In section two, we give a very short description of the model setup, including the shallow-water equations, the discretization in space and time, and grid refinement. In section three, we introduce the three test cases. In section four, we present the numerical results on the properties of western boundary currents. In section five, we present the numerical results on the criteria to detect boundary separation points. In section six, we discuss the results. In section seven, we give the main conclusions.

4.2 Model setup

This section will give a brief introduction to the functionality of the used model, including the shallow-water equations, the discretization in space and time, and the used grids. A detailed description of the model setup can be found in Chapter 2.

4.2.1 The viscous shallow-water equations

Our finite element model simulates the viscous shallow-water equations in non-conservative form

$$\partial_t \mathbf{u} + \mathbf{u} \cdot (\nabla \mathbf{u}) + f\mathbf{k} \times \mathbf{u} + g\nabla h - \frac{1}{H}\nabla \cdot (H\nu (\nabla \mathbf{u})) = \frac{\boldsymbol{\tau}^s}{H} - \gamma_f \mathbf{u},$$
$$\partial_t h + \nabla \cdot (H\mathbf{u}) = 0,$$

where $\mathbf{u}$ is the two dimensional velocity vector, f is the Coriolis parameter, $\mathbf{k}$ is the vertical unit vector, g is the gravitational acceleration, ν is the eddy viscosity, $\boldsymbol{\tau}^s$ is the surface wind stress, γ_f is the bottom friction coefficient, h is the surface elevation, and H is the height of the fluid column given by $H = h - h_b$, where h_b is the bathymetry. The prognostic variables are the surface elevation and the velocity.

The used model can run with either free-slip ($\mathbf{u} \cdot \mathbf{n} = 0$, and $\partial_{\mathbf{n}}\mathbf{u} = 0$ on $\partial\Omega$), or no-slip boundary conditions ($\mathbf{u} = 0$ on $\partial\Omega$). To introduce free-slip boundary conditions, we adjust the numerical fluxes through the boundaries. To introduce no-slip boundary conditions, we set the normal velocity flux at the boundary to zero, and add a penalty term to the velocity equation, that pushes the tangential velocity along the boundary towards zero.

4.2.2 Discretization in space and time

Following the typical finite element approach, we expand the physical fields into sets of basis functions N_i and M_i

$$\mathbf{u} = \sum_{i=1}^{N_u} \mathbf{u}_i N_i \qquad \text{and} \qquad h = \sum_{i=1}^{N_h} h_i M_i.$$

We use a $P_1^{DG}P_2$ finite element approach to discretize the equations. This means that we employ discontinuous linear Lagrange polynomials for the representation of the velocity field (N_i), and globally continuous quadratic Lagrange polynomials for the representation of the height field (M_i). Each triangular cell has three degrees of freedom for each component of velocity located at the vertices of the cells, and six degrees of freedom for the height field located at the vertices and edges. While the degrees of freedom of the height field are shared with the surrounding cells, the degrees of freedom of the velocity field belong to a specific cell, which leads to a discontinuous representation.

To expand the physical fields into sets of basis functions, the triangles in physical space need to be mapped onto a reference triangle on which the basis functions are defined. On the sphere, the geometry of the physical triangles is given by trigonometric functions and cannot be mapped exactly onto a reference triangle, which is typically

defined on the plane. To this end, a stereographic projection is introduced into the model. The projection maps the sphere from one of the poles onto a planar domain at the opposed side of the sphere. The physical triangles can be defined as planar triangles on the stereographic domain, which allows an exact mapping to the reference triangle.

Time integration is performed by an explicit three level Adams-Bashforth method. The equation

$$\partial_t \boldsymbol{\psi} = R(\boldsymbol{\psi}),$$

where R denotes the right-hand-side of the system, and $\boldsymbol{\psi}$ is the vector of prognostic variables, is discretized in time by

$$\boldsymbol{\psi}^{n+1} = \boldsymbol{\psi}^n + \Delta t \left(\frac{23}{12} R(\boldsymbol{\psi}^n) - \frac{4}{3} R(\boldsymbol{\psi}^{n-1}) + \frac{5}{12} R(\boldsymbol{\psi}^{n-2}) \right),$$

where $\boldsymbol{\psi}^i$ is the vector of state variables at the i-th time step.

4.2.3 Grids and grid refinement

We use two types of standard grids on which refinement is performed. The first type of grids are structured triangular grids that provide a uniform coverage of the longitude/latitude space. The grids are derived from rectangular grids by bisecting each rectangular into two triangles. The second type of grids are icosahedral geodesic grids that provide a quasi-uniform coverage of the sphere (Baumgardner and Frederickson 1985). We use h-refinement to refine the interesting area around the coast line. In h-refinement, new grid points are introduced to the grid, to increase the model resolution in regions of specific interest. The influence of grid refinement to the model solution is investigated in Chapter 3.

4.2.4 Diagnostic tools for the identification of separation points

To identify separation points we evaluate the velocity and the height field and their derivatives along the coast line. For dynamical systems considerations, the quantities need to be defined continuously in space and time, and not as discrete values, as in the model output. To this end, we use a bicubic spline interpolation to get a smooth representation of the diagnosed quantities along the coast, and a third order Lagrange interpolation in time, to get a smooth representation between the time slices of the model output. As studied in Mancho et al. (2006) this seems to be the best choice for dynamical systems considerations of discrete model output. Time interpolation is necessary, since we do not output the quantities after each time step, due to limitations in storage capability. When a second spatial derivative in the tangential direction is needed for one of the physical quantities, we calculate it by central differentiation, evaluating the values of the quantity in the two neighboring grid edges.

We use the original discontinuous finite element velocity field to calculate the particle trajectories along the boundary for free-slip boundary conditions. The discontinuous velocity field is smoothened in time by first order Lagrange interpolation. The use of higher order interpolation methods does not change the results significantly, since the distances between the time steps are small enough.

4.2.5 Separation points and flow around a turn of the coast line

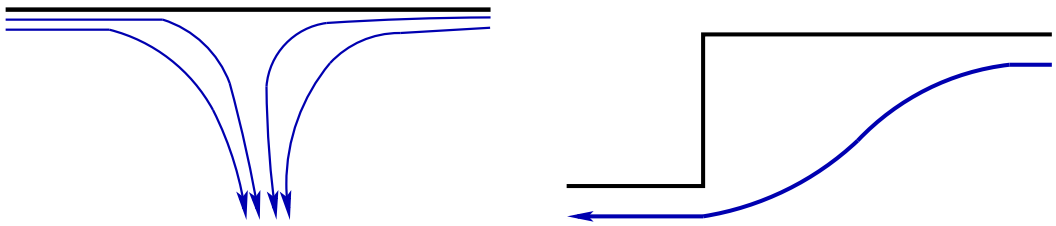

Figure 4.1: Sketch of a clear separation point (left), and a flow around a turn of the coast line (right).

The difference between clear separation points and a flow around a turn of the coast line is sketched in Figure 4.1. It is arguable if the flow around a turn of a coast line should be counted as separation point. The flow is separating, but directly reattaching. In this paper, we will distinguish between separation points and flow around a turn of the coast line.

4.3 Test cases

In this section, we introduce the three tests that we evaluate to study the properties of boundary separation in finite element models in section 4.4, and to identify criteria to detect boundary separation points in section 4.5. In the idealized coast line test, we simulate a steady wind driven western boundary current that separates at the corner of an obstacle. In the Atlantic test, we study a steady, wind driven circulation in an Atlantic shaped basin. In the island test, we study the unsteady separation of geostrophic flows around an island.

4.3.1 The idealized coast line test

We study an ocean gyre in the northern hemisphere. The gyre is forced by the wind and rotates in clockwise direction. Due to the change of the Coriolis parameter in the meridional direction, the gyre is intensified towards the western boundary, and a western boundary current develops (Pedlosky 1996). The current separates from the coast at the edge of a rectangular obstacle. Besides the obstacle, all coast lines are

straight. The setup is chosen to be as close as possible to the setup used in Dengg (1993). Dengg investigated boundary separation in a barotropic vorticity model.

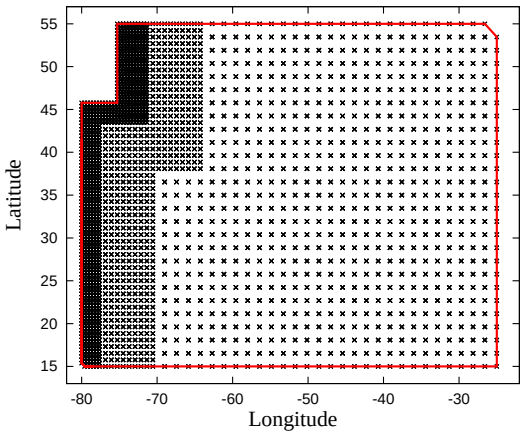

Figure 4.2: Vertices of the grid with two refinement levels used for the idealized coast line test. The red line marks the coast line.

We perform model runs on a triangular grid, which is structured in longitude/latitude space. We use refinement to increase the resolution in the vicinity of the boundary (see Figure 4.2). A grid edge has a length of about 1.6° in the coarsest and 0.4° in the finest part of the grid.

While the meridional wind stress is zero, the zonal wind stress is set to

$$\tau_\lambda^s = \tau_0 \cdot 10^{-3} \cdot \cos\left(\frac{\pi\,(\theta - 15°)}{40°}\right) m^2 s^{-2},$$

where θ is the latitude. The bottom friction coefficient γ_f is set to $10^{-6}\ s^{-1}$. The height field is initialized with a constant water depth of 1000 m; the initial velocity is set to zero.

Figure 4.3 shows the equilibrated steady velocity field for $\tau_0 = 0.84$, $\nu = 3000.0\ m^2 s^{-1}$, and either no-slip, or free-slip boundary conditions in the upper left part of the domain, after one year of integration.

4.3.2 The Atlantic test

We simulate an ocean basin which is shaped like the Atlantic ocean, but the domain is cut at the equator and at 58° North. The real-world topography is cut at 1000 m depth. An artificial wind forcing that is balanced by bottom friction induces a steady circulation. The used numerical grid is plotted in Figure 4.4. The grid is refined at the western boundary and has a typical edge length of 120 km in the coarse, and 60 km in the fine part of the grid. In the refined area along the coast line there are always two neighbored grid edges that are aligned with each other.

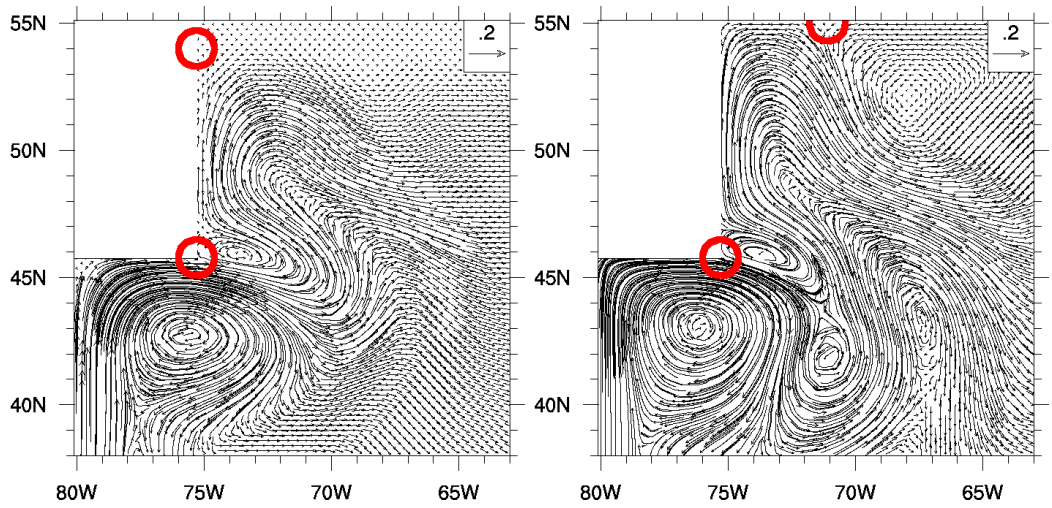

Figure 4.3: Equilibrated velocity field in the upper left part of the idealized coast line test with $\tau_0 = 0.84$, $\nu = 3000.0\ m^2 s^{-1}$, and no-slip (left) or free-slip (right) boundary conditions. The red circles mark separation points we identified by looking at the flow trajectories. In the no-slip run, the northern separation point might appear to be set too far to the north, but the flow trajectories in the direct vicinity of the coast line are separating at this point.

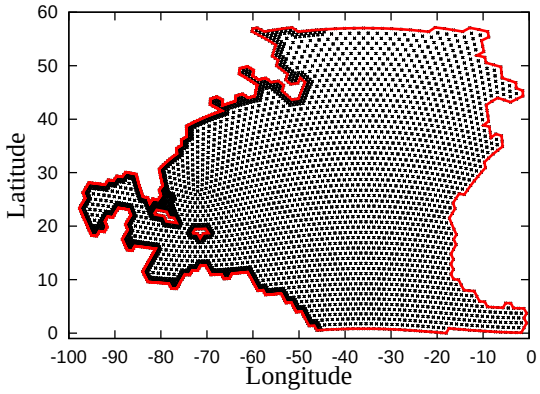

Figure 4.4: Vertices of the refined grid used for the Atlantic test. The red line marks the coast line.

Simulations are initialized with zero surface elevation and zero velocity. The zonal wind forcing is given by

$$\tau_\lambda^s = \begin{cases} -\tau_0 \cdot 10^{-3} \cdot \cos(4 \cdot \theta) & \text{if} \quad \theta < 45° \quad \text{in} \quad m^2 s^{-2} \\ 0 & \text{if} \quad \theta \geq 45°, \end{cases}$$

the meridional wind forcing is zero. The bottom friction coefficient γ_f is set to $10^{-6}\ s^{-1}$.

Figure 4.5 shows the equilibrated steady velocity field for model simulations with $\tau_0 = 3$, $\nu = 6655.0\ m^2 s^{-1}$, and no-slip or free-slip boundary conditions. An identification of separation points along the boundary, by locking at the flow trajectories, is difficult. Many points are questionable, since a clear definition of boundary separation point in ocean currents is missing.

Although there is a clear Gulf stream type flow separating from the coast, there are flow trajectories all along this part of the coast, which follow the boundary very closely. A clear Gulf stream type separation point is not visible, neither for no-slip, nor for free-slip boundary conditions. Therefore, the most important boundary separation point, the separation point of the Gulf stream, will probably not be detectable by evaluating the kinematics along the coast line.

4.3.3 The island test

We study a geostrophic flow around an island. We simulate a global, zonal jet similar to the one in the steady-state zonal geostrophic flow test proposed in Williamson et al. (1992) (test case 2 with $\alpha = 0$), and introduce a small island into the northern hemisphere. The physical fields are initialized as follows

$$u = u_0 \cos(\theta), \quad v = 0, \quad \text{and} \quad h = h_0 - \left(a_e \Omega u_0 + \frac{u_0^2}{2} \right) \frac{\sin(\theta)^2}{g},$$

where θ is the latitude, a_e is the radius of the earth, Ω is the earth rotation rate, u is the zonal velocity, v is the meridional velocity, and g is the gravitational acceleration. We choose $u_0 = 2.83\ ms^{-1}$, and $h_0 = 500\ m$.

The island has a diameter of 110 km and is centered around 45° North and 0° West. Since we simulate the whole globe, although we are only interested in the flow around the small island, we refine our numerical grid extensively. We start from a coarse icosahedral grid with an averaged edge length of 960 km, and introduce seven refinement levels, where each level reduces the lattice spacing by a factor of two. A typical edge length at the boundary of the island is 7.5 km. The island is cut out of the grid by removing all grid points in a specific distance to the center of the island. The grid is illustrated in Figure 4.6.

The Reynolds number of the flow around the island is given by

$$Re = \frac{UD}{\nu},$$

where D is the diameter of the island, ν is the viscosity, and U is a typical value for velocity, which is $2\ ms^{-1}$ in the vicinity of the island.

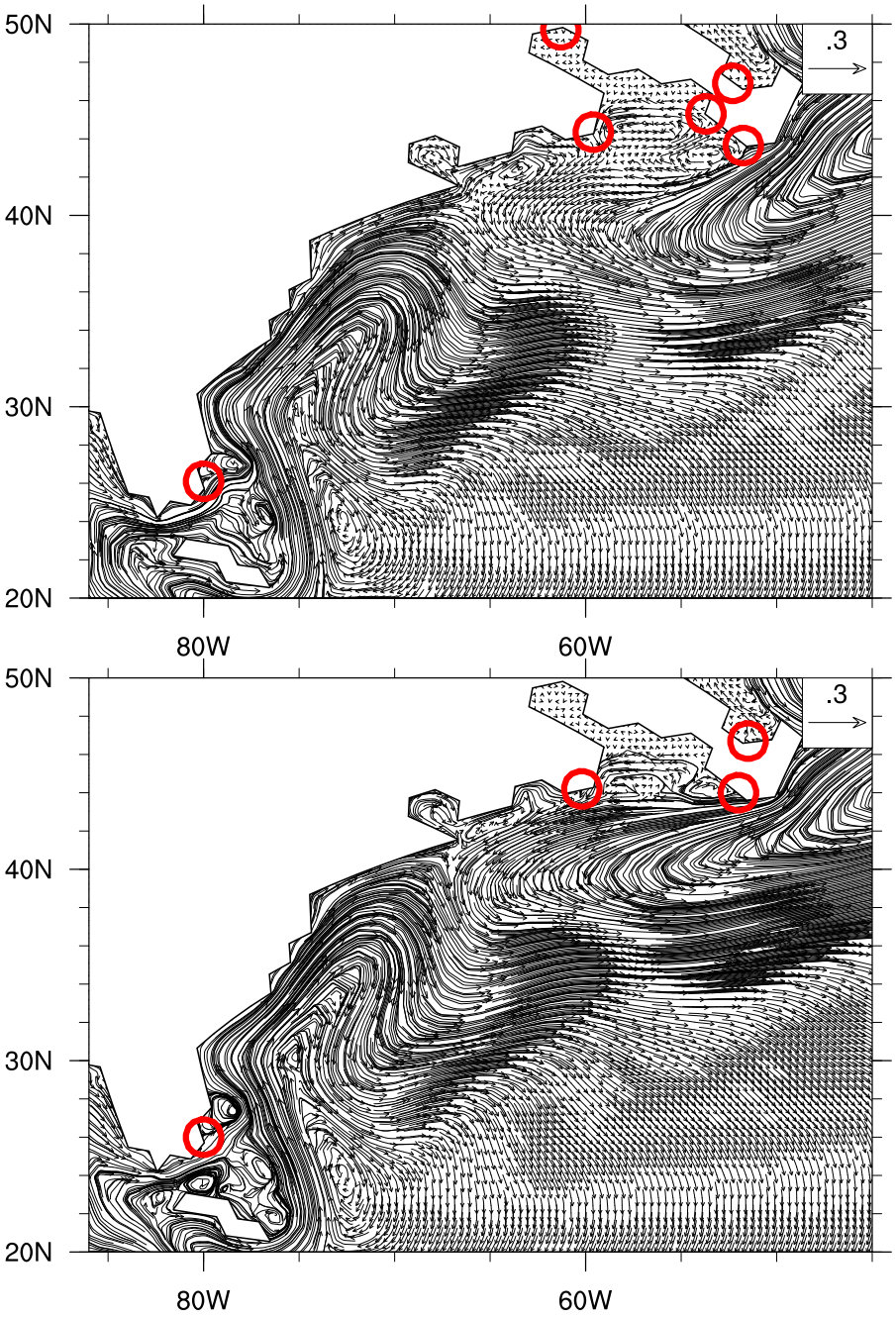

Figure 4.5: Equilibrated velocity field at the east coast of North America for the Atlantic test with $\tau_0 = 3$, $\nu = 6655.0\ m^2 s^{-1}$, and no-slip (top) or free-slip (bottom) boundary conditions. The red circles mark separation points along the North American coast we identified by looking at the flow trajectories.

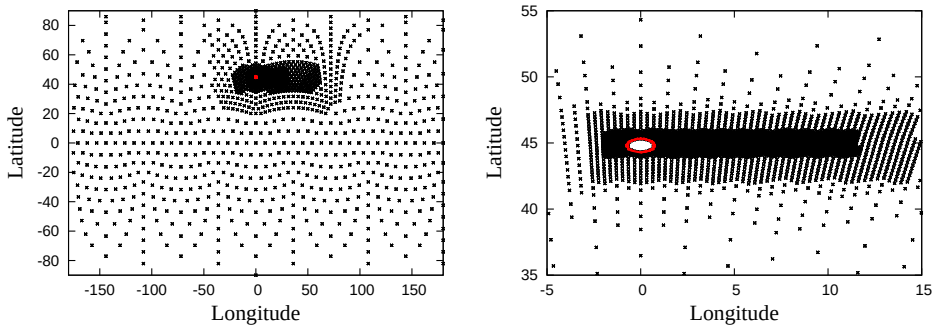

Figure 4.6: Vertices in the grid used for the geostrophic flow around an island test. The whole grid (left), and a zoom into the area around the island (right). The red line marks the coast line.

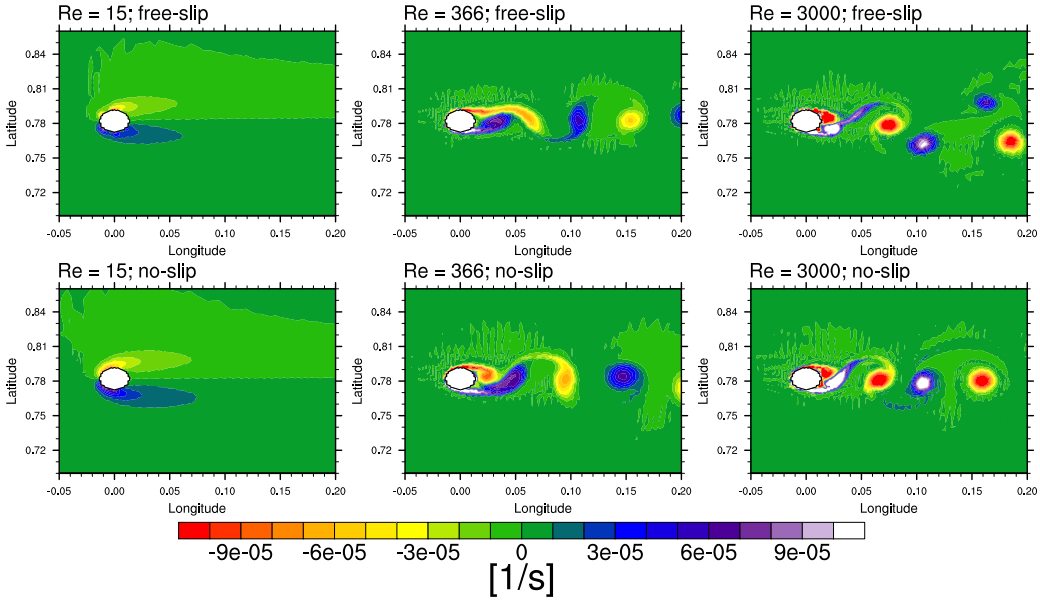

Figure 4.7: Vorticity field of the island test for $Re = 15$, $Re = 366$, and $Re = 3000$ (from left to right) for free-slip (first row), and no-slip (second row) boundary conditions after 50 days.

To study different flow regimes, we perform model runs with three different values for ν that result in the three Reynolds numbers 15, 366 and 3000. Figure 4.7 shows the vorticity fields of the model runs. Our results are similar to the results in Dong et al. (2007), where three dimensional simulations are evaluated. At $Re = 15$ two symmetric steady eddies occur in the lee of the island. At $Re = 366$ vortices detach periodically with a period of about 2.75 days. We obtain a von Kármán vortex street. For $Re = 3000$ we obtain a fully turbulent behavior in the lee of the island.

Index	Boundary condition	τ_0	ν in $\left[m^2 s^{-1}\right]$	Grid
a	no-slip	0.28	3000.0	1 level refined
b	no-slip	0.28	3000.0	2 level refined
c	free-slip	0.28	3000.0	1 level refined
d	free-slip	0.28	3000.0	2 level refined
e	free-slip	0.28	10000.0	no refinement
f	free-slip	0.28	10000.0	2 level refined

Table 4.1: List of the performed model runs for the idealized coast line test.

4.4 Properties of boundary currents in a finite element shallow-water model

In this section, we study the properties of western boundary currents and boundary separation in a finite element shallow-water model. We study the influence of resolution, viscosity, the grid structure, the shape of the coast line, the alignment between the velocity components and the coast line, and no-slip or free-slip boundary conditions in the idealized coast line or the Atlantic test. The results of this section are summarized and discussed in subsection 4.6.1.

4.4.1 The western boundary current in the idealized coast line test

In this subsection we study the representation of steady western boundary currents along idealized coast lines. We evaluate the idealized coast line test introduced in subsection 4.3.1. Table 4.1 lists the properties of the performed model runs. The grid which is indicated as '2 level refined' in Table 4.1, is the grid plotted in Figure 4.2. The '1 level refined' and 'no refinement' grids have the same extend as the '2 level refined' grid, but they do not have the finest, or both refinement levels, respectively.

Figure 4.8 shows the height field of the model runs after one year of integration, when the model is in equilibrium. For all tests, the Munk layer at the western boundary is represented smoothly. The width of the Munk layer is dependent on eddy viscosity. If eddy viscosity is too low, the boundary current is not properly resolved (Griffies 2004).

We would not expect separation to occur when free-slip boundary conditions are used, since Dengg (1993) did not obtain separation with a numerical model based on the barotropic vorticity equation. Nevertheless, the boundary flow separates for free-slip and no-slip boundary conditions. The model results look fairly different for the two boundary conditions (compare b and d). Resolution does not play an important role for boundary separation (compare a with b, c with d, and e with f). For different values of eddy viscosity, the model results look fairly different (compare d and f).

Dengg (1993) studied a further test, in which he simulated a similar test setup as

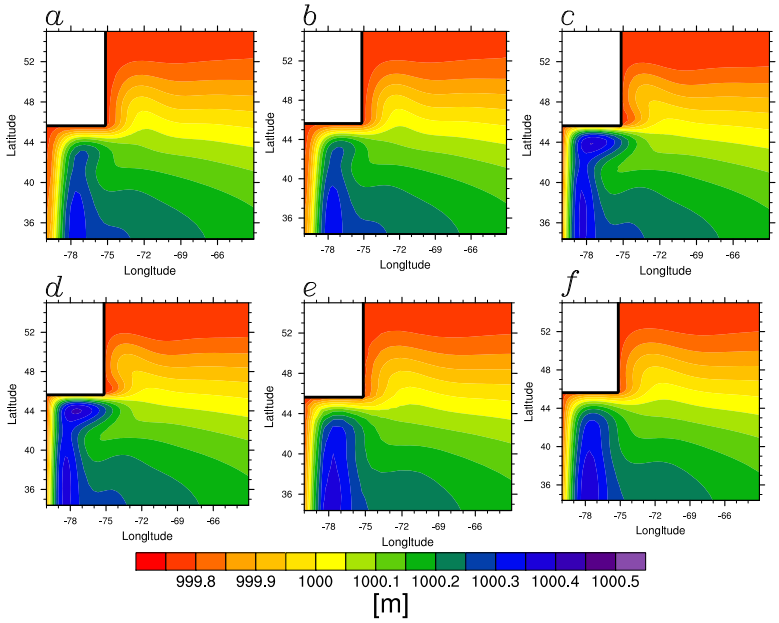

Figure 4.8: Equilibrium height field of the idealized coast line model runs listed in Table 4.1, after one year.

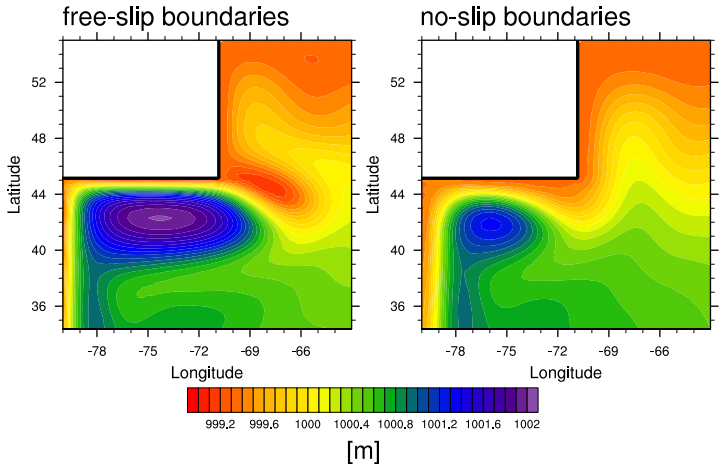

Figure 4.9: Equilibrium height field of idealized coast line model runs with a larger obstacle for free-slip (left) and no-slip (right) boundary conditions, with $\nu = 3000\ m^2 s^{-1}$, $\tau_0 = 0.84$, and '1 level' refinement.

before, with a larger obstacle. In these simulations, he noticed premature separation for no-slip, but not for free-slip boundary conditions. Premature separation means that the flow is not able to follow the northern coast line for a long distance, and separates earlier. Figure 4.9 shows the equilibrium height field of model runs of the

finite element model, performed with a larger obstacle, compared to the previous runs. As in Dengg (1993), we notice premature separation for no-slip, but not for free-slip boundary conditions. For the no-slip case, the radius of the circular separation cell and the distance of the separation point from the western boundary can be approximated by the inertial length scale δ_I, as in Dengg (1993). δ_I is given by

$$\delta_I = \left(\frac{U}{\beta}\right)^{1/2},$$

where β is the change of the Coriolis parameter with latitude. For the test case in Figure 4.9 we obtain: $\delta_I \approx 3.1°$. This is in good agreement with the numerical results.

We have performed double gyre simulations similar to the simulations in Haidvogel et al. (1992) (not shown in this paper). These simulations confirm that premature separation takes place for no-slip, but not for free-slip boundary conditions.

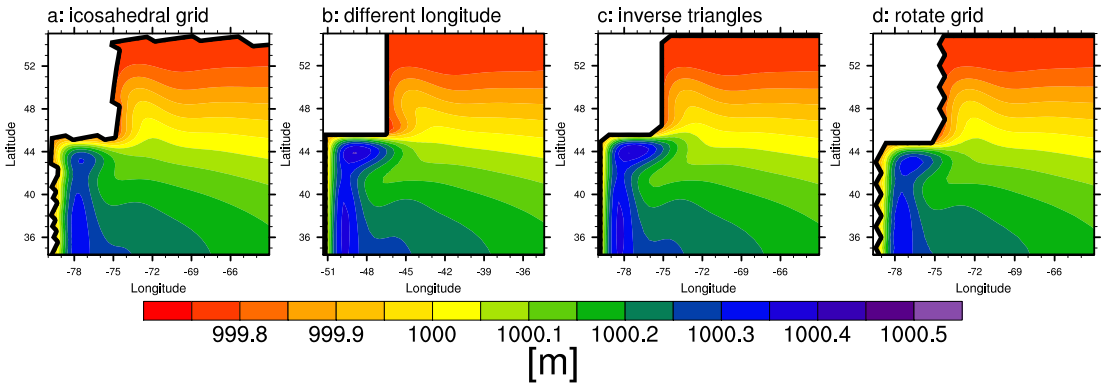

Figure 4.10: Equilibrium height field of the idealized coast line model runs with free-slip boundaries conditions on different grids. Results can be compared with model run *c* in Figure 4.8.

Figure 4.10 shows the same idealized coast line run as model run *c* in Figure 4.8 ($\nu = 3000\ m^2 s^{-1}$, $\tau_0 = 0.28$), on the different grids sketched in Figure 4.11 and 4.12. Simulation a is performed on a one level refined icosahedral grid. The coast line is represented by an unstructured pattern. In model run b, we change the longitude of the model domain compared to the standard grid. This changes the alignment of the two components of the velocity field u and v, compared to the coast line. In the model runs c and d, we change the arrangement of the triangles in the structured grid (Figure 4.12). We study a zig-zag coast line on the western boundary in model run d.

While the change of the longitude (model run b) does not make a visible difference compared to model run *c* in Figure 4.8, we get differences for all other cases. Results for the model runs a and d, in which the meridional coast is represented by an unstructured or a zig-zag coast line, are fairly similar to the no-slip run *a* in Figure 4.8. This appears

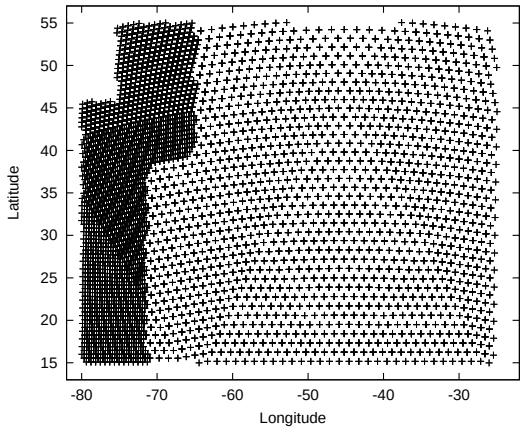

Figure 4.11: Vertices of the refined grid built from an icosahedral grid, used in model run a in Figure 4.10.

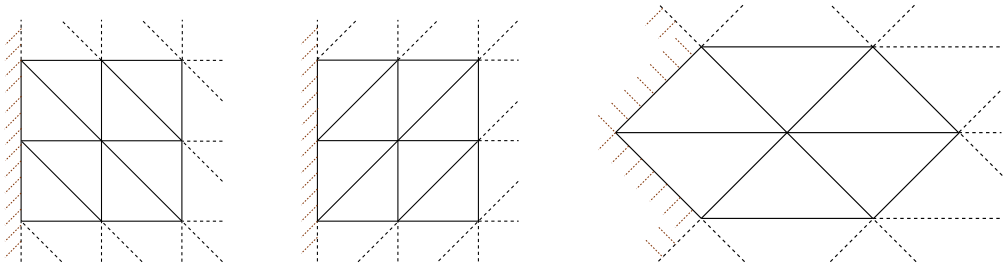

Figure 4.12: Structure of the triangular grids used for the standard runs (left), and run c and d in Figure 4.10 (middle and right), with indicated coast line at the western boundary.

to be analog to problems known for finite difference methods, where the character of the boundary conditions on a zig-zag coast line can effectively change from free-slip into no-slip boundary conditions (see Adcroft and Marshall 1998, for an Arakawa C-grid), but the mechanism of the change in finite element methods is fairly different. The boundary conditions at the coast do not change with the alignment of the grid, as for the finite difference methods. Otherwise there would be changes in run b, as well. In fact, the boundary flow is shifted slightly into the interior of the domain due to the abrupt changes of the direction of the coast line. The solution gets closer to the no-slip case, in which a small distance of the boundary flow to the coast line is induced by the boundary conditions.

The separation behavior at the obstacle in simulation c in Figure 4.10 is fairly different to the reference run. The flow is not even clearly separating. The change of the grid structure leads to a slight change of the coast line. It is alarming that the triangle

Index	Boundary condition	τ_0	ν in $\left[m^2 s^{-1}\right]$	Refinement
a	free-slip	3.0	6655.0	yes
b	no-slip	3.0	6655.0	yes
c	free-slip	3.0	53240.0	yes
d	free-slip	3.0	53240.0	no

Table 4.2: List of the performed model runs for the Atlantic test.

pattern at the boundary has such a severe influence on the separation behavior, since these kind of changes will also appear, when the same ocean model is discretized on two slightly different grids.

4.4.2 The western boundary current in the Atlantic test

In this subsection we study the representation of steady western boundary currents along a coast line as used in ocean models. We evaluate the Atlantic test introduced in subsection 4.3.2. Table 4.2 lists the properties of the four model runs from which the height field is displayed in Figure 4.13. As mentioned in the previous subsection, the eddy viscosity fixes the width of the Munk layer (Griffies 2004). A viscosity significantly lower than 6655 $m^2 s^{-1}$ for the refined, and 53240 $m^2 s^{-1}$ for the unrefined model run, would lead to an insufficiently resolved Munk layer, which would trigger model instabilities.

The model runs a, b, and c are performed on the grid plotted in Figure 4.4. Model run d is using the same grid without refinement of the western boundary. The height field along the western boundary differs much more for different values of eddy viscosity (compare a with c) than for no-slip and free-slip boundary conditions (compare a and b). A change in resolution leads to minor changes (compare c and d), although it limits the smallest possible value for eddy viscosity.

4.5 Criteria to detect boundary separation points

In this section we try to identify proper criteria to detect flow separation points in a finite element shallow-water model, for no-slip and free-slip boundary conditions. We study five approaches ($\mathbb{A}$ - $\mathbb{E}$) to detect boundary separation points. The approaches evaluate different physical quantities along the boundary. To derive criteria to detect separation points for the different approaches, we study the properties of the physical quantities in the vicinity of a separation point, and evaluate theories on boundary separation from the literature.

We test the criteria in model runs of the three test cases introduced in section 4.3. Since a clear definition of separation points is missing, it is difficult to find reference

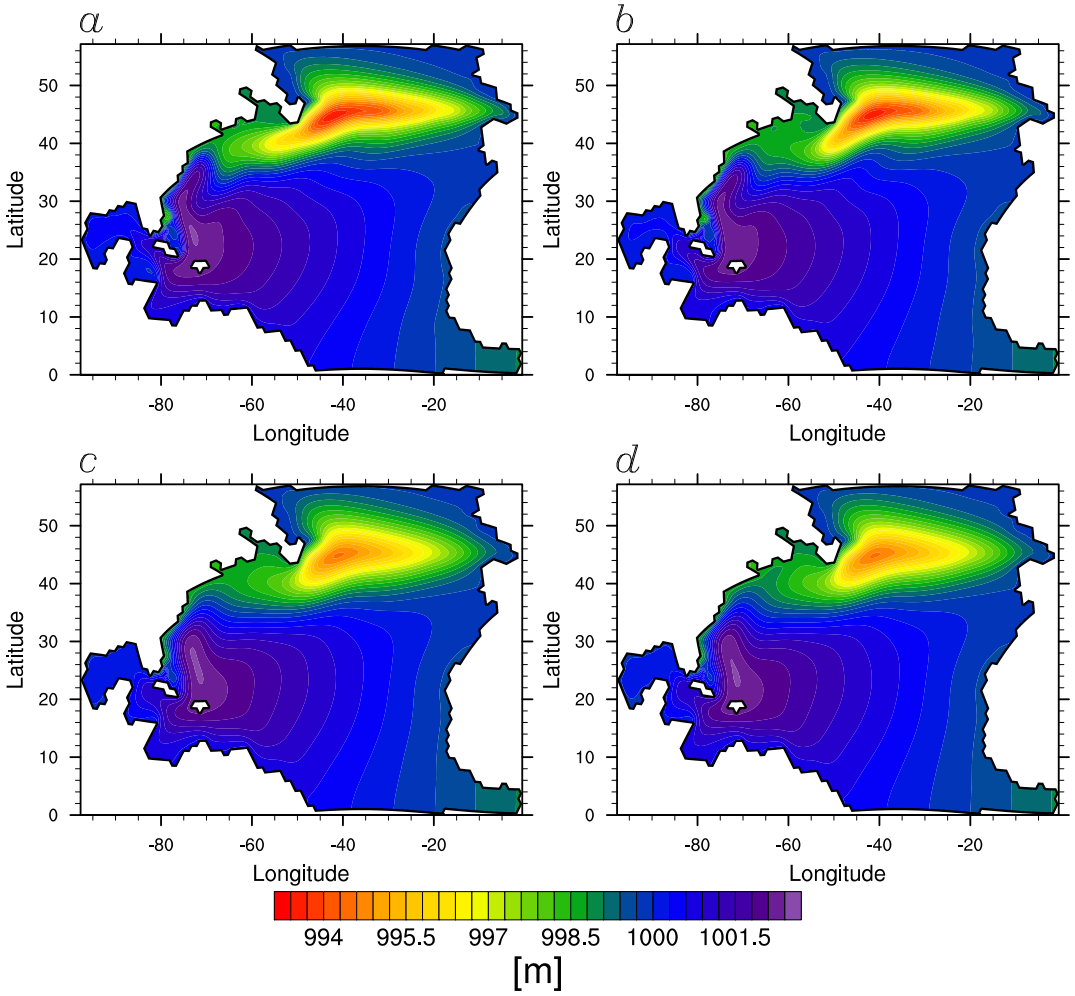

Figure 4.13: Equilibrium height field in the Atlantic model runs listed in Table 4.2, after 140 days.

solutions to compare the results of a possible criterion for flow separation points with a 'truth'. For the steady idealized coast line and the Atlantic test, we compare the results for a separation criteria to the separation points identified by looking at the flow trajectories (Figure 4.3 and 4.5). For the unsteady island test, it is very difficult to decide which points we shall count as separation points by looking at the flow trajectories. Therefore, we can not give a reference solution. Still, for most of the evaluated separation criteria it is fairly obvious from the flow fields whether a criterion provides good results or not.

This section starts with a discussion of the flow properties at an idealized flow separation point and a short overview over the five approaches (subsection 4.5.1). The different approaches are evaluated in the following subsections. The results of this

section are discussed in subsection 4.6.2.

4.5.1 The properties of an idealized separation point

Figure 4.14 sketches an idealized flow separation from a boundary on the northern hemisphere. x is the zonal coordinate in space, y is the meridional coordinate in space, u is the zonal, and v is the meridional velocity. The boundary aligns with the meridional direction at $x = 0$. A northward current from the south meets a southward current from the north. The currents merge and separate from the boundary into the domain. We assume the separation point P(0,γ) to be fixed. The analysis of such an idealized sketch will not be able to provide sufficient conditions for separation, but properties of the sketched flow separation point might serve as necessary conditions for general separation points.

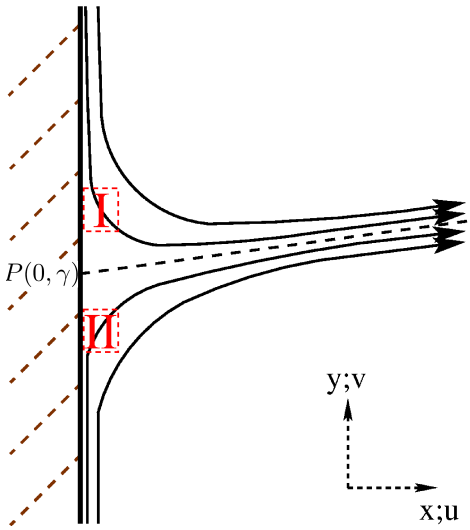

Figure 4.14: Sketch of an idealized, fixed separation point from a meridional boundary. $P(0,\gamma)$ marks the separation point. The properties of the the sketched flow at the two distinct areas I and II are listed in Table 4.3.

Table 4.3 lists a number of properties of the flow in the two areas I and II in the separation sketch, which we gathered by simple reasoning. In Figure 4.14, it is visible that the zonal velocity is greater than zero in the direct vicinity of the coast and increases in the zonal direction (line 1 and 4 of Table 4.3). In the meridional direction, the zonal velocity increases towards the separation point (line 5). While the meridional velocity is greater than zero south of the separation point, it is smaller than zero north of the separation point (line 2). This can be combined with the fact that the meridional velocity is zero on the boundary for no-slip boundary conditions (line 6; in the direct vicinity of the boundary). For free-slip boundary conditions, it is known that the

	Quantity	I	II
1	u	> 0	> 0
2	v	< 0	> 0
3	v/u	< 0	> 0
4	$\partial_x u$	> 0	> 0
5	$\partial_y u$	< 0	> 0
6	no-slip: $\partial_x v$	< 0	> 0
7	free-slip: $\partial_x v$	> 0	< 0
8	$\partial_y v$	< 0	< 0
9	$\omega = \partial_x v - \partial_y u$	> 0	< 0
10	$\partial_x h$	< 0	> 0

Table 4.3: Expected properties of the flow field for the two areas I and II indicated in Figure 4.14.

Approach	Evaluated quantities	Evaluated literature for no-slip boundaries	Evaluated literature for free-slip boundaries
$\mathbb{A}$	$\partial_x v$ and $\partial_{xy} v$	Prandtl (1904) and Haller (2004)	
$\mathbb{B}$	ω	Ghil et al. (2004)	
$\mathbb{C}$	$\partial_x u$ and $\partial_y v$		Lekien and Haller (2008)
$\mathbb{D}$	v/u		
$\mathbb{E}$	$\partial_x h$ and $\partial_y h$	Haidvogel et al. (1992)	Haidvogel et al. (1992)

Table 4.4: List of the evaluated approaches to detect separation points. The quantities are presented for separation points in which the tangential at the coast line is aligned with the meridional coordinate axis (as in Figure 4.14).

western boundary current is intensified towards the western boundary and reaches its maximum absolute velocity in the direct vicinity of the coast, at least if idealized coast lines are considered (line 7). The absolute meridional velocity decreases towards the separation point (line 8). The flow rotates clockwise in area II and anti-clockwise in area I, which indicates a negative and positive vorticity (line 9). We can assume geostrophic balance to be a good approximation within the domain, and we know that clockwise gyres show a positive, and anti-clockwise gyres show a negative height anomaly for the shallow-water system on the northern hemisphere. The anomalies should level out towards the coast (line 10).

Table 4.4 lists the physical quantities and the most important publications that are evaluated in the five approaches to detect flow separation points. All approaches are

studied on no-slip and free-slip boundaries. If no literature is given in Table 4.4 for a given boundary condition, the evaluated criteria are motivated within this paper. Some of the criteria are used beyond their theoretical limits. For example, when we use a criterion developed for steady flows to detect separation points in unsteady flows, or when we use a criterion derived for incompressible fluids to detect separation points in the compressible shallow-water setup. We want to improve our understanding of the behavior of the physical quantities around the separation point, and to elaborate working methods to detect separation points in general flow fields in finite element models for ocean applications. It is possible that a criteria provides good results to detect separation points, when it is applied to flow fields that are not captured by the theoretical derivation.

4.5.2 Approach $\mathbb{A}$: Evaluating the change of the tangential velocity in the normal direction following Prandtl (1904) and Haller (2004)

In this subsection, we evaluate the change of the tangential velocity in the normal direction. We start with the analysis of the theories for flow separation on no-slip boundaries by Prandtl and Haller. Afterwards, we motivate and evaluate two criteria for flow separation on free-slip boundaries.

In 1904 Prandtl developed a theory for flow separation of steady flows on **no-slip** boundaries (Prandtl 1904). Following Prandtl, separation occurs at a boundary aligned with the y coordinate at a point $P(0, \gamma)$, when

$$\nu\rho\partial_x v(0,\gamma) = 0, \qquad \text{and} \qquad \nu\rho\partial_{xy} v(0,\gamma) < 0, \tag{4.1}$$

where $v(x, y)$ is the meridional velocity, ν is the kinetic viscosity, and ρ is the density of the fluid. The first condition is a necessary condition that states that the wall shear vanishes, the second condition is a sufficient condition that states that the wall shear admits a negative gradient. Unfortunately, Prandtls theory does not hold for unsteady flows (Sears and Tellionis 1975).

In this paper we study boundary separation in a numerical model with curved coast lines. Since ν and ρ are positive and greater than zero, we define the two criteria for separation points, based on the theory by Prandtl, to be

$$\lambda_{1,n} = \mathbf{n} \cdot [(\nabla \mathbf{u}) \cdot \mathbf{t}] = 0, \qquad \text{and} \qquad \lambda_{1,s} = \partial_{\mathbf{t}} \left(\mathbf{n} \cdot [(\nabla \mathbf{u}) \cdot \mathbf{t}]\right) < 0, \tag{4.2}$$

where $\mathbf{t}$ is the tangential, and $\mathbf{n}$ is the normal unit vector in respect to the boundary. $\partial_{\mathbf{t}}$ denotes the spatial derivative in the tangential direction, not the time derivative ∂_t.

Another theory for flow separation on no-slip boundaries that evaluates the change of the tangential velocity in the normal direction, is the theory developed by Haller

(Haller 2004). The theory offers separation criteria for unsteady but fixed flow separation in general two dimensional velocity fields. Separation is investigated with a dynamical systems approach. The flow trajectory at the separation point is assumed to be non-hyperbolic. Haller combines this assumption with the continuity equation at the boundary. The theory provides necessary and sufficient conditions for flow separation, and high-order approximations for unsteady separation profiles in the vicinity of the boundary.

For a boundary aligned with the y-coordinate ($x = 0$), a necessary condition for a so-called effective separation point $y = \gamma_{\text{eff}}$ at a given time t_0 is

$$\int_{t_0}^{t} \frac{\partial_x v(0, \gamma_{\text{eff}}, \tau)}{\rho(0, \gamma_{\text{eff}}, \tau)} d\tau = 0, \tag{4.3}$$

where we integrate backward in time ($t < t_0$). The effective separation point will converge to the real separation point γ for $t \to -\infty$

$$\gamma = \lim_{t \to -\infty} \gamma_{\text{eff}}(t, t_0). \tag{4.4}$$

To derive the criterion, Haller assumed that the density and the time integrated second derivative $\partial_{xy} u$ remain bounded. Both assumptions are valid for our shallow-water model (where the density is replaced by the water depth). For zero integration time, the necessary criterion by Haller is equivalent to the necessary condition by Prandtl (equation (4.1)), since viscosity and density are always positive and greater than zero.

A sufficient condition, which is also derived in Haller (2004), is

$$\lim_{t \to -\infty} \int_{t_0}^{t} \left[\frac{\partial_{yx} v(0, \gamma, \tau) - \partial_{xx} u(0, \gamma, \tau)}{\rho(0, \gamma, \tau)} - 2\partial_{yx} u(0, \gamma, \tau) \int_{t_0}^{\tau} \frac{\partial_x v(0, \gamma, s)}{\rho(0, \gamma, s)} ds \right] d\tau = \infty. \tag{4.5}$$

It can be shown that this criterion reduces to the sufficient criterion by Prandtl when applied to steady flows (Haller 2004). For velocity, second order derivatives in space are critical quantities in the used low-order finite element model, since they need to be reconstructed with neighboring cells, or with the fluxes through the cell boundaries. The two combined time integrations make it very complicated to calculate the sufficient condition. Furthermore, it is difficult to analyze equation (4.5), since infinite values will not be reached, when model runs are evaluated. For these reasons, we solely use the necessary condition, and evaluate points we call 'possible separation points', since these points are not verified by a sufficient condition.

To obtain an applicable separation criterion based on the theory by Haller, for flow separation in a shallow-water model with realistic coast lines, we replace the fluid density in equation (4.3) with the water depth, and modify the criterion to be

$$\lambda_2 = \limsup_{t \to -\infty} \int_{t_0}^{t} \frac{\mathbf{n} \cdot [(\nabla \mathbf{u}\,(x, y, \tau)) \cdot \mathbf{t}]}{H} d\tau = 0. \tag{4.6}$$

It is obvious that the results for λ_2 will depend on the integration time t, for unsteady separation.

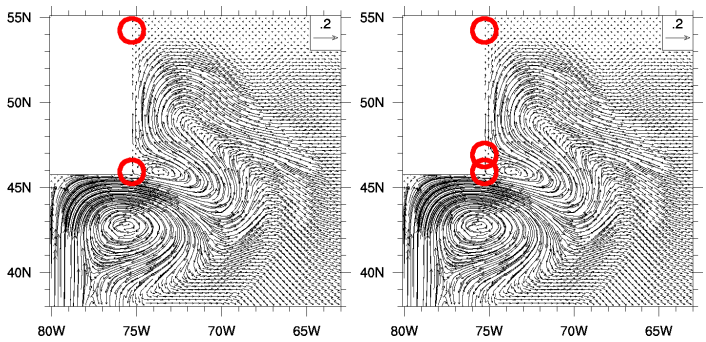

Figure 4.15: Separation points detected with the theory by Prandtl (left) and Haller (right) for the no-slip run of the idealized coast line test. The separation criterion from Haller was integrated over 26 days.

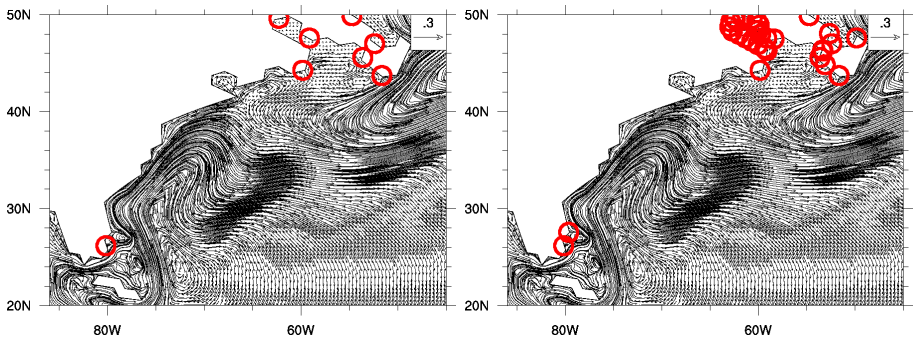

Figure 4.16: Separation points detected with the theory by Prandtl (left) and Haller (right) for the no-slip run of the Atlantic test. The separation criterion from Haller was integrated over 24 days.

Figure 4.15 and 4.16 show the results for the detection of separation points in steady flows on no-slip boundaries, by applying the criteria derived through Prandtl's and Haller's theories. Both criteria are able to detect the separation points (compare with

Figure 4.3 and 4.5). Haller's criterion also detects reattachment points, since the sufficient condition is not evaluated.

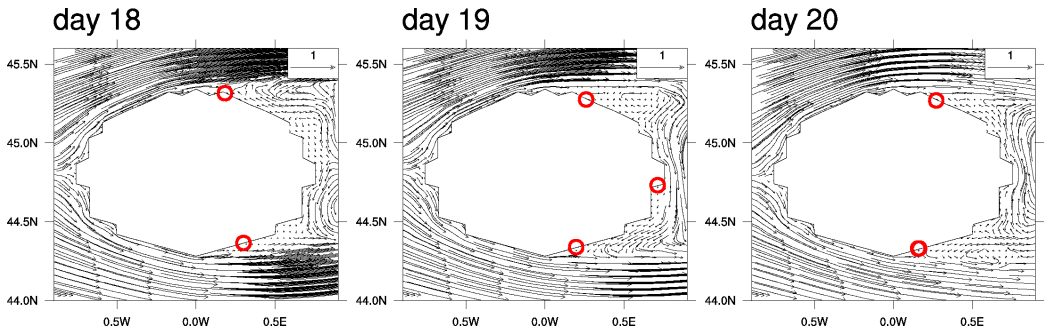

Figure 4.17: Separation points detected with the theory by Prandtl for the no-slip run of the island test with $Re = 366$, for three time steps.

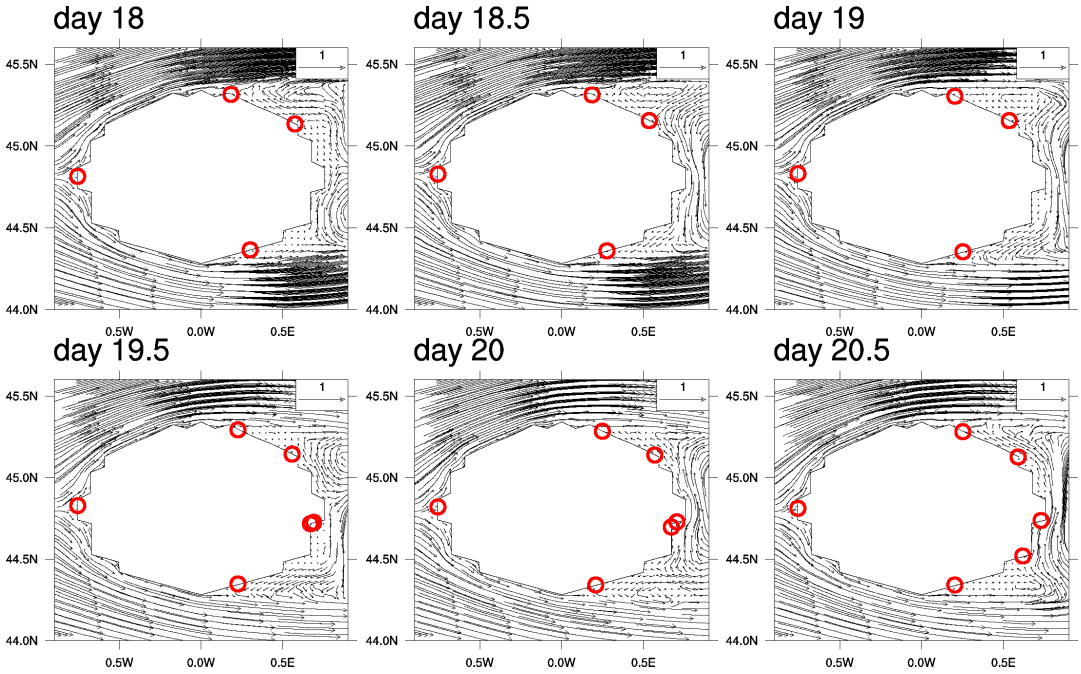

Figure 4.18: Separation points detected with the theory by Haller for the no-slip run of the island test with $Re = 366$, for different time steps. The time integrations for the separation criterion start at day 18.

The Figures 4.17 and 4.18 show the results for the criteria derived through Prandtl's and Haller's theory for separation points in the unsteady island test with $Re = 366$ and no-slip boundaries. The Prandtl criteria give reasonable results for the separation points. To investigate the influence of the time integration time t on the necessary

criterion from Haller, we plotted several time steps with increasing t. The flow field changes faster, than the criterion by Haller is adjusting. The criterion has problems for moving, unsteady separation.

For **free-slip** boundaries we expect the necessary condition of Prandtl (first equation of (4.1)) to be a good indicator for separation. As listed in Table 4.3 the change of the sign of $\partial_x v$ is also apparent for free-slip conditions, at least for the idealized flow field in Figure 4.14. Since the change of the sign has the opposite direction, we do not use the sufficient condition of Prandtl, and only evaluate the necessary condition. We test the criterion

$$\lambda_3 = \mathbf{n} \cdot [(\nabla \mathbf{u}) \cdot \mathbf{t}] = 0, \tag{4.7}$$

to detect flow separation points on free-slip boundaries.

In the following, we motivate a second criterion for separation from free-slip boundaries, which is similar to the one by Haller (equation (4.3)). The derivation of Hallers theory is not applicable to free-slip boundary conditions, since the flow trajectory at the separation point is hyperbolic and not non-hyperbolic (Lekien and Haller 2008). The coast line forms the two stable trajectories of this hyperbolic trajectory. For free-slip boundaries, we can expect the flow along the coast line in Figure 4.14 to approach but not cross the idealized separation point. The sign of the change of the meridional velocity will stay as it is listed in Table 4.3 on each side of the separation point. The sign changes at the separation point. We therefore evaluate the following criterion for possible separation points

$$\lambda_4 = \limsup_{t \to -\infty} \int_{t_0}^{t} \left[\frac{\mathbf{n} \cdot [(\nabla \mathbf{u}\,(x, y, \tau)) \cdot \mathbf{t}]}{H} \right]_{\mathbf{x}} d\tau = 0. \tag{4.8}$$

In contrast to the no-slip criterion based on the theory by Haller (equation (4.6)), particles in the direct vicinity of the coast will be advected with the flow. The lowered $\mathbf{x}$ in equation (4.8) indicates that we integrate along a flow trajectory $\mathbf{x}\,(t)$, and follow an imaginary particle in the flow field along the coast line. The criterion is not founded on mathematical sound Lyapunov type coefficients.

Since we can not expect criteria (4.7) and (4.8) to be sufficient conditions for flow separation, we can only evaluate possible separation points. Figure 4.19 shows possible separation points detected with the criteria (4.7) and (4.8) for the idealized coast line test with free-slip boundaries. Criterion (4.7) detects the separation point at the obstacle, but fails to detect the separation point on the northern coast (compare to Figure 4.3). Criterion (4.8) does it the other way around. For the idealized coast line test criterion (4.8) faces a post processing problem. We started the time integration for a

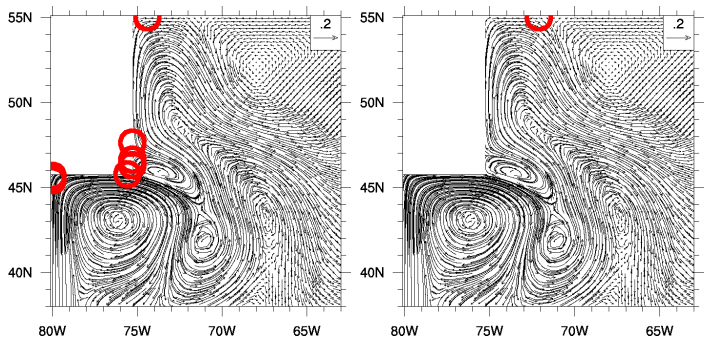

Figure 4.19: Separation points detected with criterion (4.7) (left) and (4.8) (right) for the free-slip run of the idealized coast line test. Criterion (4.8) was integrated over 100 days.

number of test particles distributed equidistantly along the coast. After short time, the flow has depopulated large parts of the coast line, and gathered the particles at very few locations. A change in the sign of λ_4 is not detectable anymore, for the separation at the obstacle.

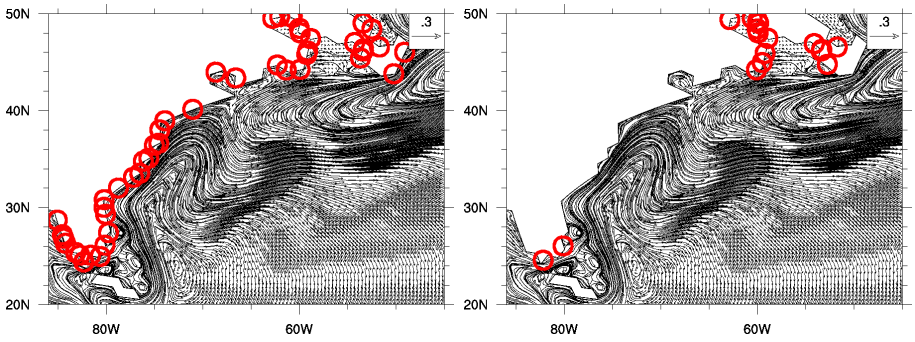

Figure 4.20: Separation points detected with criterion (4.7) (left) and (4.8) (right) for the free-slip run of the Atlantic test. Criterion (4.8) was integrated over 73 days.

Figure 4.20 shows the possible separation points for the steady separation in the free-slip Atlantic test detected with the criteria (4.7) and (4.8). While criterion (4.7) is disturbed by the curved coast line, criterion (4.8) detects the separation points fairly well (compare to Figure 4.5).

Figure 4.21 shows the detected possible separation points with criterion (4.8) for the unsteady island test with $Re = 366$ and free-slip boundaries. To investigate the influence of the time integration time t, we plotted several time steps with increasing t. Criterion (4.8) adjusts better to the varying flow field than the criterion from the theory of Haller on no-slip boundaries, since the particles can follow the moving separation points. Still, the results are improvable.

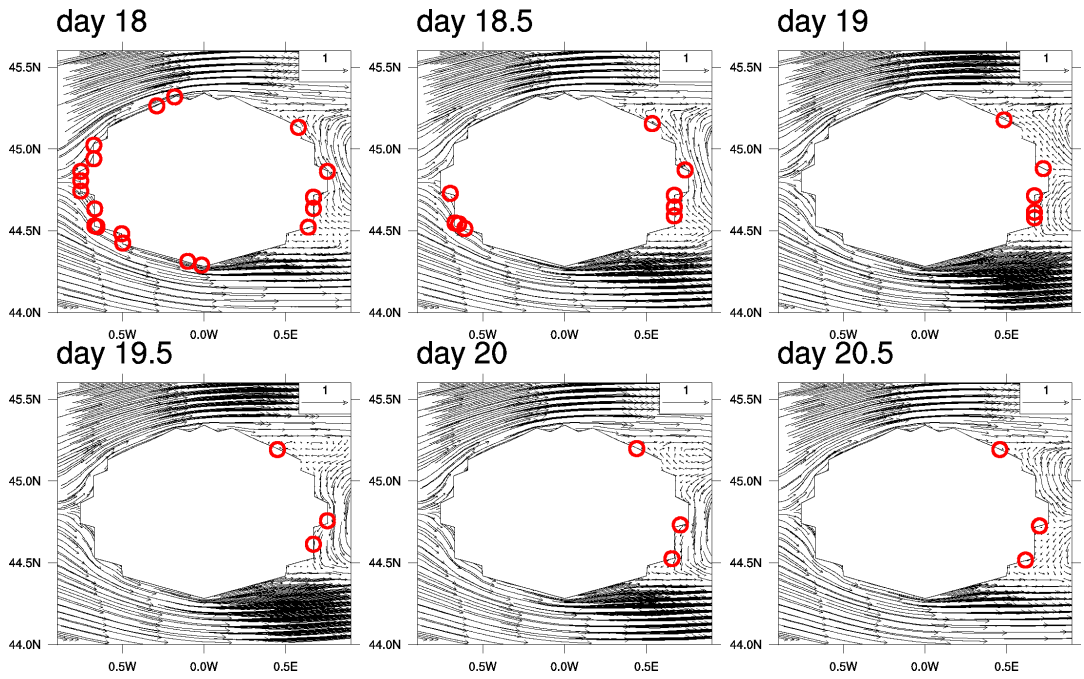

Figure 4.21: Separation points detected with criterion (4.8) for the free-slip run of the island test with $Re = 366$, for different time steps. The time integrations for criterion (4.8) start at day 18.

Summary of the results for Approach $\mathbb{A}$

For **no-slip** boundary conditions, we evaluate the theories for flow separation of Prandtl (Prandtl 1904) and Haller (Haller 2004). The theory of Prandtl should be valid for steady flow fields and no-slip boundary conditions. Our results show that Prandtls criteria for flow separation allow a proper detection of separation points in steady and unsteady flows. The theory by Haller was derived for no-slip boundaries, and unsteady, but fixed separation points. We only evaluate Hallers necessary criterion for flow separation, since the sufficient criterion is very difficult to analyze in the used low-order finite element model. The necessary criterion can not differentiate between separation and reattachment points. Results are very good for steady flow fields, but the criterion has difficulties to identify separation points for unsteady flows with moving separation points.

We motivate why the necessary separation criterion by Prandtl should also be an indicator for flow separation on **free-slip** boundaries. Unfortunately, the criterion is not useful, since it detects to many separation points, where no separation is visible. We derive an additional possible criterion for boundary separation on free-slip boundaries, which is time integrated along flow trajectories that follow the coast line. The criterion

is similar to the necessary criterion from Hallers theory. The criterion provides good results, but the results are dependent on the used integration time. If the integration time is too small, too many possible separation points are detected. If the integration time is too large, separation points can be missed because parts of the boundary are depopulated of the diagnosing particles that move along the coast line.

4.5.3 Approach $\mathbb{B}$: Evaluating the vorticity following Ghil et al. (2004)

In this subsection, we evaluate vorticity. We test the criterion of zero vorticity, to detect separation points on no-slip and free-slip boundaries, and evaluate the theory for bifurcation points by Ghil, Ma, and Wang for no-slip boundaries.

As indicated in Table 4.3, the vorticity changes its sign at the idealized separation point sketched in Figure 4.14. While a zero point of vorticity might be a necessary condition for separation, it is obviously not a sufficient condition, since a constant flow along an idealized coast line already provides zero vorticity. Since we want to study realistic coast lines for ocean models, we calculate the vorticity as the change of the velocity components in tangential or normal direction in respect to the grid edges of the boundary, and evaluate the following criterion for possible separation points

$$\lambda_5 = \omega = \mathbf{n} \cdot [(\nabla \mathbf{u}) \cdot \mathbf{t}] - \mathbf{t} \cdot [(\nabla \mathbf{u}) \cdot \mathbf{n}] = 0.$$

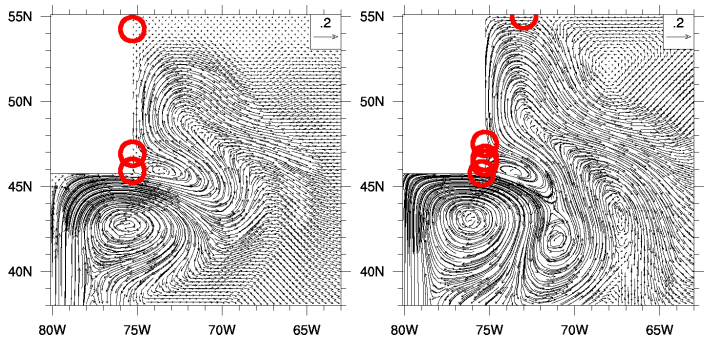

Figure 4.22: Separation points detected with zero points of ω for the no-slip (left) and the free-slip run (right) of the idealized coast line test.

Figure 4.22 and 4.23 show the results for points of zero vorticity along the coast line, for the tests with steady flows on **no-slip** and **free-slip** boundaries. Zero vorticity seems to be a good indicator for separation and reattachment for no-slip, but not for free-slip boundary conditions. For free-slip boundary conditions, too many points are detected. Figure 4.24 shows the results for the unsteady island test and no-slip boundary conditions. Since a sufficient condition is missing, the method detects separation and reattachment points. Again, the criterion provides good results.

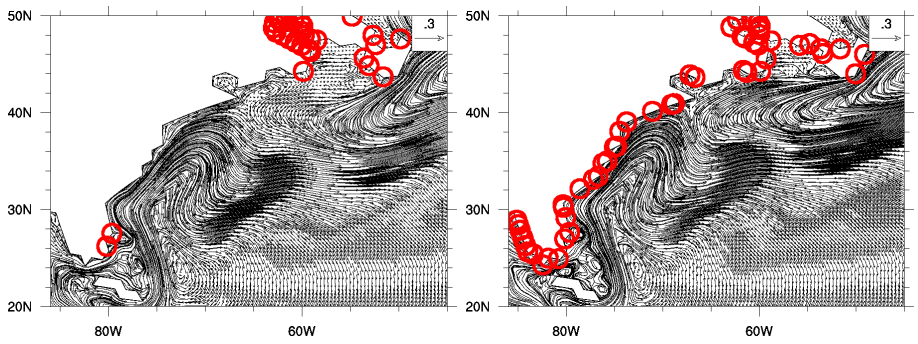

Figure 4.23: Separation points detected with zero points of ω for the no-slip (left) and the free-slip run (right) of the Atlantic test.

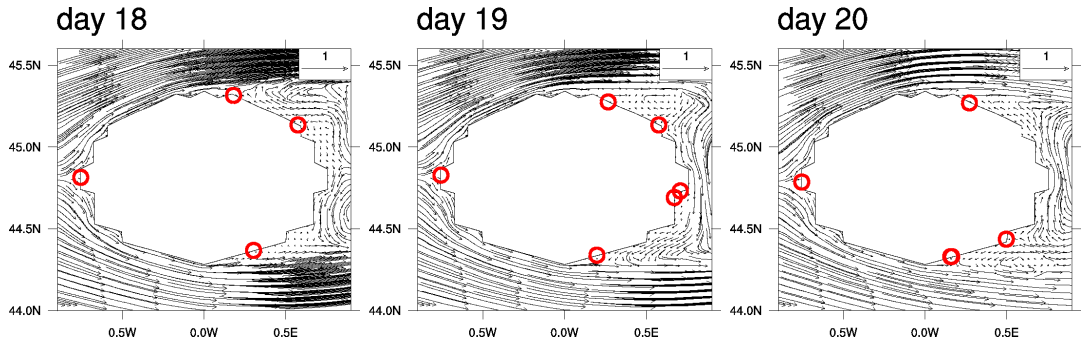

Figure 4.24: Separation points detected with zero points of ω for the no-slip run of the island test with $Re = 366$, for three different time steps.

In a series of papers Ghil, Ma, and Wang (Ma and Wang 2001; Ghil et al. 2001, 2005) study the topology of flow fields mainly with no-slip, but also with free-slip boundary conditions. They present a theory to determine structural bifurcation of two dimensional incompressible vector fields. An additional paper studies bifurcation points (Ghil et al. 2004), in which a separation and a reattachment point emerge from flow fields parallel to the boundary. When the vorticity has been positive in the neighborhood, such a bifurcation point occurs at a time t^* at a point $P(0, \gamma, t^*)$, along a meridional boundary at $x = 0$, if the following conditions are satisfied

$$\omega(0,\gamma,t^*) = 0, \qquad \partial_y\omega(0,\gamma,t^*) = 0, \qquad \partial_{yy}\omega(0,\gamma,t^*) > 0,$$
$$\text{and} \qquad \partial_t\omega(0,\gamma,t^*) < 0.$$

The conditions actually mean, that a declining vorticity along the boundary has a local minimum at $\omega = 0$. If the vorticity field in the neighborhood is negative, a bifurcation point is indicated by an increasing vorticity field that has a local maximum at $\omega = 0$. In contrast to all the other approaches discussed in this paper, the method of Ghil et al.

(2004) provides the possibility to identify separation points when they develop along the coast line.

The theory was derived for no-slip boundary conditions, incompressible continuous fluids, and idealized and curved coast lines. There is no mathematical support that the results should be valid in the used shallow-water system, since the shallow-water setup is not incompressible, although $\nabla \cdot \mathbf{u}$ is typically very small for solutions of the shallow-water equations. Nevertheless, we test the criteria in the used model setup.

Figure 4.25 and 4.26 show the unsteady flow field around the island for six time steps, and the associated vorticity field along the coast line. It is possible to track separation points along the coast line, by evaluating the change of the position of the zero vorticity points. The detachment of vortices from the coast line can be detected as well, since the corresponding zero values for vorticity disappear (look at the position of the vortices indicated by the colored dots in Figure 4.25, and the corresponding vorticity fields). The birth of a new separation point with the given mechanism by Ghil et al. (2004) can be seen for the vortex indicated by the black dots. The vorticity pattern which is apparent when the vortex is born, is marked by the black box in Figure 4.26.

Summary of the results for Approach $\mathbb{B}$

For **no-slip** boundary conditions, zero values of vorticity are a very good indicator of separation or reattachment points, although zero vorticity is not a sufficient criterion for separation or reattachment. It is possible to identify the track of vortices along the coast for unsteady flows and moving separation points, by evaluating the points of zero vorticity. Furthermore, we can detect the birth and the detachment of vortices from the coast line, by following the theory of Ghil, Ma, and Wang (Ghil et al. 2004). The use of the sufficient condition by Prandtl would probably allow the differentiation between separation and reattachment points.

For **free-slip** boundary conditions, the criterion of zero vorticity is not useful, since there are too many detected separation points, where no separation is visible.

4.5.4 Approach $\mathbb{C}$: Evaluating the change of the tangential velocity in the normal direction and the change of the normal velocity in the tangential direction following Lekien and Haller (2008)

In this subsection, we evaluate the change of the tangential velocity in the normal direction and the change of the normal velocity in the tangential direction. We start with the analysis of the approach to separation on free-slip boundaries by Lekien and Haller. Afterwards, we briefly discuss separation on no-slip boundaries.

Lekien and Haller studied separation on **free-slip** boundaries (Lekien and Haller 2008). They state that flow separation takes place at a point $\mathbf{x}$ situated on the boundary, when the following three assumptions are satisfied:

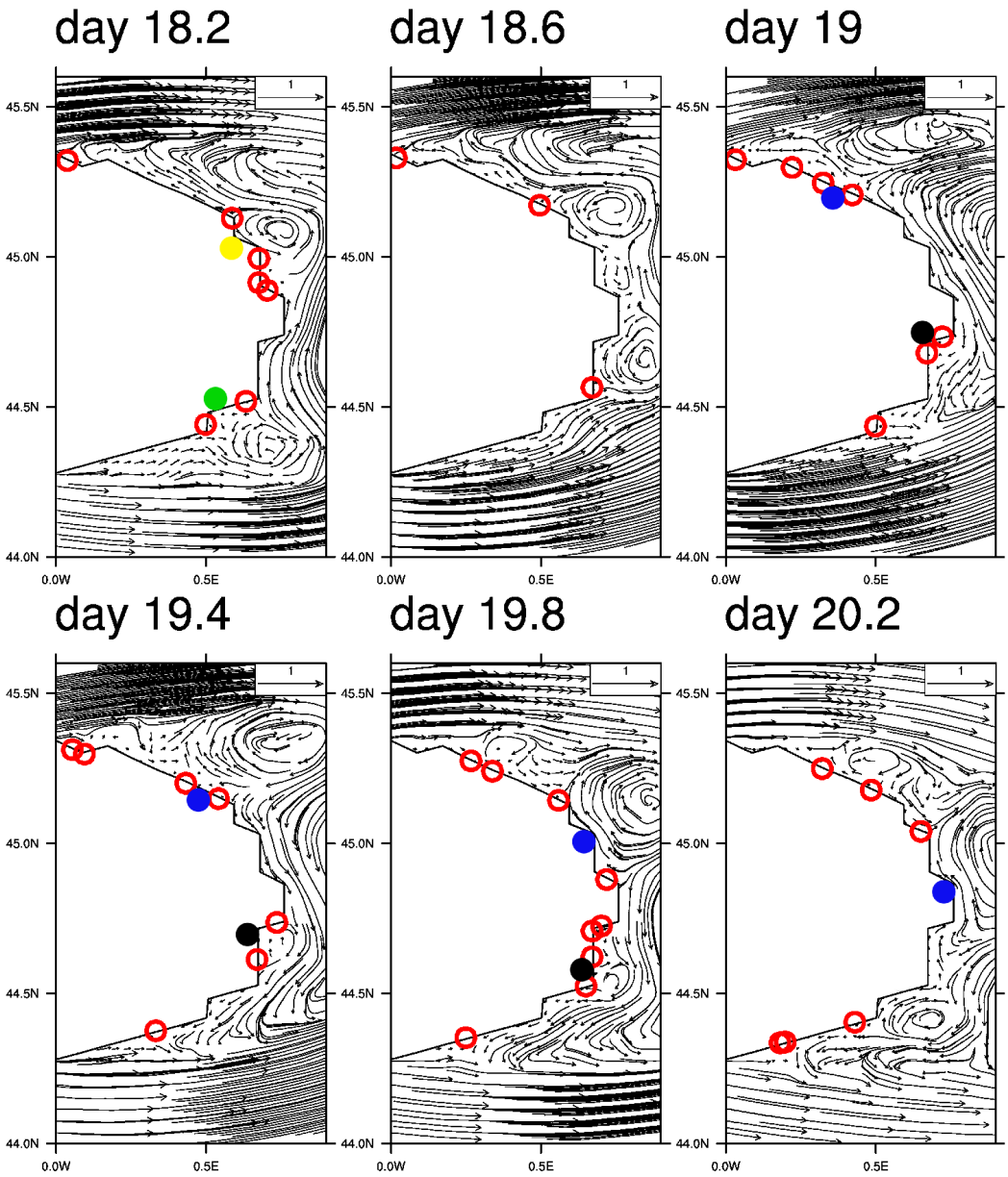

Figure 4.25: Separation points detected with zero points of ω for the no-slip run of the island test with $Re = 3000$, for different time steps. Red circles mark the detected separation points, the colored dots indicate the position of specific vortices that move along the coast.

1. $\mathbf{x}(t)$ attracts other trajectories within the boundary.

2. $\mathbf{x}(t)$ has an unique manifold that is uniformly bounded away from a portion of

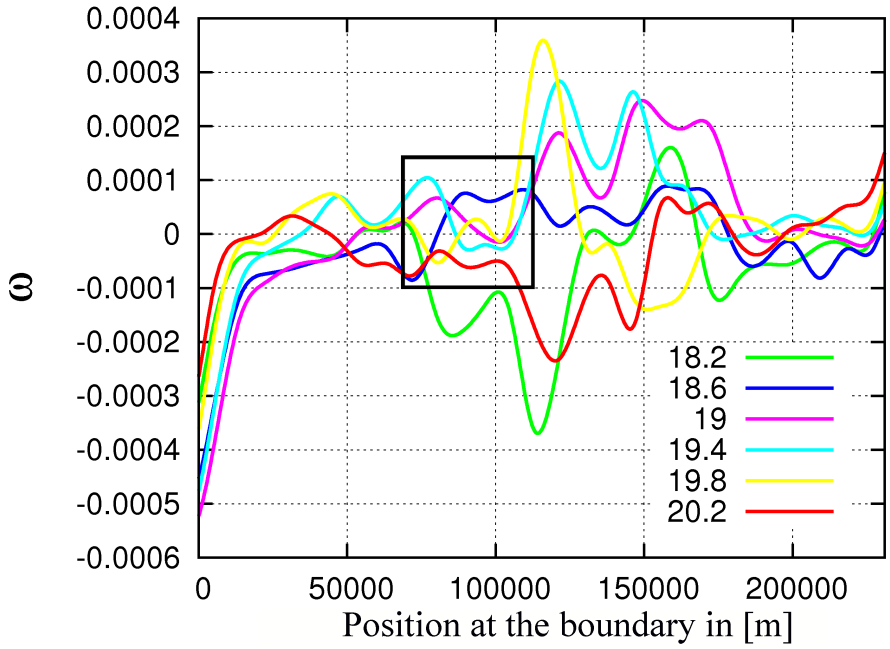

Figure 4.26: Vorticity along the boundary for the flow fields plotted in Figure 4.25, for different time steps (in days). The plotted part of the boundary starts in the south and ends in the north of the visible coast line in Figure 4.25. The black box marks the area in which a separation point is born (at day 19), and detaches from the coast (at day 20.2).

boundary, containing $\mathbf{x}(t)$ in backward time.

3. Both of the properties above are robust.

Lekien and Haller evaluated previous work of Fenichel (1971) and Mañé (1978), and concluded that the three assumptions above are sufficient and necessary conditions for normal hyperbolicity at $\mathbf{x}$, where the flow along the coast line represents the stable, and the separated flow into the domain represents the unstable trajectory of $\mathbf{x}(t)$. Starting here, Lekien and Haller studied the scaling of the velocity field along the coast line, towards the separation point. They derived the following two Lyapunov type numbers

$$\lambda_{6,\mathbf{t}} = \limsup_{T\to+\infty} \frac{1}{T} \int_{t-T}^{t} \left[\mathbf{t}\cdot((\nabla\mathbf{u}(x,y,\tau))\cdot\mathbf{t})\right]_{\mathbf{x}} d\tau, \tag{4.9}$$

$$\lambda_{6,\mathbf{n}} = \liminf_{T\to+\infty} \frac{1}{T} \int_{t-T}^{t} \left[\mathbf{n}\cdot((\nabla\mathbf{u}(x,y,\tau))\cdot\mathbf{n})\right]_{\mathbf{x}} d\tau, \tag{4.10}$$

where the lowered $\mathbf{x}$ shall indicate, that we integrate along a flow trajectory $\mathbf{x}(t)$, and follow an imaginary particle in the flow field along the coast. Flow separation takes place whenever $\lambda_{6,\mathbf{t}} < 0$, and $\lambda_{6,\mathbf{n}} > 0$. Similar criteria can be proved for flow reattachment (see Lekien and Haller 2008).

The results are derived for free-slip boundary conditions and moving separation points in a continuous fluid. If $\lambda_{6,\mathbf{t}}$ and $\lambda_{6,\mathbf{n}}$ are calculated for discrete model output and the flow trajectories are integrated over finite time intervals, $\lambda_{6,\mathbf{t}}$ and $\lambda_{6,\mathbf{n}}$ will not be zero at points where no separation takes place. Therefore, we replace the conditions 'smaller or greater than zero' with the conditions 'local minima and maxima' of the two Lyapunov type quantities, as it was done in Lekien and Haller (2008).

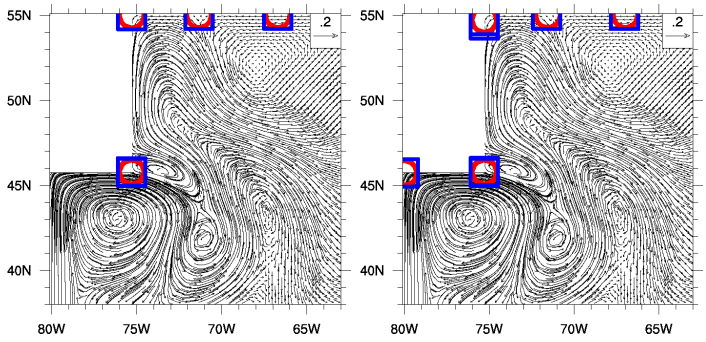

Figure 4.27: Separation points detected with the criteria by Lekien and Haller for the free-slip run of the idealized coast line test. The criteria were integrated over 150 (left) and 26 days (right). The red circles mark minima of $\lambda_{6,\mathbf{t}}$, the blue squares mark maxima of $\lambda_{6,\mathbf{n}}$.

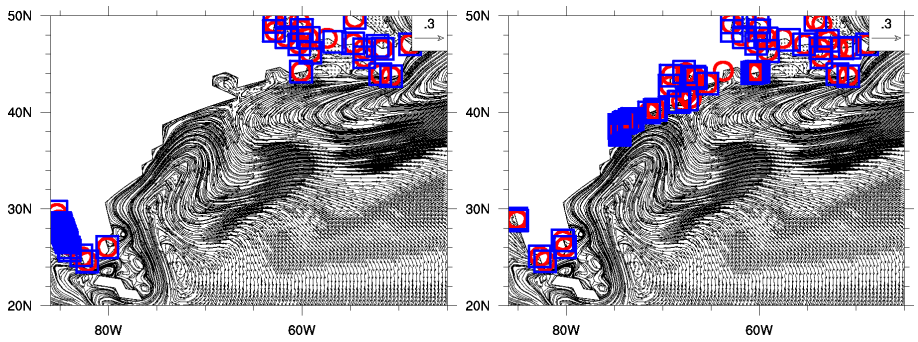

Figure 4.28: Separation points detected with the criteria by Lekien and Haller for the free-slip run of the Atlantic test. The criteria were integrated over 166 (left) and 24 days (right). The red circles mark minima of $\lambda_{6,\mathbf{t}}$, the blue squares mark maxima of $\lambda_{6,\mathbf{n}}$.

Figure 4.27 and 4.28 show the results for steady flows with free-slip boundaries. The

criteria of Lekien and Haller are able to identify the separation points (compare with Figure 4.3 and 4.5), but they appear to be sensitive to turns of the coast line and detect separation points, where no separation is visible. Results improve when the integration time is increased.

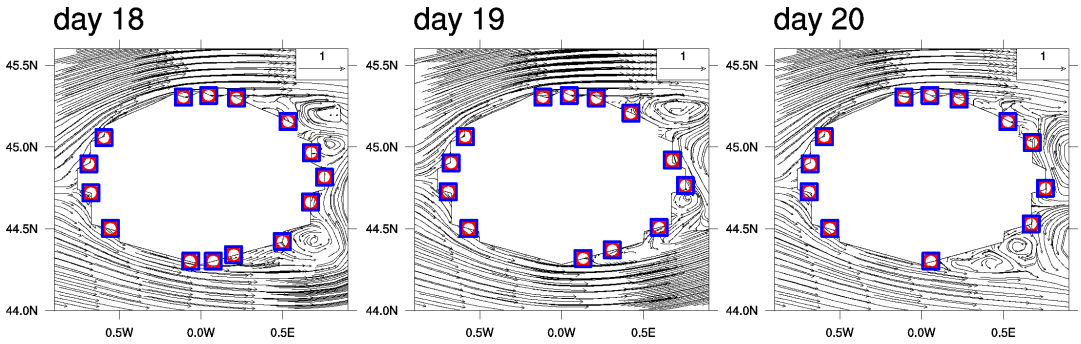

Figure 4.29: Separation points detected with the criteria by Lekien and Haller for the free-slip run of the island test with $Re = 3000$, for different time steps. The time integrations for the criteria start at day 17. The red circles mark minima of $\lambda_{6,\mathbf{t}}$, the blue squares mark maxima of $\lambda_{6,\mathbf{n}}$.

Figure 4.29 shows the time evolution for the detection of separation points in the unsteady island test with $Re = 3000$ and free-slip boundaries. Several separation points are indicated by the criteria at turns of the coast line, while some areas are depopulated from diagnostic particles at locations where new separation points develop.

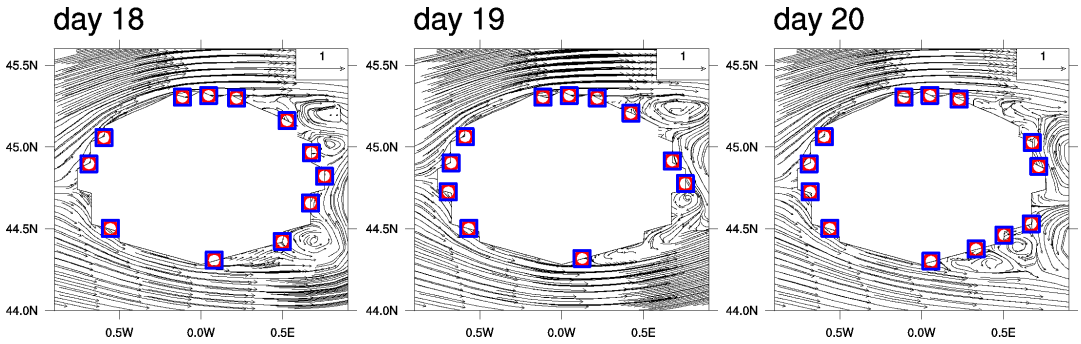

Figure 4.30: Separation points detected with the criteria by Lekien and Haller for the free-slip run of the island test with $Re = 3000$, for three time steps. The criteria were integrated over thirty days with fixed velocity fields at a given time step. The red circles mark minima of $\lambda_{6,\mathbf{t}}$, the blue squares mark maxima of $\lambda_{6,\mathbf{n}}$.

We suggest another application of the criteria. We integrate $\lambda_{6,\mathbf{t}}$ and $\lambda_{6,\mathbf{n}}$ along the coast line, while we fix the velocity field at a given time step. The criteria can adjust in a 'steady' flow. Figure 4.30 shows the detected separation points with the criteria of

Lekien and Haller. Integration was performed with fixed velocity fields at the different time steps. The results are better than the results in Figure 4.29. Still, many of the turns of the coast line are indicated to be separation points.

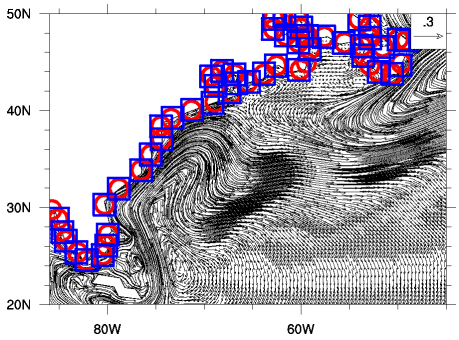

Figure 4.31: Separation points detected with the criteria by Lekien and Haller for the no-slip run of the Atlantic test with zero integration time. The red circles mark minima of $\lambda_{6,\mathbf{t}}$, the blue squares mark maxima of $\lambda_{6,\mathbf{n}}$.

The mathematical support for the criteria by Lekien and Haller does not hold for **no-slip** boundaries. Line 4 and 8 of Table 4.3 indicate that the criteria (4.9) and (4.10) could also be useful for no-slip boundaries, at least for zero integration times. Figure 4.31 shows the results for the evaluation of criteria (4.9) and (4.10) for the no-slip Atlantic simulation. The criteria detect too many separation points, where no separation is visible.

Summary of the results for Approach $\mathbb{C}$

For **no-slip** boundary conditions, we do not obtain useful diagnostics to identify separation points.

For **free-slip** boundary conditions, we evaluate the separation criteria developed by Lekien and Haller (Lekien and Haller 2008). The criteria were derived for moving, unsteady separation. We obtain good results, but problems appear since long time integrations along the flow trajectories are needed for the evaluation of the criteria, to avoid unwanted detections of separation at turns of the coast line. If the integration time is too long, parts of the coast line are depopulated from diagnosing particles that move in the flow. For unsteady flows, we can improve the results by integrating the separation criteria along the coast line with fixed velocity fields, at a specific time step.

4.5.5 Approach $\mathbb{D}$: Evaluating the ratio between the tangential and normal velocity components

In this subsection, we evaluate the ratio between the tangential and normal velocity components. We derive a necessary criterion for unsteady, fixed flow separation on no-slip boundaries, and motivate why this criterion should also hold for free-slip boundaries. Afterwards, we test the criterion in model simulations with no-slip and free-slip boundaries.

For the derivation of a criterion for separation on **no-slip** boundaries, we follow the assumptions in Haller (2004). In difference to Haller (2004), we do not evaluate the continuity equation at the boundary. We study a boundary aligned with the y coordinate ($x = 0$). We start from the assumption discussed in Haller (2004), that fixed unsteady separation occurs, if a boundary point $P(0, \gamma)$ admits an unstable manifold that is not tangent to the boundary. The unstable manifold is locally represented by a time-dependent graph

$$y = \gamma + xF\left(x, t\right), \tag{4.11}$$

which describes the time evolution of the tangent coordinate of a particle, which is separating on the unstable manifold. F defines the separation profile. As in Haller (2004) we develop the function F into a series expansion

$$F(x, t) = f_0(t) + xf_1(t) + \frac{1}{2}x^2 f_2(t) + \ldots .$$

Haller (2004) identifies $f_0(t)$ to be the tangent of the angle that the separation profile encloses with the wall-normal at the separation point. At this point we differ from Haller (2004) and take the time derivative of equation (4.11) and obtain

$$v(x, y, t) = \partial_t \gamma + u(x, y, t)F(x, t) + x\partial_t F(x, t), \tag{4.12}$$

using $\partial_t x(x, y, t) = u(x, y, t)$ and $\partial_t y(x, y, t) = v(x, y, t)$. Since we assume fixed separation, we know that $\partial_t \gamma = 0$. When model output of a finite difference model is evaluated at the point $P(0, \gamma)$, all terms in equation (4.12) will be zero for the assumed no-slip boundary conditions. In contrast, the weak form of the differential equation used in finite element models allows the velocity field at the boundary to be different from zero. The velocity at the boundary is not only dependent on the coast line, but on the whole area of the boundary grid cell. In our model, the velocity does not need to be strictly zero along the boundary. We evaluate equation (4.12) at $P(0, \gamma)$ as

$$v(0, \gamma, t) = u(0, \gamma, t)f_0(t).$$

Fixed separation takes place when $f_0(t)$ remains bounded in backward time. We obtain a necessary condition for separation

$$\limsup_{t\to-\infty}\left|\int_{t_0}^{t}\frac{v(0,\gamma,\tau)}{u(0,\gamma,\tau)}d\tau\right|<\infty. \tag{4.13}$$

The condition is difficult to evaluate in our numerical model, since we do not obtain infinite values for the discrete model output. Assuming the integral in equation (4.13) to be $-\infty$ if $y>\gamma$, and ∞ if $y<\gamma$, which is reasonable when fixed separation is considered, we end up with the following condition for points of flow separation

$$\lambda_7=\limsup_{t\to-\infty}\int_{t_0}^{t}\left[\frac{\mathbf{t}\cdot\mathbf{u}\,(x,y,\tau)}{\mathbf{n}\cdot\mathbf{u}\,(x,y,\tau)}\right]_{\mathbf{x}}d\tau=0. \tag{4.14}$$

The necessary criterion (4.14) is derived for no-slip boundary conditions and unsteady, but fixed separation.

For **free-slip** boundaries the flow trajectories at the separation point is hyperbolic (see Lekien and Haller 2008, and Approach ℂ). The coast can be assumed to form the stable trajectories of the separation point. The flow along the coast line will not cross the separation point, and it will not leave the coast, due to the condition for the normal component of velocity to be zero at the boundary. It is likely that the flow shows the properties listed in line 1, 2, and 3 in Table 4.3, and keeps the signs of the velocity components while approaching the separation point. The signs are opposite on both sides of the idealized separation point. The change of the sign happens at the separation point. Therefore, we will evaluate criterion (4.14) also for free-slip boundary conditions.

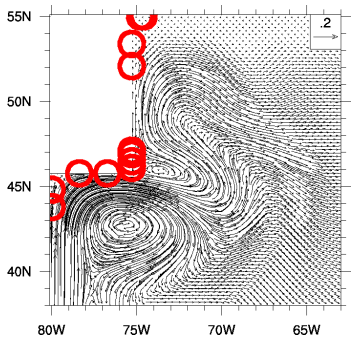

Figure 4.32: Separation points detected with criterion (4.14) for the no-slip run of the idealized coast line test. The criterion was integrated over 26 days. Since we study steady flows and no-slip boundary conditions, the results do not change with the integration time.

The Figures 4.32, 4.33, and 4.34 show the results for steady and unsteady separation

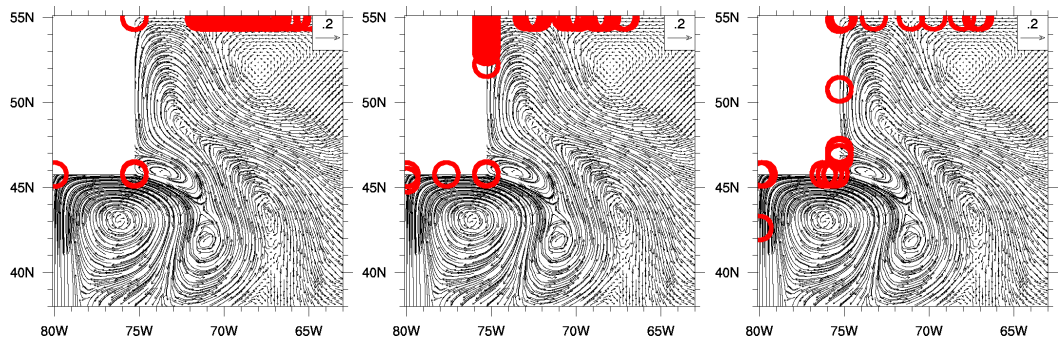

Figure 4.33: Separation points detected with criterion (4.14) for the free-slip run of the idealized coast line test. The criterion was integrated over 100, 26, and 0 days (from left to right).

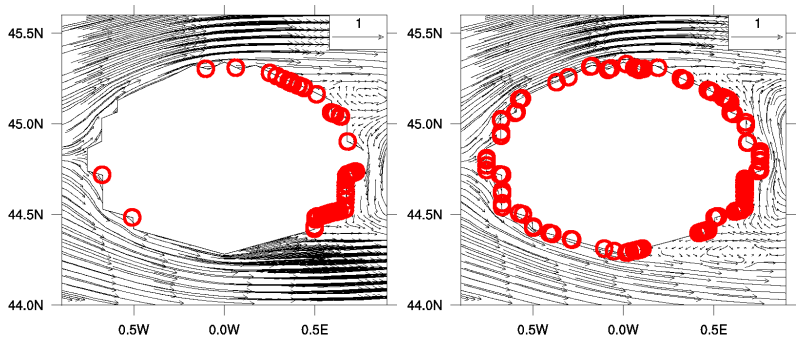

Figure 4.34: Separation points detected with criterion (4.14) for the free-slip (left) and the no-slip (right) run of the island test with $Re = 366$. The criterion was integrated over 2 days.

for no-slip and free-slip boundary conditions. The criterion detects many separation points, where no separation is visible.

Summary of the results for Approach $\mathbb{D}$

We derive a necessary separation criterion for unsteady, fixed separation on **no-slip** boundaries. We motivate why the developed criterion might also be valid for **free-slip** boundaries. Unfortunately, the developed criterion is not sufficient for both boundary conditions, since too many separation points are detected, where no separation is visible. Results would probably be better for a finite element model with a continuous representation of the velocity field.

4.5.6 Approach $\mathbb{E}$: Evaluating the derivative of the height field in the normal and the tangential direction following Haidvogel et al. (1992)

In this subsection, we evaluate the derivative of the height field in the normal and tangential direction. We motivate a separation criterion for the change in the tangential direction from the numerical study in Haidvogel et al. (1992), and a criterion for the change in the normal directions from geostrophic balance. Afterwards, we test the criteria in model simulations on no-slip and free-slip boundaries.

Haidvogel et al. (1992) simulated boundary currents in idealized ocean domains with idealized coast lines, and observed that boundary separation coincides with a strong adverse pressure gradient for **no-slip and free-slip** boundary conditions. A pressure gradient opposes the flow along the wall and forces it to separate. Haidvogel et al. (1992) analyzed the flow field in 60 km distance to a straight, meridional coast. Since they evaluated the quasigeostrophic potential vorticity, and not the momentum equations, they could not evaluate the pressure gradient solely, but investigated a quantity they called the higher-order pressure gradient, which includes a part of the Coriolis term. The existence of an adverse pressure gradient at boundary separation points is also known from the literature in Fluid Dynamics (Monin et al. 2007). It was shown in Ghil et al. (2004) that an adverse pressure gradient is also present at the bifurcation point discussed for Approach $\mathbb{B}$.

Following the results of Haidvogel et al. (1992) we evaluate the quantity

$$\lambda_8 = \mathbf{t} \cdot (\nabla \cdot h) \cdot \text{sign}[\mathbf{t} \cdot \mathbf{u}]. \tag{4.15}$$

λ_8 describes the change of the height field in the direction of the flow along the coast. This is equivalent to an adverse pressure gradient. If λ_8 shows a maximum at a value larger than a constant c, which is adjusted to the flow field, we take this as a criterion for possible flow separation points.

We derive a second criterion for flow separation based on geostrophic balance ($f\mathbf{k} \times \mathbf{u} \approx -g\nabla h$). Geostrophic balance is not valid within a typical western boundary current, since the currents are in the turbulent flow regime, where the main balance of the momentum equation holds between advection and diffusion. Nevertheless, geostrophic balance should be a good assumption for the flow field outside the boundary current. We know that clockwise gyres show a positive, and anti-clockwise gyres show a negative height anomaly for the shallow-water system on the northern hemisphere, due to geostrophic balance. The anomalies level out against the boundary. Given this, and line 10 of Table 4.3, we derive the following criterion for possible flow separation points

$$\lambda_9 = \mathbf{n} \cdot (\nabla \cdot h) = 0. \tag{4.16}$$

We can only offer a principle explanation why the two criteria above should be physically meaningful. We can not offer a strict mathematical foundation.

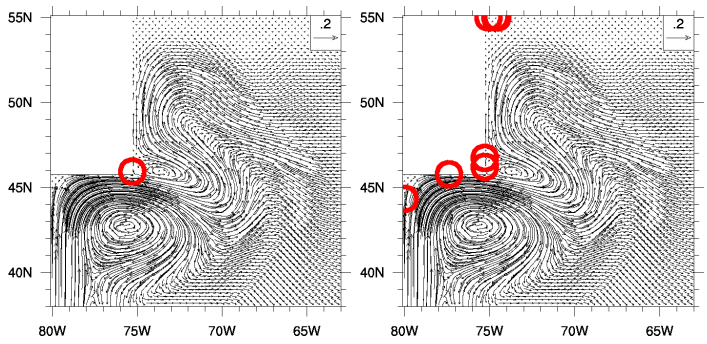

Figure 4.35: Separation points detected with criterion (4.15) with $c = 5 \cdot 10^{-10}$ (left) and criterion (4.16) (right) for the no-slip run of the idealized coast line test.

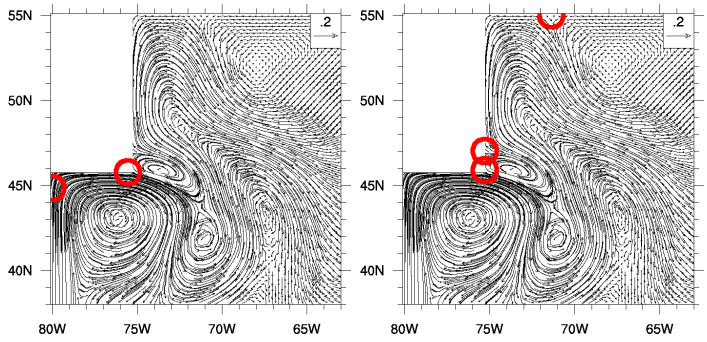

Figure 4.36: Separation points detected with criterion (4.15) with $c = 5 \cdot 10^{-7}$ (left) and criterion (4.16) (right) for the free-slip run of the idealized coast line test.

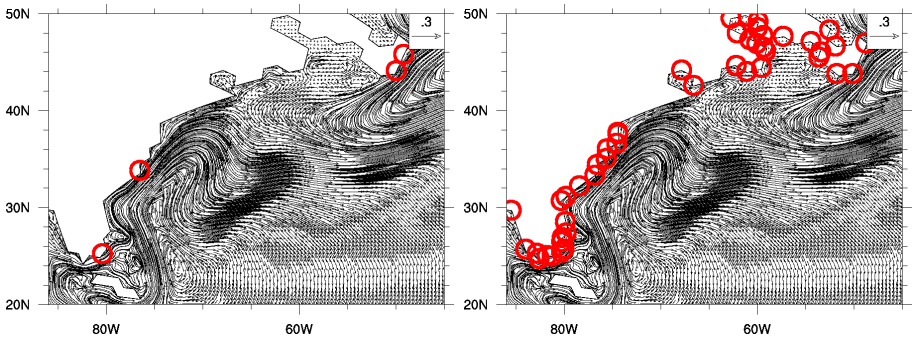

Figure 4.37: Separation points detected with criterion (4.15) with $c = 1 \cdot 10^{-7}$ (left) and criterion (4.16) (right) for the no-slip run of the Atlantic test.

The Figures 4.35, 4.36, 4.37, 4.38, 4.39, and 4.40 show the results for the criteria (4.15) and (4.16) for steady and unsteady flows. While criterion (4.15) gives better results on **no-slip** boundaries, criterion (4.16) gives better results on **free-slip** bound-

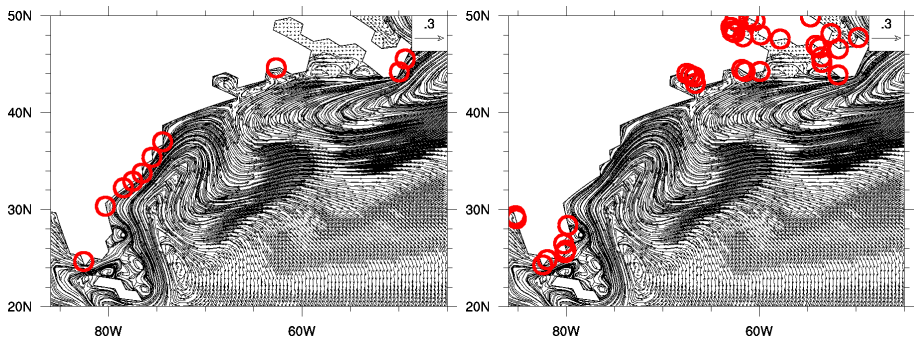

Figure 4.38: Separation points detected with criterion (4.15) with $c = 1 \cdot 10^{-6}$ (left) and criterion (4.16) (right) for the free-slip run of the Atlantic test.

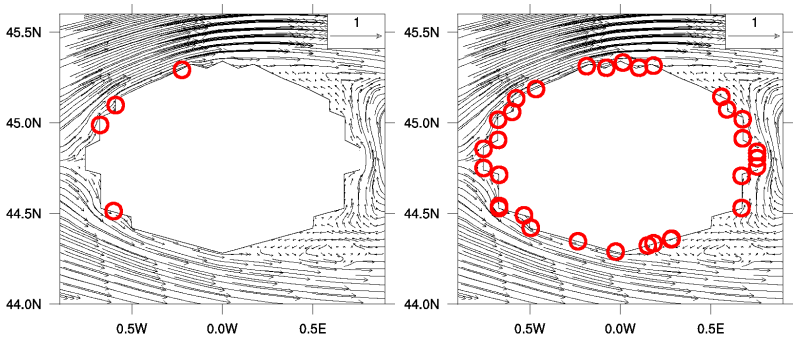

Figure 4.39: Separation points detected with criterion (4.15) with $c = 5 \cdot 10^{-7}$ (left) and criterion (4.16) (right) for the no-slip run of the island test with $Re = 366$.

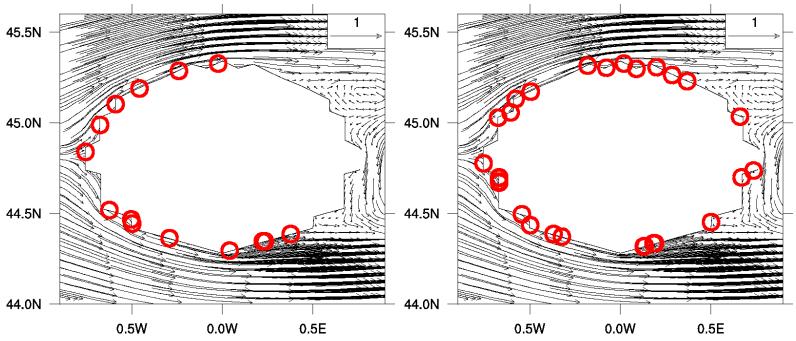

Figure 4.40: Separation points detected with criterion (4.15) with $c = 5 \cdot 10^{-7}$ (left) and criterion (4.16) (right) for the free-slip run of the island test with $Re = 366$.

aries. The necessity to define c for criterion (4.15) leads to some lost detections (for example for the northern separation point in Figure 4.35). If c is too small, too many possible separation points are detected.

Both approaches fail to provide useful information on the separation points in the unsteady island test. Too many separation points are detected, where no separation is visible.

Summary of the results for Approach $\mathbb{E}$

For **no-slip** conditions and idealized coast lines, we obtain good results by evaluating the change of height in the tangential direction. Unfortunately, the criterion for the tangential change is difficult to analyze, since a minimal value for the change needs to be adjusted to the flow field, from which we start to count a maximum of the tangential change to indicate a possible separation point. For **free-slip** conditions and idealized coast lines, we obtain good results from the change of the height in the normal direction. We fail to elaborate useful diagnostic tools to detect separation points for coast lines as used in ocean models, by evaluating the change of the height field, since too many possible separation points are detected for **both** boundary conditions. The results might be better if the change of the height field is not considered along the coast line, but in close distance. This was done in Haidvogel et al. (1992), for an idealized coast line.

4.6 Discussion of the results

4.6.1 On western boundary currents in a finite element shallow-water model

We study the numerical representation of western boundary currents in finite element models (section 4.4). Although finite element methods provide an improved coast line representation compared to finite difference methods, our investigations show that the representation of the coast line and the boundary conditions is still not satisfying. Small changes of the grid structure can lead to changes of the separation behavior (see Figure 4.10).

Our tests on the influence of resolution and eddy viscosity show that steady western boundary currents are not strongly affected by changes in resolution, as long as the Munk layer is resolved properly (subsection 4.4.1 and 4.4.2). However, a higher resolution allows the use of a smaller eddy viscosity, which can change the model results significantly. To this end, grid refinement can be used to increase the local resolution in the Munk layer.

The model results change strongly between free-slip and no-slip boundary conditions, when idealized coast lines are simulated (subsection 4.4.1). On the other hand, the model results change only slightly with the boundary conditions for coast lines as used in ocean models (subsection 4.4.2). In simulations with free-slip boundaries and zig-zag or unstructured coast lines, the flow is shifted towards the interior of the domain,

due to the rapid changes of the direction of the coast line. The results look similar to no-slip model runs, in which the flow is shifted into the interior of the domain via the boundary conditions (subsection 4.4.1).

In contrast to finite difference models with the vorticity as prognostic quantity (Dengg 1993), we obtain separation for free-slip boundary conditions, using a finite element model with velocity and height as prognostic quantities. We do obtain premature separation for no-slip, but not for free-slip boundary conditions (subsection 4.4.2). This result is consistent with results of finite difference models.

For the Atlantic test, no boundary separation point is visible along the coast line in the area around the separation of the Gulf stream type flow (see Figure 4.5), neither for no-slip, nor for free-slip boundaries. The flow field is only slightly affected by the boundary condition, but strongly affected by a change of eddy viscosity. This indicates that Gulf stream separation is less dependent on the kinematic in the direct vicinity of the coast line, but more dependent on the internal dynamics of the system, fixed by the equations of motion, and parametrization. Of course, these results might be specific for the given shallow-water setup, and might differ from results in full ocean models.

4.6.2 On criteria to detect boundary separation points

In the second part of this paper, we try to identify proper criteria to detect boundary separation points in ocean modeling, for free-slip and no-slip boundary conditions. We investigate five approaches, where each approach evaluates specific physical quantities. In summary, we obtain very good results for the detection of boundary separation points with Approach $\mathbb{A}$ and $\mathbb{B}$ for no-slip boundaries, and good results with Approach $\mathbb{C}$ for free-slip boundaries. We are very optimistic that Prandtls separation criteria, or the evaluation of zero points for vorticity would allow a proper identification of separation points in two dimensional layers of a finite element ocean model with no-slip boundaries. For free-slip boundaries the separation criteria by Lekien and Haller would probably give good results, although success will depend on a proper tuning of the integration time, and there will be some unwanted detections of separation at turns of the coast line. We can improve the results for the criteria by Lekien and Haller by integrating the criteria along flow trajectories in fixed velocity fields, at a specific time step.

The facts that the best methods are based on the shear of the velocity field for no-slip boundary conditions, and the components of the divergence of the velocity field for free-slip boundary conditions, show the extensive difference between the mechanism of separation on no-slip and free-slip boundaries. Since the study of the gradient of the height field was not successful for the identification of separation points on realistic coast lines, neither for no-slip, nor for free-slip boundary conditions, we expect the height field to play a minor role for boundary separation in shallow-water models.

Although the approaches from dynamical systems theory show some difficulties in detecting flow separation points for unsteady, moving separation, and it seems to be necessary to include the physical fields close to the boundary and not only the flow fields along the coast line into considerations, these types of approaches appear very promising.

To derive criteria to detect Gulf stream type separation, it seems to be necessary to include the equations of motion into considerations, since the Gulf stream appears to be driven by the dynamics of the system, rather than the kinematics along the coast line.

4.7 Main conclusions

- First Part: Although finite element methods offer an improved coast line representation compared to finite difference methods, the representation of boundary flows remains dependent on the pattern of the coast line, which is – for today's ocean models – very much dependent on the resolution. Small changes of the grid structure can lead to significant changes in the separation behavior.

- Second Part: For no-slip boundaries, we obtain the best results to detect steady and unsteady separation points in ocean modeling by using Prandtls criteria for separation points. In principle, Prandtls criteria are only valid for steady flows. For free-slip boundaries, we obtain the best results by evaluating the separation criteria by Lekien and Haller. Unfortunately, the criteria by Lekien and Haller are sensitive to turns of the coast line, and dependent on the used integration time along the flow trajectories.

Chapter 5

Conclusions and Outlook

5.1 Scientific contribution

To the best of our knowledge we are the first

- to develop a global shallow-water model based on the hybrid continuous/discontinuous $P_1^{DG}P_2$ finite element approach,
- to use the stereographic projection to introduce spherical geometry to a global finite element model,
- to study errors and improvements possible with grid refinement in a global $P_1^{DG}P_2$ finite element shallow-water model,
- to test the applicability of recently developed theories of boundary separation in ocean models, based on dynamical systems theory, or considerations of the flow topology,
- to provide a detailed study of the discretized physical fields in a finite element model, along a coast line as it is used in ocean models.

In summary, the main results of this thesis show that

- the evaluated $P_1^{DG}P_2$ finite element approach is applicable for global modeling and has very promising properties for use in dynamical cores of global weather or climate models,
- the improvements possible with a deliberated use of local grid refinement justify the risk of spurious reflections and scatterings in the used global finite element shallow-water model,
- even though finite element methods offer an improved coast line representation compared to finite difference methods, small changes of the grid structure can lead to significant changes in the separation behavior of boundary currents,

- Prandtls criteria for the separation of steady flows are proper criteria to detect separation of steady and unsteady flows in finite element models for ocean applications with no-slip boundaries, while the separation criteria by Lekien and Haller offer the best results to detect separation points on free-slip boundaries.

5.2 Answers to the Research Questions

We can now answer the research questions stated in the introduction.

- **Can we develop a stable shallow-water model setup on the sphere, using the $P_1^{DG}P_2$ finite element approach?**

  Yes. We present a stable model setup for a global $P_1^{DG}P_2$ shallow-water model. We do not observe any spurious modes that necessitate additional diffusion or stabilization schemes, in all tests performed. Regarding the convergence properties and kinetic energy spectra, our discretization shows the expected behavior.

- **What is the best way to introduce spherical geometry to a finite element model?**

  We introduce the spherical geometry using the stereographic projection. The projection is accurate and cheap, and easier to implement, compared to other methods from the literature. Unfortunately, the coupling of two stereographic projections for atmospheric applications leads to a small error in global mass conservation.

- **How does a $P_1^{DG}P_2$ finite element model compare to other models, such as the hybrid finite volume/finite difference ICON shallow-water model (Rípodas et al. 2009)?**

  On the same grids, the $P_1^{DG}P_2$ finite element model clearly shows a smaller error norm than the ICON shallow-water model. The effective resolution per computational cost could not be compared within the scope of this thesis, since the finite element model is not tuned to maximal performance.

- **What is the influence of grid refinement on small- and large-scale flow patterns?**

  While the reflection and scattering is severe for waves represented by less than five grid cells per wave length, large-scale flow features are unaffected by grid refinement in all tests performed. The errors are fairly independent of the structure

of the transition zone and the change of resolution between fine and coarse parts of the grids.

- **Is the ability to represent the geostrophic balance and the representation of turbulent cascades influenced by grid refinement in a $P_1^{DG}P_2$ finite element model?**

  Grid refinement does not perturb the representation of the geostrophic balance, and improves the representation of turbulent cascades.

- **In which applications can grid refinement improve the simulations of a $P_1^{DG}P_2$ shallow-water model?**

  Grid refinement can lead to a significant improvement of simulations of flow over topography, local wave patterns, and western boundary currents.

- **How good is the numerical representation of boundary currents in the $P_1^{DG}P_2$ finite element shallow-water model?**

  Although finite element methods offer a significantly improved coast line representation compared to finite difference methods, the representation of boundary currents is still not satisfying. Due to the insufficient resolution, small changes of the coast line can lead to significant changes in the separation behavior.

- **Can we find proper criteria to detect boundary separation points in a finite element shallow-water model, for no-slip and free-slip boundary conditions?**

  Out of all of the evaluated criteria to detect boundary separation points on no-slip boundaries, Prandtls separation criteria work best. For free-slip boundaries, the separation criteria by Lekien and Haller turned out to be the best choice. Unfortunately, the criteria by Lekien and Haller are dependent on the integration time along the flow trajectories, and sensitive to turns of the coast line.

- **What are the properties of separation points of Gulf stream type flows in the $P_1^{DG}P_2$ finite element shallow-water model?**

  The separation of Gulf stream type flows is influenced stronger by a change in eddy viscosity than by a change between no-slip or free-slip boundary conditions. In the used shallow-water model, it was not possible to detect Gulf stream type separation by evaluating the kinematics of the physical fields along the coast line, since the separation is rather driven by the interior dynamics of the system.

5.3 Outlook

The developed shallow-water model could be improved with semi-implicit or implicit time stepping methods. Since a linear system of equations needs to be solved for all prognostic variables, also for explicit time stepping methods, the use of (semi-) implicit methods could lead to a significant reduction of the computational cost, due to longer time steps. The use of a less diffusive Riemann solver, compared to the used Lax-Friedrich method, could probably improve the results.

The next natural step towards a full ocean and atmosphere model based on the $P_1^{DG}P_2$ finite element approach, would be the extension of the shallow-water model to three dimensions. This could be done within the ICON model developing project at the Max Planck Institute for Meteorology in Hamburg. The vertical discretization could be transferred from the given hybrid finite volume/finite difference dynamical core, at least to a large extent. This would allow us a direct comparison of model accuracy and performance between the finite element and the hybrid finite volume/finite difference method.

For the analysis of grid refinement in GFD, the next step should be to incorporate and evaluate grid refinement in full ocean and atmosphere models. Possible tests could apply grid refinement in regions of specific interest, such as the area around Cape Hatteras, the Denmark straight, or the Himalaya region, but also around Europe, the Arctic, or the Tropics, in global model runs. For the developed $P_1^{DG}P_2$ finite element model, it is already possible to perform grid refinement within a model run. Therefore, it would be comparatively easy to implement the possibility of adaptive grid refinement.

For the considerations of boundary currents, the next step should be to test the separation criteria by Prandtl, and Lekien and Haller in full ocean models. This should be done either in hybrid finite volume/finite difference models, such as the ICON model, or in finite element models such as FEOM or ICOM (ocean models developed at the Alfred Wegener Institute and Imperial College London). For further investigations of the mechanism of boundary separation, one should include the physical fields in the vicinity of the coast line into considerations. For further investigations of the separation of Gulf stream type flows, it will be necessary to evaluate the dynamics of the underlying equations of motion.

Bibliography

Adcroft, A. and D. Marshall, 1998: How slippery are piecewise-constant coastlines in numerical ocean models? *Tellus A*, **50 (1)**, 95–108.

Baumgardner, J. R. and P. O. Frederickson, 1985: Icosahedral discretization of the two-sphere. *SIAM Journal on Numerical Analysis*, **22 (6)**, pp. 1107–1115.

Bernard, P.-E., J.-F. Remacle, R. Comblen, V. Legat, and K. Hillewaert, 2009: High-order discontinuous Galerkin schemes on general 2d manifolds applied to the shallow water equations. *Journal of Computational Physics*, **228 (17)**, 6514 – 6535.

Bonaventura, L. and T. Ringler, 2005: Analysis of discrete shallow-water models on geodesic Delaunay grids with c-type staggering. *Monthly Weather Review*, **133 (8)**, 2351–2373.

Branicki, M. and S. Wiggins, 2010: Finite-time Lagrangian transport analysis: stable and unstable manifolds of hyperbolic trajectories and finite-time Lyapunov exponents. *Nonlinear Processes in Geophysics*, **17 (1)**, 1–36.

Browning, G., J. Hack, and P. Swarztrauber, 1989: A comparison of three numerical methods for solving differential equations on the sphere. *Monthly Weather Review*, **117 (5)**, 1058–1075.

Bryan, F. O., M. W. Hecht, and R. D. Smith, 2007: Resolution convergence and sensitivity studies with North Atlantic circulation models. Part 1: The western boundary current system. *Ocean Modelling*, **16 (3-4)**, 141 – 159.

Bryan, K., 1969: A numerical method for the study of the circulation of the world ocean. *Journal of Computational Physics*, **4 (3)**, 347 – 376.

Chassignet, E. P. and Z. D. Garrao, 2001: Viscosity parameterization and the Gulf Stream separation. *Proceedings 'Aha Huliko'a Hawaiian Winter Workshop. U. of Hawaii. January*, 15–19.

Chassignet, E. P. and D. P. Marshall, 2008: *Gulf Stream separation in numerical ocean models*, 39–62. AGU Monograph Series.

Chen, Y. and H. Kuo, 1986: A global model with overlapping mercator and stereographic grids. *Advances in Atmospheric Sciences*, **3**, 302–313.

Comblen, R., J. Lambrechts, J.-F. Remacle, and V. Legat, 2010: Practical evaluation of five partly discontinuous finite element pairs for the non-conservative shallow water equations. *International Journal for Numerical Methods in Fluids*, **63 (6)**, 701 – 724.

Cotter, C. and D. Ham, 2011: Numerical wave propagation for the triangular P1DG-P2 finite element pair. *Journal of Computational Physics*, **230 (8)**, 2806 – 2820.

Cotter, C. J., D. A. Ham, and C. C. Pain, 2009a: A mixed discontinuous/continuous finite element pair for shallow-water ocean modelling. *Ocean Modelling*, **26 (1-2)**, 86 – 90.

Cotter, C. J., D. A. Ham, C. C. Pain, and S. Reich, 2009b: LBB stability of a mixed Galerkin finite element pair for fluid flow simulations. *Journal of Computational Physics*, **228 (2)**, 336 – 348.

Danilov, S., G. Kivman, and J. Schröter, 2004: A finite-element ocean model: Principles and evaluation. *Ocean Modelling*, **6 (2)**, 125 – 150.

Dengg, J., 1993: The problem of Gulf Stream separation: A barotropic approach. *Journal of Physical Oceanography*, **23 (10)**, 2182–2200.

Dong, C., J. C. McWilliams, and A. F. Shchepetkin, 2007: Island wakes in deep water. *Journal of Physical Oceanography*, **37 (4)**, pp. 962–981.

Düben, P. D., P. Korn, and V. Aizinger, 2012: A discontinuous/continuous low order finite element shallow water model on the sphere. *Journal of Computational Physics*, **231 (6)**, 2396 – 2413.

Fenichel, N., 1971: Persistence and smoothness of invariant manifolds for flows. *Indiana University Mathematics Journal*, **21 (3)**, 193–226.

Galewsky, J., R. K. Scott, and L. M. Polvani, 2004: An initial-value problem for testing numerical models of the global shallow-water equations. *Tellus*, **A (56)**, 429 – 440.

Ghil, M., J.-G. Liu, C. Wang, and S. Wang, 2004: Boundary-layer separation and adverse pressure gradient for 2-d viscous incompressible flow. *Physica D: Nonlinear Phenomena*, **197 (1 - 2)**, 149 – 173.

Ghil, M., T. Ma, and S. Wang, 2001: Structural bifurcation of 2-d incompressible flows. *Indiana University Mathematics Journal*, **50**, 159 – 180.

Ghil, M., T. Ma, and S. Wang, 2005: Structural bifurcation of 2-d nondivergent flows with Dirichlet boundary conditions: Applications to boundary-layer separation. *SIAM Journal on Applied Mathematics*, **65 (5)**, 1576 – 1596.

Giraldo, F. X., 1997: Lagrange-Galerkin methods on spherical geodesic grids. *Journal of Computational Physics*, **136 (1)**, 197 – 213.

Giraldo, F. X., 2006: High-order triangle-based discontinuous Galerkin methods for hyperbolic equations on a rotating sphere. *Journal of Computational Physics*, **214**, 447–465.

Giraldo, F. X., J. S. Hesthaven, and T. Warburton, 2002: Nodal high-order discontinuous Galerkin methods for the spherical shallow water equations. *Journal of Computational Physics*, **181**, 499–525.

Griffies, S. M., 2004: *Fundamentals of Ocean Climate Models*. Princeton University Press.

Haidvogel, D. B., J. C. McWilliams, and P. R. Gent, 1992: Boundary current separation in a quasigeostrophic, eddy-resolving ocean circulation model. *Journal of Physical Oceanography*, **22 (8)**, pp. 882–902.

Haller, G., 2004: Exact theory of unsteady separation for two-dimensional flows. *Journal of Fluid Mechanics*, **512**, 257–311.

Jakob, R., J. J. Hack, and D. L. Williamson, 1993: Solutions to the shallow water test set using the spectral transform method. *NCAR TECHNICAL NOTE*, **TN-388+STR**.

Lanser, D., J. G. Blom, and J. G. Verwer, 2000: Spatial discretization of the shallow water equations in spherical geometry using Osher's scheme. *Journal of Computational Physics*, **165 (2)**, 542 – 565.

Läuter, M., F. X. Giraldo, D. Handorf, and K. Dethloff, 2008: A discontinuous Galerkin method for the shallow water equations in spherical triangular coordinates. *Journal of Computational Physics*, **227 (24)**, 10 226 – 10 242.

Läuter, M., D. Handorf, and K. Dethloff, 2005: Unsteady analytical solutions of the spherical shallow water equations. *Journal of Computational Physics*, **210 (2)**, 535–553.

Le Roux, D. Y., A. Staniforth, and C. A. Lin, 1998: Finite elements for shallow-water equation ocean models. *Monthly Weather Review*, **126 (7)**, 1931–1951.

Lekien, F. and G. Haller, 2008: Unsteady flow separation on slip boundaries. *Physics of Fluids*, **20 (9)**.

LeVeque, R. J., 1992: *Numerical Methods for Conservation Laws*. Birkhäuser Verlag.

Long, D. and J. Thuburn, 2011: Numerical wave propagation on non-uniform one-dimensional staggered grids. *Journal of Computational Physics*, **230**, 2643–2659.

Ma, T. and S. Wang, 2001: Structure of 2-d incompressible flows with the Dirichlet boundary conditions. *Discrete Cont. Dyn. Syst.*, **B (1)**, 29 – 41.

Mañé, R., 1978: Persistent manifolds are normally hyperbolic. *Transactions of the American Mathematical Society*, **246**, 261–283.

Mancho, A. M., D. Small, and S. Wiggins, 2006: A comparison of methods for interpolating chaotic flows from discrete velocity data. *Computers & Fluids*, **35 (4)**, 416 – 428.

McWilliams, J. C., 2006: *Fundamentals of Geophysical Fluid Dynamics*. Cambridge University Press.

Medina, F. and R. Rosales, 1987: Spurious reflections and accuracy of finite element models for unbounded wave propagation problems: The one-dimensional case. *Engineering Computations*, **4 (2)**, 139 – 148.

Monin, A., A. Yaglom, and J. Lumley, 2007: *Statistical Fluid Mechanics: Mechanics of Turbulence*. No. Bd. 1 in Dover Books on Physics Series, Dover Publications.

Müller, R. and U. Schulzweida, 2010: Climate Data Operators. Version 1.4.5.1.

Nair, R. D., S. J. Thomas, and R. D. Loft, 2005: A discontinuous Galerkin global shallow water model. *Monthly Weather Review*, **133 (4)**, 876–888.

Özgökmen, T. M., E. P. Chassignet, and A. M. Paiva, 1997: Impact of wind forcing, bottom topography, and inertia on midlatitude jet separation in a quasigeostrophic model. *Journal of Physical Oceanography*, **27 (11)**, 2460–2476.

Pedlosky, J., 1996: *Ocean Circulation Theory*. Springer Verlag.

Phillips, N. A., 1957: A map projection system suitable for large-scale numerical weather prediction. *J. Meteor. Soc. Japan*, **75**, 262–267.

Piggott, M. D., C. C. Pain, G. J. Gorman, D. P. Marshall, and P. D. Killworth, 2008: Unstructured adaptive meshes for ocean modeling. *Ocean Modeling in an Eddying Regime, Geophysical Monograph Series, American Geophysical Union*, 383–408.

Prandtl, L., 1904: Über Flüssigkeitsbewegung bei sehr kleiner Reibung. *Int. Math. Kongr. Heidelberg*, **Verh. 3**, 484–491.

Ringler, T. D., D. Jacobsen, M. Gunzburger, L. Ju, D. Michael, and W. Skamarock, 2011: Exploring a multiresolution modeling approach within the shallow-water equations. *Monthly Weather Review*, **139 (11)**, 3348–3368.

Ringler, T. D. and D. A. Randall, 2002: A potential enstrophy and energy conserving numerical scheme for solution of the shallow-water equations on a geodesic grid. *Monthly Weather Review*, **130 (5)**, 1397–1410.

Rípodas, P., et al., 2009: Icosahedral shallow water model (ICOSWM): Results of shallow water test cases and sensitivity to model parameters. *Geoscientific Model Development*, **2**, 581–638.

Roeckner, E., et al., 2003: The atmospheric general circulation model ECHAM 5. Part 1: Model description. *Tech. rep., Max Planck Institute for Meteorology*, **(349)**.

Ronchi, C., R. Iacono, and P. S. Paolucci, 1996: The 'cubed sphere': A new method for the solution of partial differential equations in spherical geometry. *Journal of Computational Physics*, **124 (1)**, 93 – 114.

Salmon, R., 1998: *Lectures on Geophysical Fluid Dynamics*. Oxford University Press.

Sears, W. R. and D. P. Tellionis, 1975: Boundary layer separation in unsteady flow. *SIAM Journal on Applied Mathematics*, **28**, 215 – 235.

Shahbazi, K., 2005: An explicit expression for the penalty parameter of the interior penalty method. *Journal of Computational Physics*, **205 (2)**, 401 – 407.

Shin, S., M. Sommer, S. Reich, and P. Névir, 2010: Evaluation of three spatial discretization schemes with the Galewsky et al. test. *Atmospheric Science Letters*, **11**, 223–228.

Taylor, M., J. Tribbia, and M. Iskandarani, 1997: The spectral element method for the shallow water equations on the sphere. *Journal of Computational Physics*, **130 (1)**, 92 – 108.

Thuburn, J. and Y. Li, 2000: Numerical simulations of Rossby-Haurwitz waves. *Tellus A*, **52 (2)**, 181–189.

Trefethen, L. N., 1982: Group velocity in finite difference schemes. *SIAM Review*, **24**.

Ullrich, P. A. and C. Jablonowski, 2011: An analysis of 1d finite-volume methods for geophysical problems on refined grids. *Journal of Computational Physics*, **230**, 706–725.

Ullrich, P. A., C. Jablonowski, and B. van Leer, 2010: High-order finite-volume methods for the shallow-water equations on the sphere. *Journal of Computational Physics*, **229**, 6104–6134.

Vichnevetsky, R., 1987: Wave propagation and reflection in irregular grids for hyperbolic equations. *Applied Numerical Mathematics*, **3 (1-2)**, 133–166.

Williams, J. C., 1977: Incompressible boundary-layer separation. *Ann. Rev. Fluid Mech.*, **9**, 113–144.

Williamson, D. L., J. B. Drake, J. J. Hack, R. Jakob, and P. N. Swarztrauber, 1992: A standard test set for numerical approximations to the shallow water equations in spherical geometry. *Journal of Computational Physics*, **102 (1)**, 211–224.

Acknowledgements

I thank Peter Korn for his exceptional supervision. The scientific problems he assembled for this PhD project were very well picked. The useful hints he gave and questions he asked guided me safely through the difficult terrain of model development. I thank Jochem Marotzke for being an excellent co-adviser, the comprehensive training to become a good scientist, and the steady support to keep this thesis on track. I thank Vadym Aizinger for all the time he spent with me in fruitful discussions, and his intensive support towards the publication of the first paper. I thank Bjorn Stevens for his very motivating contributions as Panel Chair.

Thanks to Almut Gaßman, Leonidas Linardakis, Juan-Pedro Mellado, Hui Wan, Marco Giorgetta, Helmuth Haak, and all the other people who answered the many questions I asked.

I thank Antje Weitz and Cornelia Kampmann for making the IMPRS-ESM PhD school a great opportunity to realize ideas, and their committed support.

I thank Colin Cotter for his scientific input, the insight to model code, and the possibility to learn more about the ICOM project at Imperial College London, through an academic visit.

Furthermore, I thank Hui Wan and Juan-Pedro Mellado for careful (internal) reviews of the Chapters 2 and 3, and Sergey Danilov and the two unknown external reviewers for their useful comments on Chapter 2. Thanks to Philipp, Florian R., and Thomas for proofreading parts of this thesis.

Special thanks to my fellow PhD students and friends Aiko, Fanny, Florian Z., Freja, Laura, Louise, Mario, Mathias, Nils, Philipp, Rosi, Steffen, Thomas, Vera, Werner, and all the others, and certainly to Florian R. who showed me how to finish a PhD properly.

I thank my office mate Chao together with Hongmei and Helen for the nice time we had, and all the healthy Chinese tea that kept me alive.

I thank my parents and my brother for their steady support. Many thanks to Michi for making me as happy as I am.

ISSN 1614-1199